DOCTORAL DISSERTATION

Analysis and measurement of OFDM-based communication systems considering power amplifier nonlinearity

パワーアンプの非線形性を考慮したOFDMに基づく
通信システムの測定と解析

Author:
Taewoo LEE

Supervisor:
Professor Hideki OCHIAI

A dissertation submitted in fulfilment of the requirements
for the degree of Doctor of Engineering

in the

Department of Physics, Electrical and Computer Engineering

YOKOHAMA NATIONAL UNIVERSITY

Date of Submission : March 2016

Initiative for
Global Arts & Sciences
YNU 横浜国立大学
YOKOHAMA National University

Declaration of Authorship

I, Taewoo LEE, declare that this dissertation titled, "Analysis and measurement of OFDM-based communication systems considering power amplifier nonlinearity" and the work presented in it are my own. I confirm that:

- This work was done wholly or mainly while in candidature for a research degree at this University.
- Where any part of this dissertation has previously been submitted for a degree or any other qualification at this University or any other institution, this has been clearly stated.
- Where I have consulted the published work of others, this is always clearly attributed.
- Where I have quoted from the work of others, the source is always given. With the exception of such quotations, this dissertation is entirely my own work.
- I have acknowledged all main sources of help.
- Where the dissertation is based on work done by myself jointly with others, I have made clear exactly what was done by others and what I have contributed myself.

Signed:

_____

Date:

_____

Abstract

Department of Physics, Electrical and Computer Engineering

YOKOHAMA NATIONAL UNIVERSITY

Doctor of Engineering

Analysis and measurement of OFDM-based communication systems considering power amplifier nonlinearity

by Taewoo LEE

Orthogonal frequency division multiplexing (OFDM) has been adopted in many modern communication systems due to its robustness against frequency-selective fading channels as well as its near rectangular spectrum that can achieve high spectral efficiency. However, its major drawback is the resulting signal with high peak-to-average power ratio (PAPR), which causes severe nonlinear distortion at the power amplifier (PA) unless input back off is chosen sufficiently large. The effect of the nonlinear distortion is two-fold: out-of-band radiation and signal quality degradation. The former causes adjacent channel interference and thus degrades the bandwidth efficiency. The latter affects the system level performance and is often measured by the error vector magnitude (EVM). It is thus important for the system designer to analyze the nonlinear distortion caused by a given PA in terms of power spectral density (PSD) and EVM, but accurate calculation of these characteristics may be generally involved.

Reduction of PAPR is important for small long distance communication devices such as user terminals of mobile networks whose power consumption is of significant importance. From this viewpoint, single-carrier frequency division multiple access (SC-FDMA) is an attractive technology mainly due to its signal with lower PAPR than that of OFDM. Nevertheless, an attempt to further reduce PAPR even for SC-FDMA systems may be desirable since SC-FDMA signal still exhibits relatively high PAPR compared to the conventional single-carrier signals. Therefore, in this dissertation a new PAPR reduction scheme based on trellis shaping is developed for SC-FDMA systems.

Acknowledgements

As important as the achievement of my researches itself is to express gratitude to everyone who helped me throughout my long-term Ph.D course. I have to say that it is impossible for an individual to complete my Ph.D degree without a significant amount of support be it direct or indirect, technical, financial or emotional. At the same time it is difficult to mention all those who may have given me such valuable supports. For this reason, I apologize for the ones who are not mentioned here in advance, but your assistance and contribution are greatly appreciated.

Firstly, I would like to express my deepest gratitude to my advisor, professor Hideki Ochiai, for his excellent guidance, caring, patience, and providing me with an excellent atmosphere for doing research. Also, I would also like to thank several graduate students whose friendships have helped me to become a better researcher.

This work would not be possible without the support from my family. My wife, Jin has been extremely supportive of me throughout my Ph.D course and has made incalculable sacrifices to help me get to this point. My son, Sanghwa has continually provided the motivation to finish my degree with expediency.

Finally, my parents deserve special thanks for their continued support and encouragement. They have always been a huge inspiration to me and have always supported my actions and endeavors whatever they may be. They provided me with all the opportunities that anyone could ever dream of, and for this I will always be eternally grateful. Also, my heartfelt thanks must go to my brother and sisters for their emotional support and encouragement.

Without such greatest people behind me, I doubt that I would be in this place today.

Taewoo LEE

For my sons and wife.

Contents

List of Figures

List of Tables

Chapter 1

Introduction

1.1 Background

Recent wireless communication industry has focused on the fifth generation (5G) of mobile technology succeeding the fourth generation (4G), namely long-term evolution-advanced (LTE-Advanced) [Liu+15; WN15; CZ14]. LTE-Advanced technology is standardized by the 3rd generation partnership project (3GPP) and it can realize high capacity. With the latest generation technology, voice, video and even large data can be transmitted through the air. Also, any physical objects could be connected to the Internet through wireless communication technology known as the Internet of Things (IoT) [GYL11; Zor+10]. Such objects are embedded with sensors for data collection and wireless communication modules for data transmission. The common requirements of the above mentioned technologies are the efficient usage of frequency resource and power source.

As a rapid increase of mobile terminals, the usage of frequency resource grows dramatically. As a result, it suffers from lack of frequency resource in several Giga Hertz band so that, for instance, 5G technology challenges to use in Tera Hertz band. Orthogonal frequency division multiplexing (OFDM) is one of the approaches that can efficiently utilize frequency resource. OFDM maintains orthogonality between adjacent subcarriers, that is, each subcarrier is allocated with minimum spacing, and therefore the bandwidth efficiency is relatively high. However, a major drawback of OFDM is its high peak-to-average power ratio (PAPR) since the signal bearing high PAPR causes severe nonlinear distortion in power amplifier (PA).

As an alternative technology, single-carrier frequency division multiple access (SC-FDMA) has been adopted in LTE-Advanced standard as its uplink transmission for the reason of high spectral efficiency and lower PAPR compared to that of OFDM.

However, it still suffers from relatively high PAPR when the effect of pulse-shaping filter (or the transformation process often referred to as precoding) is considered.

Any PA essentially has its linear and saturated amplification regions. Once the transmit signal is amplified in saturation region, the critical nonlinear distortion is incurred, which falls on both inband and out-of-band. The inband nonlinear distortion can be mitigated by channel coding in receiver side whereas out-of-band distortion may not be usually canceled after amplification by PA, and thus causes severe interference to adjacent channel, degrading the overall spectral efficiency. In order to use frequency resource more efficiently, therefore, it is essential to avoid nonlinear distortion. For this reason, most of wireless communication standards strictly limit out-of-band radiation associated with nonlinear distortion.

Interestingly, PA is also related with battery life as it is the most power hungry device in wireless communication system since constant power is, in general, supplied to PA. However, only a limited amount of supplied power is used for amplification, and rest of the supplied power is converted to heat dissipation. Moreover, in order to maximize the power efficiency, one should increase the average power of PA input signal close to the saturation point. From a viewpoint of system designer, in order to avoid nonlinear distortion caused by PA, it is necessary to decrease the average power so that the signal fluctuation range (i.e., PAPR) should fit into linear amplification region according to target PA characteristic. In this case, however, the power efficiency is considerably decreased. Since a mobile terminal is mostly operated by battery, an efficient use of PA that leads to lower power consumption together with high power efficiency is highly desirable.

1.2 Aims of this thesis

1.2.1 Effectiveness of Peak Power Reduction Technique on OFDM

As mentioned above, most of recent wireless communication standards adopt OFDM transmission technique due to its several merits such as high bandwidth efficiency and robustness against frequency-selective fading channels. In the fist part of this work, we focus on the wireless local area network.

IEEE 802.11ac wireless local area network (WLAN) has become a leading standard in indoor wireless communication systems due to its compatibility with existing standard

and high capacity. Among its backward compatible technologies, we focus on IEEE 802.11g which supports four different layers; two existing layers which are mandatory (i.e., ERP-DSSS/CCK and ERP-OFDM) and two new layers which are optional (i.e., ERP-PBCC and DSSS-OFDM). These layers defined as ERP (Extended rate PHY) in IEEE 802.11g standard are described in [Vas+05; Ieea]. ERP-DSSS provides backward compatibility with IEEE 802.11b standard which operates under the same carrier frequency (2.4GHz). Also, ERP-OFDM has the same frame format as IEEE 802.11a [Ieeb], which is based on OFDM, enabling high speed communications up to 54Mbps in the single-input single-output (SISO) framework. Without considerable input back off (IBO) of PA, the OFDM signal frequently exceeds its saturation level and causes nonlinear distortion. The quality of signal thus degrades and this causes adjacent channel interference (ACI). On the other hand, operating PA with large IBO considerably reduces its efficiency, causing increase of heat dissipation, which also lowers the quality of transmitted signals.

The peak power reduction technique is a key to improve trade-off relationship between the quality of the signal and the efficiency of PA. Many peak power reduction techniques have been proposed for OFDM systems (e.g., [HL05; JW08]). Among them, the clipping and filtering (CAF) is one of the simplest candidates that are applicable to many existing standards such as IEEE 802.11g since it does not require major modification of the receiver configuration of the standard. An apparent drawback of CAF is its irreducible nonlinear distortion that falls within the signal bandwidth. The question is how much clipping is tolerable while complying with the standard requirement.

The CAF reduces not only the dynamic range (or PAPR) but also the average power of the transmitted signal. The signal input to PA is peak power (or maximum signal envelope) limited, rather than the average power. In other words, for a given input envelope level, by reducing the PAPR through the CAF, we can increase the average power of transmitting signal. Accordingly, our goal is to experimentally reveal the effectiveness of the CAF on the IEEE 802.11g WLAN system while increasing average power under the given constraints such as error vector magnitude (EVM) and ACI by using real PA.

1.2.2 Estimation of Distortion for Nonlinearly Amplified OFDM Signal

In order to maximize power efficiency in PA, it is essential to make the PA input signal to be amplified around saturation region. However, this amplification introduces

severe nonlinear distortion which degrades the signal quality, and in turn increases bit error rate (BER). In addition, it also introduces spectral regrowth which leads to ACI. On the other hand, when we set the operation point of PA as much lower value than its saturation point, it suffers from severe low power efficiency problem. This is well-known tradeoff relationship between the power efficiency and the quality of transmit signal [Och13; Lia+99]. In particular, the signal bearing large dynamic range such as OFDM severely suffers from peak power problem.

Many analytical and experimental studies have been performed to compromise this tradeoff relationship on OFDM signal. They are roughly categorized into PAPR reduction and PA linearization techniques. PAPR reduction techniques can significantly reduce the dynamic range of PA input signal. For example, the clipping and filtering is an attractive technique as the dynamic range can be adjusted by clipping process, and the adjacent channel power regrowth can also be suppressed by filtering process. However, it causes inevitable inband nonlinear distortion [LC98; OI02].

The PA linearization technique improves the linearity of nonlinear PA and thereby enhances the efficiency of PA for given amount of nonlinear distortion. The digital predistortion (DPD) is a widely used approach that compensates the PA nonlinearity [Li+09; car+10]. These approaches require the knowledge of the characteristic of given PAs. For these reasons, PA modelling has been focused on in recent research. In accordance with the characteristic of PA, PA models are categorized into strictly memoryless, quasi-memoryless and memory PA models [BG89]. The output signal of strictly memoryless PA models (e.g., Rapp model [Rap91]) only depends on the AM-AM characteristic while quasi-memoryless PA models (e.g., Saleh model [Sal81]) are based on both the AM-AM and AM-PM. Recently, the Volterra behavioral model has been used to describe the memory effect of PA [CCRTMA07].

From a viewpoint of communication system designer, since many of wireless communication standards such as IEEE 802.11 wireless LAN strictly regulate the spectral regrowth in order to use finite bandwidth resource efficiently, it may be helpful if performances such as spectral regrowth or EVM of PA output signal are able to be predicted. In this thesis, we propose an approach to develop a simple model that can accurately characterize the power spectral density (PSD) and EVM of the resulting OFDM signals. Our approach is based on the use of the cross-correlation coefficient between the input and output signals from the PA, which can be easily calculated from its AM-AM and AM-PM characteristics and input back off operation.

1.2.3 Peak Power Reduction Technique on SC-FDMA

The major advantage of SC-FDMA over OFDM is its signal with lower PAPR. The signal bearing higher PAPR should be operated by a PA with higher IBO, which translates to lower efficiency in terms of power amplification. Since a user terminal is mostly operated by battery, an efficient use of the PA that leads to lower power consumption is highly desirable.

Even though an SC-FDMA signal generally has lower PAPR than OFDM, the output signal from pulse shaping filter also suffers from relatively high PAPR. Since the property of SC-FDMA is inherited from single-carrier, the peak power reduction technique developed for conventional single-carrier signals may be also applicable to SC-FDMA signals. In [CC05], a trellis-based peak power reduction technique is proposed, where the pulse shaping filter is viewed as a convolutional encoder. The peak power reduction performance is achieved effectively while the complexity is increased significantly. More recently, in [TO09a], the use of trellis shaping (TS) is proposed for PAPR reduction of general single-carrier signals. The TS significantly reduces peak power of single-carrier signals in the presence of pulse shaping filter. However, the applicability and effectiveness of the TS approach to SC-FDMA should be investigated due to its rather different structure compared to conventional single-carrier system. In fact, certain modification of TS is necessary to achieve effective PAPR reduction of SC-FDMA signals.

In this thesis, we propose a modified TS design suitable for SC-FDMA and evaluate its peak power reduction performance together with ACI and BER over nonlinear and frequency-selective fading channels.

1.3 Outline of This Thesis

This thesis is devoted to design and analysis of single-carrier as well as OFDM systems with main focus on the peak-to-average power ratio issue. The outline of the subsequent chapters is illustrated in Fig. 1.1. Some of the chapters share common objective, direction, or approach as categorized in the figure, but each chapter is presented in a self-contained manner such that it can be read without deep understanding of the preceding chapters.

- In Chapter 2 titled as "Overview of Multicarrier Modulation Transmission System ," we briefly overview OFDM and SC-FDMA signal models used in this thesis. Analytical models are derived, and peak power generation mechanism is discussed.

- In Chapter 3 titled as "Experimental Analysis of the Effectiveness of Clipping and Filtering for OFDM Systems," we analyze the effectiveness of the CAF on the OFDM system through experiment using a real power amplifier. We apply the CAF to IEEE 802.11g WLAN standard as a system which has strict constraints on both EVM and power spectra, and evaluate the increase of the received power under the given EVM and power spectral constraints by adjusting the input back-off (IBO) of the power amplifier. It is shown that by appropriately adjusting the IBO and clipping ratio, the received power can be slightly improved under the constraints.

- In Chapter 4 titled as "Characterization of Power Spectral Density for Nonlinearly Amplified OFDM Signals," by establishing the link between the cross-correlation coefficient of the input and output signals from PA and the resulting PSD, we theoretically characterize the in-band and out-of-band distortion of nonlinearly amplified OFDM signals based exclusively on the cross-correlation coefficient. The accuracy of the proposed approach is confirmed by both simulation and measurement using a real PA.

- In Chapter 5 titled as "A Trellis Shaping Approach for Peak Power Reduction of SC-FDMA Signals ," we investigate the impact of a peak power reduction of SC-FDMA signal by modifying the trellis shaping technique that has been recently developed for peak power reduction of conventional single-carrier modulation. It is shown that the SC-FDMA signal with TS can significantly improve the PA efficiency, thus serving as a potential candidate for the uplink of next generation cellular networks. We also investigate the achievable PA efficiency together with bit error performances over AWGN and frequency selective Rayleigh fading channels.

- Chapter 6 summarizes this dissertation and describes future works.

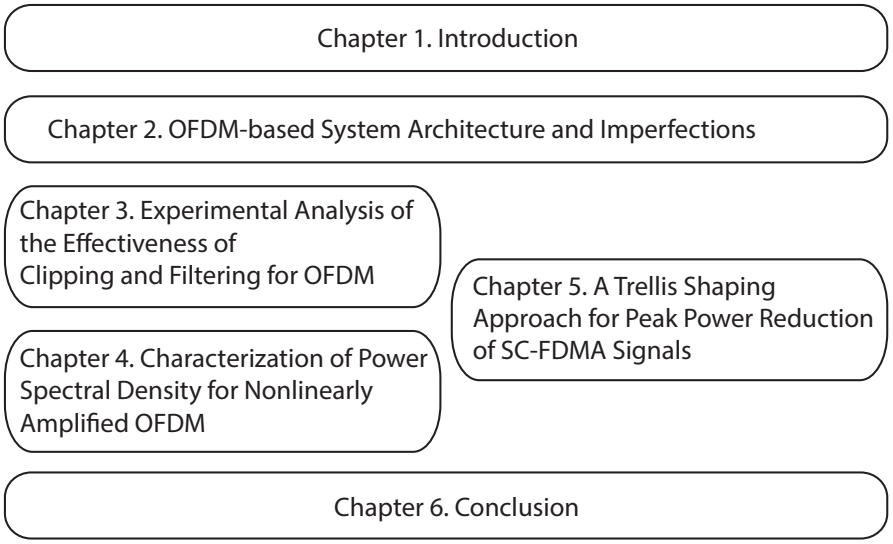

Figure 1.1: Organization of this dissertation.

Chapter 2

OFDM-based System Architecture and Imperfections

This chapter describes the fundamentals of OFDM-based systems and its nonlinear distortion effect caused by power amplifier.

2.1 Fundamentals of OFDM-based System

2.1.1 OFDM Signal

The complex-valued baseband OFDM signal can be expressed by using N-point inverse discrete Fourier transform (IDFT) given by

$$x_k = \frac{1}{\sqrt{N}} \sum_{n=0}^{N-1} X_n e^{j2\pi nk/N}, \tag{2.1}$$

where X_n is M-QAM (or PSK) mapped symbol and x_k is time-domain signal. In the receiver side, demodulation process of x_k is simply achieved by applying discrete Fourier transform (DFT) with assumption of no channel noise as

$$X_n = \frac{1}{\sqrt{N}} \sum_{k=0}^{N-1} x_k e^{-j2\pi kn/N}. \tag{2.2}$$

Unlike conventional frequency division multiplexing (FDM) modulation, OFDM retains the orthogonality since

$$\frac{1}{N} \sum_{n=0}^{N-1} \sum_{k=0}^{N-1} e^{j2\pi k/N} e^{-j2\pi n/N} = \frac{1}{N} \sum_{n=0}^{N-1} \sum_{k=0}^{N-1} e^{j2\pi (k-n)/N} = \begin{cases} 1, & \text{for } k = n, \\ 0, & \text{otherwise.} \end{cases} \tag{2.3}$$

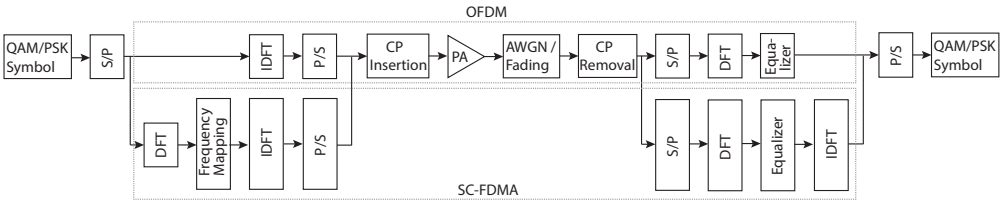

Figure 2.1: Block diagram of OFDM and SC-FDMA

Note that all the subcarriers can be superposed due to their orthogonality, and thus the bandwidth efficiency is relatively high.

2.1.2 SC-FDMA Signal

SC-FDMA is often called as DFT-precoded OFDM since the transmit signal is generated by inverse DFT using symbols preprocessed in DFT as shown in Fig. 2.1. Since the signal generation process of SC-FDMA system is inherited from single-carrier system, its signal has lower peak power compared to those of multicarrier system. SC-FDMA is categorized into interleaved FDMA (IFDMA) and localized FDMA (LFDMA) depending on the frequency mapping methods. In this dissertation, we focus on LFDMA since it has advantages in terms of practical implementation. As shown in Fig. 2.1, the former DFT whose size is N plays a role to convert time domain user data $\{x_n : n = 0, 1, \cdots, N-1\}$ to frequency domain components $\{X_m : m = 0, 1, \cdots, N-1\}$ given by

$$X_m = \frac{1}{\sqrt{N}} \sum_{n=0}^{N-1} x_n e^{j2\pi \frac{mn}{N}}. \tag{2.4}$$

Then X_m is processed by the frequency mapping that generates $\tilde{X}_k$, where zeros are inserted to the remaining $(N-1)Q$ subcarriers as follows:

$$\tilde{X}_k = \begin{cases} X_m & : k = m, \\ 0 & : \text{elsewhere}, \end{cases} \tag{2.5}$$

where Q ($Q > 0$: integer) is a bandwidth spread factor and $k \in \{0, 1, \cdots, NQ-1\}$.

Finally, frequency mapped components $\tilde{X}_k$ are converted to time domain signal $\tilde{x}_l$ through NQ-point IDFT which is expressed as

$$\tilde{x}_l = \frac{1}{\sqrt{N}} \sum_{k=0}^{NQ-1} \tilde{X}_k e^{j2\pi \frac{lk}{NQ}}. \tag{2.6}$$

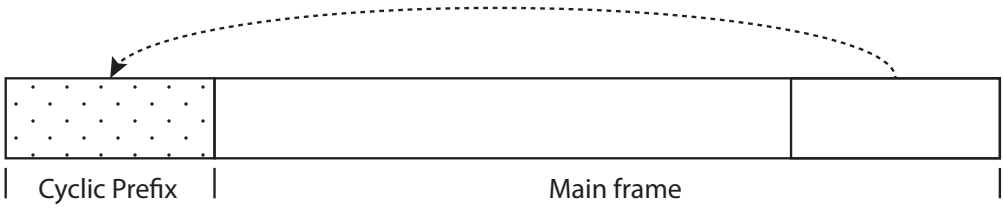

Figure 2.2: Cyclic-prefixed transmit frame.

Note that the resultant sequence $\tilde{x}_l$ is normalized by $1/\sqrt{N}$ due to the fact that only N subcarriers of $\tilde{X}_k$ contain non-zero frequency components.

Generally, since the peak power of the signal after lowpass filter is of primary interest, in order to obtain exact peak power of $\tilde{x}_l$, it is essential that $\tilde{x}_l$ is band-limited. This can be generated by adding extra zeros to $\tilde{X}_k$ with oversampling factor J, i.e.,

$$\bar{X}_k = \begin{cases} \tilde{X}_k & : k \in \{0, 1, \cdots, NQ-1\} \\ 0 & : k \in \{NQ, NQ+1, \cdots, JNQ-1\} \end{cases} \tag{2.7}$$

Accordingly, from (2.6) and (2.7) the band-limited signal $\bar{x}_p$, where $p \in \{0, 1, \cdots, JNQ-1\}$ can be expressed by

$$\bar{x}_p = \frac{1}{\sqrt{N}} \sum_{k=0}^{NQ-1} \bar{X}_k e^{j2\pi \frac{pk}{JNQ}}. \tag{2.8}$$

2.1.3 Cyclic Prefix

One of the major advantages of OFDM and SC-FDMA is their robustness against multipath fading channel. The robustness can be achieved by cyclic prefix (CP), also called guard interval. Since the addition of CP to OFDM and SC-FDMA brings essentially the same effect, we take an example based on the OFDM signal. The CP is composed by duplicating OFDM signal at the range of $N - N_{\text{cp}} \leq k_c < N$, where N_{cp} is the length of CP, and appending it to the beginning of the frame as illustrated in Fig. 2.2. Specifically, the OFDM signal with CP can be expressed as

$$y_{n_c} = \begin{cases} x_{n_c}, & 0 \leq n_c < N, \\ x_{N+n_c}, & -N_c \leq n_c < 0, \end{cases} \tag{2.9}$$

where $-N_c \leq n_c < N$. Note that the intersymbol interference (ISI) can be removed by CP when its length is set as longer than that of channel impulse response i.e., $\frac{N_{\text{cp}}}{N} T > \tau_{\max}$ where T is symbol period and $\tau_{\max}$ is the maximum propagation delay. The cyclic

prefixed signal is transmitted through multipath fading channel. The received signal is given by [Pro01]

$$r(t) = h(t) \star y(t) + w(t) = \int_{-\infty}^{\infty} h(\tau) y(t-\tau) d\tau + w(t) \\ = \int_{0}^{\tau_{\max}} h(\tau) y(t-\tau) d\tau + w(t), \tag{2.10}$$

where $\star$ denotes convolution process, $w(t)$ and $h(t)$ are additive white Gaussian noise (AWGN) with zero mean and unit variance and time invariant channel impulse response, respectively, and $y(t)$ is continuous signal of y_{n_c} given by

$$y(t) = y(n\Delta T) = \frac{1}{\sqrt{N}} \sum_{k=0}^{N-1} X_k e^{j2\pi k n \Delta T}, \tag{2.11}$$

where $\Delta T = T/N$. Note that due to the periodicity of Fourier transform, expression (2.11) is still valid in the range of $-\frac{N_c}{N} T \leq t < T$. Consequently, the detected symbol can be expressed by substituting (2.11) into (2.10) and applying DFT as

$$\begin{aligned} \bar{X}_l &= \frac{1}{\sqrt{N}} \sum_{n=0}^{N-1} \left(\int_0^{\tau_{\max}} h(\tau) y(t-\tau) d\tau + w(t) \right) e^{-j2\pi nl/N} \\ &= \frac{1}{N} \sum_{n=0}^{N-1} \left(\int_0^{\tau_{\max}} h(\tau) \sum_{k=0}^{N-1} X_k e^{j2\pi k(n\Delta T - \tau)} d\tau + w(n\Delta T) \right) e^{-j2\pi nl/N} \\ &= \frac{1}{N} \sum_{n=0}^{N-1} \sum_{k=0}^{N-1} X_k \left(\int_0^{\tau_{\max}} h(\tau) e^{-j2\pi k\tau} d\tau \right) e^{j2\pi nk/N} e^{-j2\pi nl/N} + W_l \\ &= \frac{1}{N} \sum_{k=0}^{N-1} X_k H_k \sum_{n=0}^{N-1} e^{j2\pi n(k-l)/N} + W_l, \end{aligned} \tag{2.12}$$

where

$$W_l = \frac{1}{N} \sum_{n=0}^{N-1} w(n\Delta T) e^{-j2\pi ln/N}, \tag{2.13}$$

and

$$H_k = \int_0^{\tau_{\max}} h(\tau) e^{-j2\pi k\tau} d\tau. \tag{2.14}$$

Expression (2.12) can be simplified by the orthogonality principle of the subcarriers as

$$\bar{X}_l = X_l H_l + W_l. \tag{2.15}$$

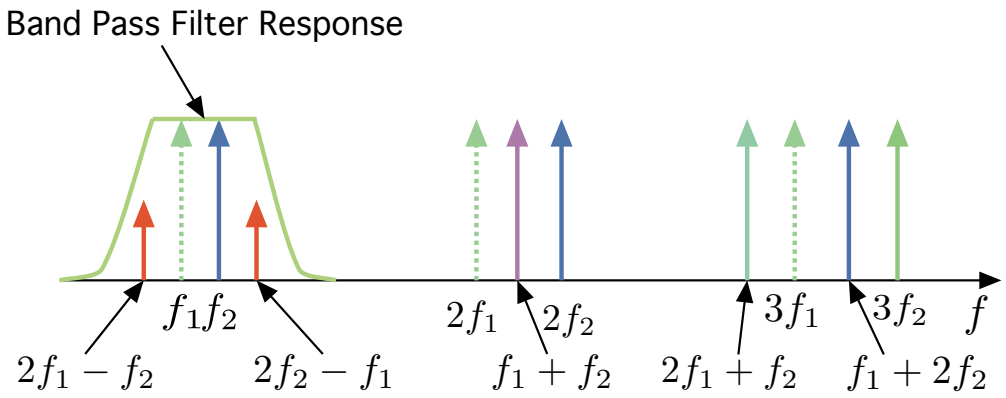

Figure 2.3: Inband and out-of-band nonlinear distortion components caused by PA.

The above relationship shows that, without Gaussian noise, the detected symbol on the lth subcarrier can be expressed as the product of the originally transmitted symbol X_l and the corresponding channel response H_l.

2.2 Imperfection of OFDM-based Signal

As mentioned before, a major drawback of OFDM-based signal is its high peak-to-average power ratio (PAPR). Generally, high PAPR signal suffers from nonlinear distortion in power amplifier (PA) and it falls inband and out-of-band. Let us assume that PA input signal contains two different carrier frequencies

$$x(t) = A\cos(w_1 t) + B\cos(w_2 t), \tag{2.16}$$

where $w_k = 2\pi f_k$. For the sake of simple analysis of nonlinear distortion by PA, Taylor series expansion is often adopted so that we can obtain nonlinearly amplified PA output signal y(t) as

$$\begin{aligned} y(t) &= \sum_{n=0}^{\infty} a_{2n+1} x^{2n+1} \\ &= \sum_{n=0}^{\infty} a_{2n+1} \left(A\cos(w_1 t) + B\cos(w_2 t)\right)^{2n+1}. \end{aligned} \tag{2.17}$$

Note that the ideal PA has only the first-order term, that is, a_1, which corresponds to the linear gain. After some algebraic manipulation of (2.17) with trigonometric property, we see that PA output signal contains many of different frequency components commonly referred to intermodulation distortion. As an example, the third-order term

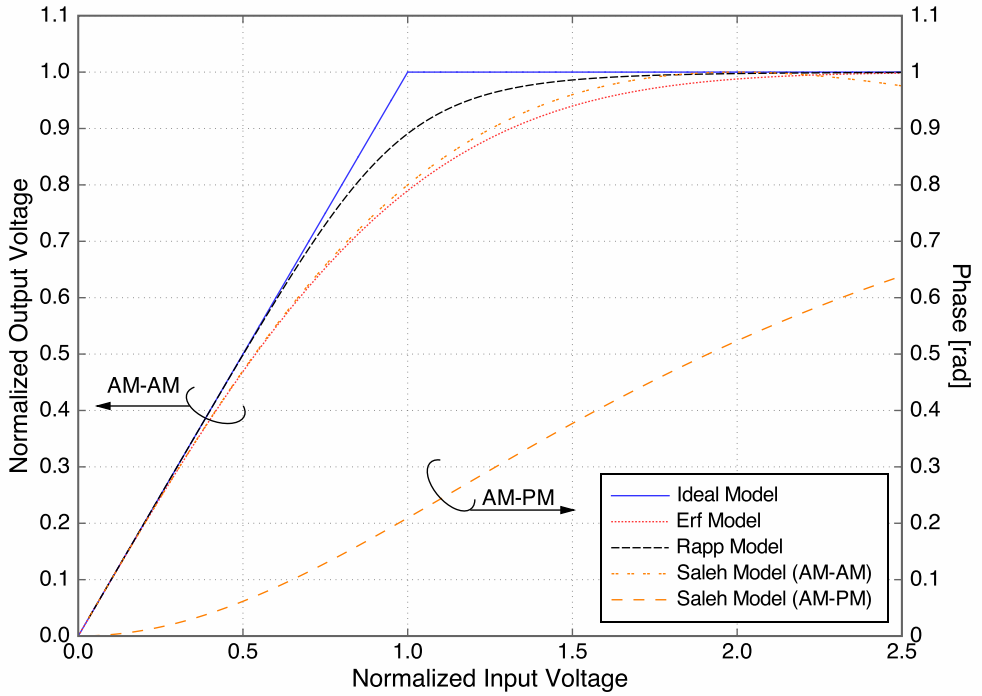

Figure 2.4: The AM-AM and AM-PM characteristics of PA models used in this work where the reference envelope level $A_{\max}$ is chosen as 1.0. For the Rapp model, the parameter p is chosen as 3.0.

can be derived by

$$
\begin{aligned}
a_3(A\cos(w_1t) + B\cos(w_2t))^3 = \\
&\left(\frac{3a_3A^3}{4} + \frac{3a_3AB^2}{2}\right)\cos(w_1t) + \left(\frac{3a_3A^2B}{2} + \frac{3a_3B^3}{4}\right)\cos(w_2t) \\
&+ \frac{a_3A^3}{4}\cos(3w_1t) + \frac{a_3B^3}{4}\cos(3w_2t) \\
&+ \frac{3a_3A^2B}{4}\cos\left((2w_1 + w_2)t\right) + \frac{3a_3AB^2}{4}\cos\left((w_1 + 2w_2)t\right) \\
&+ \frac{3a_3A^2B}{4}\cos\left((2w_1 - w_2)t\right) + \frac{3a_3AB^2}{4}\cos\left((2w_2 - w_1)t\right). \qquad (2.18)
\end{aligned}
$$

Figure 2.3 illustrates frequency components in (2.18). We see that many of frequency components are newly generated by PA nonlinearity, and those except for f_1 and f_2 serve as interference over inband and out-of-band. Even if the received signal goes through bandpass filter in receiver side, some frequency components close to that of desired one still remains, and they causes degradation of error rate performance.

2.2.1 Power Amplifier Models

Several memoryless power amplifier models are introduced for characterization of real PA. In this subsection, we briefly describe its characteristics.

Envelope Limiter

The soft envelope limiter model is defined as

$$G(r) = g(r) = \begin{cases} r, & r < A_{\max}, \\ A_{\max}, & r \geq A_{\max}, \end{cases} \tag{2.19}$$

where $A_{\max}$ denotes the maximum envelope level of input signal where it is linearly amplified. Note that without loss of generality, the amplifier gain is normalized to unity and the AM-PM characteristic is absent (i.e., $\phi(r) = 0$) in this model.

Erf Model

The erf model is defined as [Och13; Gal59]

$$G(r) = g(r) = A_{\max}\text{erf}\left(\frac{\sqrt{\pi}}{2}\frac{r}{A_{\max}}\right), \tag{2.20}$$

where $A_{\max}$ in this case corresponds to the maximum output envelope level if the power gain is normalized to unity, and $\text{erf}(\cdot)$ is the error function given by

$$\text{erf}(x) = \frac{2}{\sqrt{\pi}}\int_0^x e^{-t^2}dt. \tag{2.21}$$

Rapp Model

The Rapp model (also known as Cann model [Can80; Can12]) is frequently adopted for describing an SSPA model and given by [Rap91]

$$g(r) = \frac{r}{\left[1 + (r/A_{\max})^{2p}\right]^{\frac{1}{2p}}}, \tag{2.22}$$

where the definition of $A_{\max}$ is the same as that of the erf model, and p is a smoothness factor that controls transition from linear to nonlinear region of PA.

Saleh Model

In contrast to the Rapp model which has no AM-PM effect, we examine the TWTA model based on the Saleh model [Sal81]. The AM-AM characteristic is given by

$$g(r) = \frac{r}{1 + \frac{1}{4}(r/A_{\max})^2} \tag{2.23}$$

and the AM-PM characteristic is

$$\phi(r) = \frac{\pi}{12} \frac{(r/A_{\max})^2}{1 + \frac{1}{4}(r/A_{\max})^2} \ \text{(rad)}. \tag{2.24}$$

Polynomial Model

The baseband equivalent signal representation with the memoryless polynomial PA model can be expressed by [BB06]

$$\begin{aligned} y(t) &= \sum_{k=0}^{K} a_{2k+1} |x(t)|^{2k} x(t) \\ &= x(t) \sum_{k=0}^{K} a_{2k+1} r^{2k}(t) = a_1 x(t) + a_3 r^2(t) x(t) + \cdots , \end{aligned} \tag{2.25}$$

where a_{2k+1} is a complex-valued coefficient of the $(2k+1)$-th order and $2K+1$ is the maximum order considered. Note that the polynomial PA model is characterized by the odd-order terms only since the even-order terms will be removed by a subsequent zonal filter [BB06].

By expressing the complex-valued coefficient a_{2k+1} as $a_{2k+1} = b_{2k+1} e^{j\phi[r(t)]}$ where b_{2k+1} is a real-valued coefficient, we have

$$y(t) = x(t) \sum_{k=0}^{K} b_{2k+1} r^{2k}(t) e^{j\phi[r(t)]}. \tag{2.26}$$

We further assume that $\phi[r(t)]$ is expressed by only *even*-order terms, i.e.,

$$\phi[r(t)] = \sum_{i=0}^{I} c_{2i} r^{2i}(t), \tag{2.27}$$

where c_{2i} is a real-valued coefficient and $2I$ is the maximum order considered here. Then, by the Taylor series, the complex exponential term in (2.26) can be expanded to

the following polynomial expression:

$$\begin{aligned} e^{j\phi[r(t)]} &= \sum_{q=0}^{Q} \frac{(j\phi[r(t)])^q}{q!} \\ &= 1 + j\left\{\sum_{i=0}^{I} c_{2i} r^{2i}(t)\right\} - \frac{1}{2}\left\{\sum_{i=0}^{I} c_{2i} r^{2i}(t)\right\}^2 + \cdots \\ &= \sum_{q=0}^{Q} d_{2q} r^{2q}(t), \end{aligned} \tag{2.28}$$

where d_{2q} is a complex-valued coefficient and $2Q$ is the maximum order effective for the above polynomial. Substituting (2.28) into (2.26), we obtain

$$\begin{aligned} y(t) &= x(t) \sum_{k=0}^{K} b_{2k+1} r^{2k}(t) \sum_{q=0}^{Q} d_{2q} r^{2q}(t) \\ &= x(t) \left\{b_1 + b_3 r^2(t) + \cdots\right\} \left\{d_0 + d_2 r^2(t) + \cdots\right\} \\ &= x(t) \sum_{k=0}^{K+Q} z_{2k+1} r^{2k}(t), \end{aligned} \tag{2.29}$$

where z_{2k+1} is a complex-valued coefficient. By comparing (2.25) and (2.29), we observe that $z_{2k+1} = a_{2k+1}$ for $k = 0, 1, \ldots K$, which justifies our assumption that the polynomial model for phase distortion $\phi[r(t)]$ should only contain even-order terms.

2.2.2 Peak Power Characteristic of OFDM-based Signal

Assuming that transmit symbol X_k is statistically independent and identically distributed (i.i.d) random variable for large N, then the probability density function (PDF) of its complex-valued output x_k follows the Gaussian distribution given by

$$pr(x_k) = \frac{1}{\sqrt{2\pi\sigma_x^2}} e^{-\frac{x_k^2}{2\sigma_x^2}}, \tag{2.30}$$

where $\sigma_x^2 = E\{|x_k|^2\}$ and $E\{\cdot\}$ is averaging function. By the Chi-square distribution, we can derive the PDF of the instantaneous power $P_k = |x_k|^2$ given by [Pro01]

$$pr(P_k) = \frac{1}{2\sigma_x^2} e^{-\frac{P_k}{2\sigma_x^2}}. \tag{2.31}$$

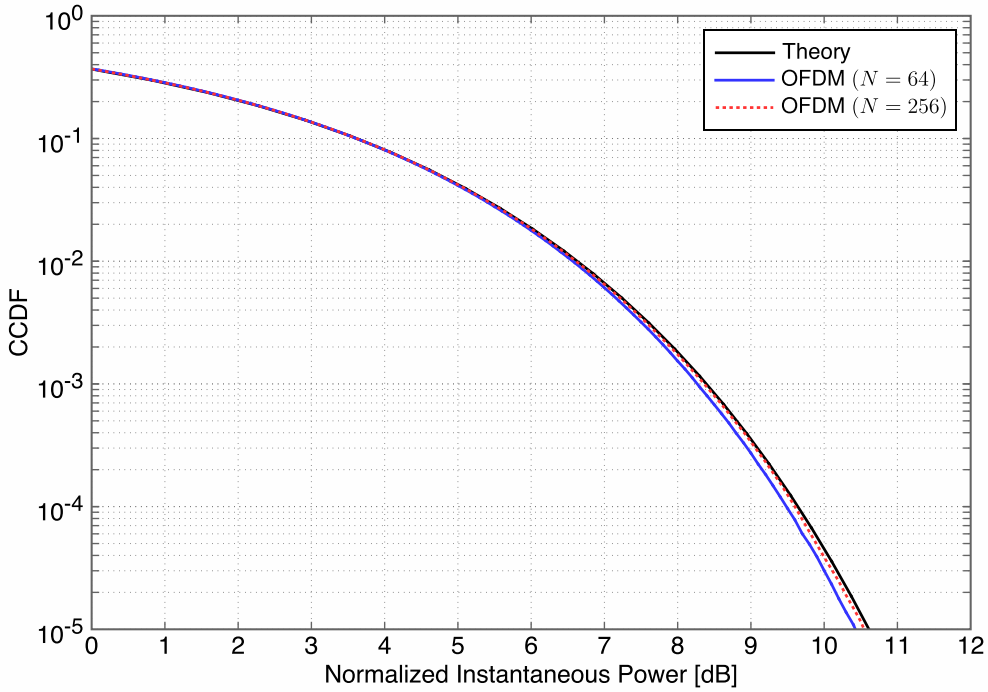

Figure 2.5: CCDF of OFDM signal

The corresponding cumulative distribution function (CDF) can be calculated by integrating (2.31) as

$$F_r(P_k) = \int_0^{P_k} \frac{1}{2\sigma_x^2} e^{-\frac{v}{2\sigma_x^2}} dv = 1 - e^{-\frac{P_k}{2\sigma_x^2}}. \tag{2.32}$$

Consequently, the complementary CDF (CCDF) is

$$\Gamma_r(P_k) = e^{-\frac{P_k}{2\sigma_x^2}}. \tag{2.33}$$

In Fig. 2.5, we see that the CCDF of OFDM signal generated by simulation approaches to theoretical value of (2.33) as the number of subcarriers increases.

From the distribution of OFDM, we see that the Gaussian distribution significantly helps to analyze the signal characteristic. For the case of SC-FDMA, however, since the transmit signal is not Gaussian, it is difficult to derive the closed-form of distribution function [WG05].

2.2.3 Fundamental Analysis of Nonlinear Distortion

Nonlinear distortion affects both inband and out-of-band. Generally, inband distortion degrades the quality of signal such as bit error rate. On the other hand, out-of-band

distortion causes interference over adjacent channel. Most of wireless communication standards have a guard band between channels to prevent adjacent channel interference (ACI). From the view point of frequency resource, the guard band can be wasteful of spectrum. Therefore, it is required to analyze spectral broadening by nonlinear distortion in the initial step of wireless system design.

In this subsection, we briefly describe the influence of nonlinear distortion by analytical approach. For the sake of simplicity, we use third-order polynomial PA model is adopted as nonlinear channel, and assume that the input signal is OFDM which is an ideally band-limited Gaussian random process whose power spectral density is express as

$$S_x(f) = \begin{cases} p_s, & |f| < \frac{W}{2} \\ 0, & \text{otherwise,} \end{cases} \tag{2.34}$$

where W denotes the bandwidth of the input OFDM signal and p_s is a constant that determines its average power such that $P_{\text{in}} = p_s W$.

Autocorrelation Function

The autocorrelation function of the output signal $y(t)$ in (2.25) is expressed as

$$\begin{aligned} R_y(t_1, t_2) &= E\{y(t_1)y^*(t_2)\} \\ &= E\left\{ \sum_{k=0}^{K} \sum_{l=0}^{L} a_{2k+1} a_{2l+1}^* x(t_1) x^*(t_2) |x(t_1)|^{2k} |x(t_2)|^{2l} \right\} \\ &= \sum_{k=0}^{K} \sum_{l=0}^{L} a_{2k+1} a_{2l+1}^* E\left\{ x^{k+1}(t_1) x^l(t_2) \{x^*(t_1)\}^k \{x^*(t_2)\}^{l+1} \right\}, \end{aligned} \tag{2.35}$$

where x^* denotes the complex conjugate of x and $E\{\cdot\}$ is a statistical expectation operation. Since the higher-order terms in (2.35) are less tractable as well as less dominant in the resulting performance, we only focus on the terms up to the third order in what follows. In this case, we have

$$\begin{aligned} R_y(t_1, t_2) = |a_1|^2 E\left\{u_1 u_2^*\right\} + a_1 a_3^* E\left\{u_1 u_2 u_2^* u_2^*\right\} \\ + a_3 a_1^* E\left\{u_1 u_1 u_1^* u_2^*\right\} + |a_3|^2 E\left\{u_1 u_1 u_1^* u_2 u_2^* u_2^*\right\} \end{aligned} \tag{2.36}$$

where $u_1 = x(t_1)$ and $u_2 = x(t_2)$. Since u_1 and u_2 are zero-mean complex Gaussian random variables by assumption, based on the property of moment theorem that holds for a zero-mean complex Gaussian random variable, we have [Ree62]

$$\begin{aligned} E\{u_1 u_2 u_2^* u_2^*\} &= 2E\left\{|u_2|^2\right\} E\{u_1 u_2^*\} \\ E\{u_1 u_1 u_1^* u_2^*\} &= 2E\left\{|u_1|^2\right\} E\{u_1 u_2^*\} \end{aligned} \tag{2.37}$$

and

$$E\{u_1 u_1 u_1^* u_2 u_2^* u_2^*\} = 4E\left\{|u_1|^2\right\} E\left\{|u_2|^2\right\} E\{u_1 u_2^*\} + 2E\{u_1 u_2^*\} E\{u_1^* u_2\} E\{u_1 u_2^*\}. \tag{2.38}$$

Substituting (2.37) and (2.38) into (2.36), we obtain

$$\begin{aligned} R_y(t_1, t_2) = &\left(|a_1|^2 + 2a_1 a_3^* E\left\{|u_2|^2\right\} + 2a_3 a_1^* E\left\{|u_1|^2\right\} + 4|a_3|^2 E\left\{|u_1|^2\right\} E\left\{|u_2|^2\right\}\right) E\{u_1 u_2^*\} \\ &+ 2|a_3|^2 E\{u_1 u_2^*\} \left(E\{u_1 u_2^*\}\right)^* E\{u_1 u_2^*\}. \end{aligned} \tag{2.39}$$

If we assume that $x(t)$ is wide-sense stationary with

$$P_{\text{in}} \triangleq E\left\{|x(t)|^2\right\} = E\left\{|u_1|^2\right\} = E\left\{|u_2|^2\right\} \tag{2.40}$$

and

$$R_x(\tau) = R_x(t, t-\tau) = E\{x(t)x^*(t-\tau)\} = E\{u_1 u_2^*\} \tag{2.41}$$

where $\tau = t_1 - t_2$, then $y(t)$ is also wide-sense stationary and we have

$$R_y(\tau) \triangleq R_y(t, t-\tau) = |a_1 + 2a_3 P_{\text{in}}|^2 R_x(\tau) + 2|a_3|^2 R_x(\tau) R_x^*(\tau) R_x(\tau). \tag{2.42}$$

Power Spectral Density

By Wiener-Khinchin theorem, the PSD of the output signal $y(t)$ can be derived by taking a Fourier transform of the autocorrelation function (2.42) as

$$S_y(f) = |a_1 + 2a_3 P_{\text{in}}|^2 S_x(f) + 2|a_3|^2 S_x(f) \star S_x(-f) \star S_x(f), \tag{2.43}$$

where $\star$ denotes convolution.

By assumption, the PSD of the input signal $S_x(f)$ is rectangular as in (2.34) and thus an even function. Consequently, the convolution term in (2.34) can be expressed in a closed form as

$$S_x(f) \star S_x(f) \star S_x(f) = \begin{cases} \frac{3}{4}p_s^3 W^2 - p_s^3 f^2, & |f| < \frac{W}{2}, \\ \frac{1}{2}p_s^3(\frac{3}{2}W - |f|)^2, & \frac{W}{2} < |f| < \frac{3W}{2}, \\ 0, & \text{otherwise.} \end{cases} \tag{2.44}$$

Finally, if we normalize the bandwidth of the PSD such that $W = 1$ and the resulting PSD by its input power, (2.43) is simplified as

$$\begin{aligned} \tilde{S}_y(f) = \left.\frac{S_y(f)}{P_{\text{in}}}\right|_{W=1} &= |a_1 + 2a_3 P_{\text{in}}|^2 S_1(f) + \frac{1}{2}|2a_3 P_{\text{in}}|^2 S_3(f) \\ &= |a_1|^2 \left\{ |1 + 2\xi|^2 S_1(f) + 2|\xi|^2 S_3(f) \right\} \end{aligned} \tag{2.45}$$

where

$$\xi \triangleq \frac{a_3 P_{\text{in}}}{a_1}, \tag{2.46}$$

$$S_1(f) = \begin{cases} 1, & |f| < \frac{1}{2}, \\ 0, & \text{otherwise,} \end{cases} \tag{2.47}$$

and

$$S_3(f) = \begin{cases} \frac{3}{4} - f^2, & |f| < \frac{1}{2}, \\ \frac{1}{2}(\frac{3}{2} - |f|)^2, & \frac{1}{2} < |f| < \frac{3}{2}, \\ 0, & \text{otherwise.} \end{cases} \tag{2.48}$$

Signal-to-Distortion Power Ratio (SDR)

Note that the first term of the right-hand side of (2.43) or (2.45) corresponds to the useful signal component, i.e.,

$$P_{\text{S}} = |a_1|^2 |1 + 2\xi|^2 \int_{-\infty}^{\infty} S_1(f) df = |a_1|^2 |1 + 2\xi|^2 \tag{2.49}$$

whereas the second term corresponds to the nonlinear distortion that spreads in-band and out-of-band:

$$P_{\mathrm{D}} = |a_1|^2 2\,|\xi|^2 \int_{-\infty}^{\infty} S_3(f)df = 2|a_1|^2\,|\xi|^2 \tag{2.50}$$

We can calculate the signal-to-distortion power ratio (SDR) of the entire bandwidth, which we refer to as *total SDR*, as

$$\mathrm{SDR}_{\text{total}} = \frac{P_{\mathrm{S}}}{P_{\mathrm{D}}} = \frac{|a_1|^2\,|1+2\xi|^2}{2|a_1|^2\,|\xi|^2} = 2\left|1+\frac{1}{2\xi}\right|^2. \tag{2.51}$$

On the other hand, the nonlinear distortion that falls *in-band* can be derived as

$$P_{\mathrm{D,in}} = |a_1|^2 2\,|\xi|^2 \int_{-\frac{1}{2}}^{\frac{1}{2}} S_3(f)df = \frac{4}{3}|a_1|^2\,|\xi|^2\,. \tag{2.52}$$

Consequently, the in-band SDR is calculated by

$$\mathrm{SDR}_{\text{in-band}} = 3\left|1+\frac{1}{2\xi}\right|^2 = \frac{3}{2}\mathrm{SDR}_{\text{total}}. \tag{2.53}$$

This result reveals that the in-band SDR is higher than the total SDR by a factor of $\frac{3}{2}$ (1.76 dB). Also, it is apparent that the center subcarrier suffers from higher distortion compared to the edge subcarriers, and the difference in distortion can be calculated as

$$\frac{S_3(0)}{S_3\left(\frac{1}{2}\right)} = \frac{3}{2} \tag{2.54}$$

which also suggests that the difference between the maximum and minimum SDR is $\frac{3}{2}$ (1.76 dB).

From (2.51), we observe that the nonlinearly amplified signal is affected only by the amount $\xi = a_3 P_{\text{in}}/a_1$, which depends on the input signal power P_{in}. Therefore, the accurate estimation of this term can largely determine the resulting PSD of the nonlinearly amplified OFDM signals with near rectangular spectra. In the next section, we propose a method to estimate this term based on the alternative estimation of the SDR from the AM-AM and AM-PM of a given power amplifier model.

Error Vector Magnitude

Finally, we remark the relationship between the error vector magnitude (EVM) and the SDR derived above. The EVM is commonly used as a measure for specifying distortion and other impairments mostly caused by nonlinear circuits in many communication systems. Recent wireless communication standard adopts EVM constraints in order to guarantees the quality of the transmit signal in accordance with each modulation type. Generally, EVM is defined as [Och13]

$$\text{EVM} \triangleq \sqrt{\frac{E\left\{\left|\tilde{X}_k - \lambda_{X,\text{opt}} X_k\right|^2\right\}}{E\left\{\left|\lambda_{X,\text{opt}} X_k\right|^2\right\}}} \times 100[\%] \tag{2.55}$$

where X_k is a reference M-QAM (or M-PSK) symbol, $\tilde{X}_k$ is the received signal with additive white Gaussian noise (AWGN) and nonlinear distortion caused by nonlinear amplification at PA, and the corresponding compensation factor $\lambda_{X,\text{opt}}$ is given by

$$\lambda_{X,\text{opt}} = \frac{E\left\{X_k^* \tilde{X}_k\right\}}{E\left\{|X_k|^2\right\}}. \tag{2.56}$$

It can be shown that the EVM can be directly related to the in-band SDR as [Och13]

$$\text{EVM} = \sqrt{\frac{1}{\text{SDR}_{\text{in-band}}}} \times 100[\%]. \tag{2.57}$$

Therefore, calculating EVM is equivalent to calculating in-band SDR, which can be pursued by the approach given in the previous subsection.

Chapter 3

Experimental Analysis of the Effectiveness of Clipping and Filtering for OFDM Systems

3.1 Introduction

One of the well-known drawbacks of the OFDM signal is its high peak-to-average power ratio (PAPR). The envelope of OFDM signal may frequently exceed saturation level of power amplifier (PA) and cause nonlinear distortion if the input back-off (IBO) is not large enough. Nonlinear distortion not only degrades the performance of OFDM, but also causes out-of-band radiation that leads to adjacent channel interference (ACI). On the other hand, if the IBO of PA is increased, it will considerably reduce the PA efficiency.

In order to solve such a problem, many of experimental studies have been performed to investigate and improve the trade-off relationship between the quality of the signal and efficiency of PA, which are roughly categorized into PA linearization and PAPR reduction. The PA linearization technique improves linearity of nonlinear PA and thereby enhances the efficiency of PA for given amount of nonlinear distortion. The digital predistortion (DPD) is a widely used approach that compensates for PA nonlinearity and look up table (LUT) is commonly applied [Li+09; car+10]. In [Li+09], the authors proposed multi-level LUT and improved the convergence time with eight times faster at 64 LUT size than traditional LUT method while maintaining error and adjacent channel power ratio (ACPR) performance the same as traditional one. Alternatively, the method to enhance the linearity region of PA using two nonlinear PAs, often referred to as linear amplification with nonlinear component (LINC) [car+10], is also effective

to suppress nonlinear distortion. In [car+10], a LINC algorithm is proposed that has a fast convergence rate, and in addition, not only the ACI is significantly reduced but also inband distortion caused by PA is mitigated.

These approaches require the knowledge of the characteristic of a given PA and additional hardware. To the contrary, the baseband PAPR reduction technique is attractive due to its simplicity. Moreover, these two approaches can be combined to further improve the overall PA efficiency.

A number of the peak power reduction techniques have been introduced for OFDM systems (e.g.,[HL05; JW08]). Among them, the clipping and filtering (CAF) [LC98] is attractive due to its simplicity. The peak envelope can be adjusted by clipping ratio to a certain level that meets the system requirement. Furthermore, sidelobe power is suppressed by the filtering and thus the adjacent channel interference (ACI) is reduced.

The clipping process, however, also introduces nonlinear distortion referred to as a clipping noise. As a result, it causes degradation of the signal quality. The filtering process also causes a slight increase of the envelope level. In [OI02], the authors evaluate the channel capacity degradation and the peak power reduction capability of the clipped OFDM signal in AWGN and fading channel with and without oversampling. Oversampling before clipping process is effective in suppressing peak power regrowth, improving capacity and bit error performance. In [Bah+02], the performance of the clipped OFDM systems is analyzed with the assumption that the clipping is a rare event. Overall performance of signal clipping without filtering using PA model is investigated in terms of total degradation in [TPZ05]. It has been shown that the signal clipping may not be necessarily effective if total degradation and spectral dispersion are taken into account.

In order to measure nonlinear distortion caused by nonlinear process and analog devices such as PA or digital-to-analog converter (DAC), the error vector magnitude (EVM) is widely adopted in recent wireless communication standards such as IEEE 802.11 (WLAN) or IEEE 802.16 (WiMAX). Especially, since the clipping process introduces the nonlinear distortion, it is necessary to guarantee the quality of signal by means of maximum acceptable EVM. Additionally, after filtering process, the peak power will be increased compared to the target envelope level designed by the clipping ratio. As a result, additional nonlinear distortion is caused in PA. There are a number of significant research results such as achievable PAPR or the evaluation of

clipping distortion in CAF with computer simulation. On the other hand, the experimental studies based on a real PA that examine the validity of CAF are rather scarce. In this chapter, therefore, we investigate the validation of the clipped and filtered OFDM signal by evaluating the efficiency of PA, EVM and ACI with computer simulation and experiment using real PA.

Our contributions are as follows :

- Estimating the quality of the clipped and filtered OFDM signal : As mentioned above, the nonlinear distortion affects both inband and out-of-band of the transmit signal. Since inband distortion is directly related with bit error performance, its mitigation has been widely studied. In [JT02], the magnitude and phase of the clipped signal are limited by threshold to improve resultant EVM. As a result, inband distortion is significantly compensated while the peak power regrows, and it may introduce additional nonlinear distortion by PA. The channel coding is a key solution even in the condition that EVM is relatively high. The optimum code rate can be determined by the cutoff rate [Pro01] with respect to signal-to-noise ratio (SNR).

- Measuring the power efficiency : Considering that PA is the most power-hungry component in wireless communication system, it is important to reduce power consumption of PA. In [SSC11], the authors take advantages of companding signal with μ-law as peak power reduction technique as well as an adaptive PA for reducing power consumption. The signal companded with μ-law may have reduced its peak power, that is, it is assured that amplification is performed only in linear region, but the EVM is increased by companding process. In this work, we measure the power efficiency of clipping and filtering with constant gain of PA through the experimental setup. From the viewpoint of power efficiency, the CAF is remarkably effective. The CAF reduces not only the dynamic range of signal amplitude but also its average power. The signal input level (or amplitude) of PA without nonlinear distortion is limited in terms of peak envelope rather than average power. In other words, for a predetermined maximum envelope level of real PA and under the limited signal quality constraints such as EVM and ACI, we can increase the transmit power, thus improving the power efficiency through the CAF. The question what we aim to answer in this work is how effective the CAF is in OFDM system using real PA, which has the quality constraint such as EVM and/or ACI. Also, since the CAF requires no major modification of the

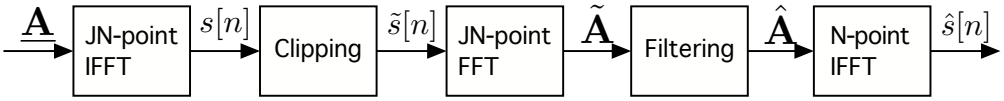

Figure 3.1: A block diagram of clipping and filtering

receiver side, it is directly applicable to commercial products if its performance improvement is outstanding.

Thus we also investigate the performance of the CAF based on the setup of IEEE 802.11g WLAN standard system through the real PA implementation.

This chapter is organized as follows. The clipping and filtering system model is described in Section 3.2. Theoretical analysis and signal estimating method are discussed in Section 3.3. The experimental testbed is described in Section 3.4 and the experiment and numerical results are described in 3.5. Finally conclusion is drawn in Section 3.6.

3.2 System Model

There are several approaches of implementing CAF and throughout this chapter we focus on the implementation proposed in [OI02]. Other approaches may yield a similar result.

3.2.1 Clipping

The clipping process is composed of JN-point discrete Fourier transform (DFT) as shown in Fig. 3.1, where J is an oversampling factor and N is the number of modulated subcarriers, respectively. It is common in many standards that the DC component of the baseband signal is set as NULL symbol. The data sequence is then expressed as

$$\underline{\mathbf{A}} = \{\underbrace{0, A_0, A_1, \ldots,}_{N/2}\ \underbrace{0, 0, \ldots, 0, 0}_{(J-1)\times N \text{ zeros}},\ \underbrace{\ldots, A_{N-2}, A_{N-1}}_{N/2}\}. \tag{3.1}$$

Subsequently, $\underline{\mathbf{A}}$ goes to input of JN-point inverse DFT (IDFT) and we can obtain the oversampled OFDM signal $s[n]$ in time domain as

$$s[n] = \underbrace{\sqrt{J}\frac{1}{\sqrt{JN}}\sum_{k=0}^{JN-1} A_k e^{j2\pi nk/JN}}_{\triangleq \text{IDFT}(\underline{\mathbf{A}}, JN)_n}. \tag{3.2}$$

The oversampled OFDM signal $s[n]$ is then clipped as

$$s_c[n] = \begin{cases} s[n], & \text{for } |s[n]| \leq A_{\max}, \\ A_{\max} e^{j \arg s[n]}, & \text{for } |s[n]| > A_{\max}. \end{cases} \tag{3.3}$$

Clipping ratio (CR) γ is defined by the maximum amplitude to the root mean square (rms) value of input signal $s[n]$ given by

$$\gamma = \frac{A_{\max}}{\sqrt{P_{\text{in}}}}, \tag{3.4}$$

where $A_{\max}$ is the maximum clipping amplitude and P_{in} is the average power of the input signal, $s[n]$.

It is well-known fact that OFDM signal follows a Gaussian distribution, and the average power of transmit signal after the clipping process can be expressed as

$$P_{\text{out}} = (1 - e^{-\gamma^2}) P_{\text{in}}. \tag{3.5}$$

3.2.2 Filtering

The filtering process eliminates the out-of-band power dispersion (sidelobe power growth) caused by clipping process. The former DFT converts the clipped signal $\tilde{s}$ to the frequency domain components $\tilde{\mathbf{A}}$ expressed as

$$\tilde{\mathbf{A}} = \{\underbrace{0, \tilde{A}_0, \tilde{A}_1, \ldots}_{N/2} \underbrace{\tilde{A}_{N/2-1} \ldots \tilde{A}_{JN-N/2}}_{out-of-band} \underbrace{\ldots \tilde{A}_{JN-2}, \tilde{A}_{JN-1}}_{N/2}\}. \tag{3.6}$$

Finally, we can obtain the filtered OFDM signal by using N-point IDFT excluding out-of-band components in (3.6). [1]

$$\hat{s}[n] = IDFT(N, \tilde{\mathbf{A}})_n \tag{3.7}$$

[1] In the case of ERP-OFDM in IEEE 802.11g stnadard, it has 12 NULL subcarriers as a guard band allocated in the borders between in- and out-of-band in order to minimize the ACI. In our experiment of Section 3.5, we also set them as zeros in filtering process.

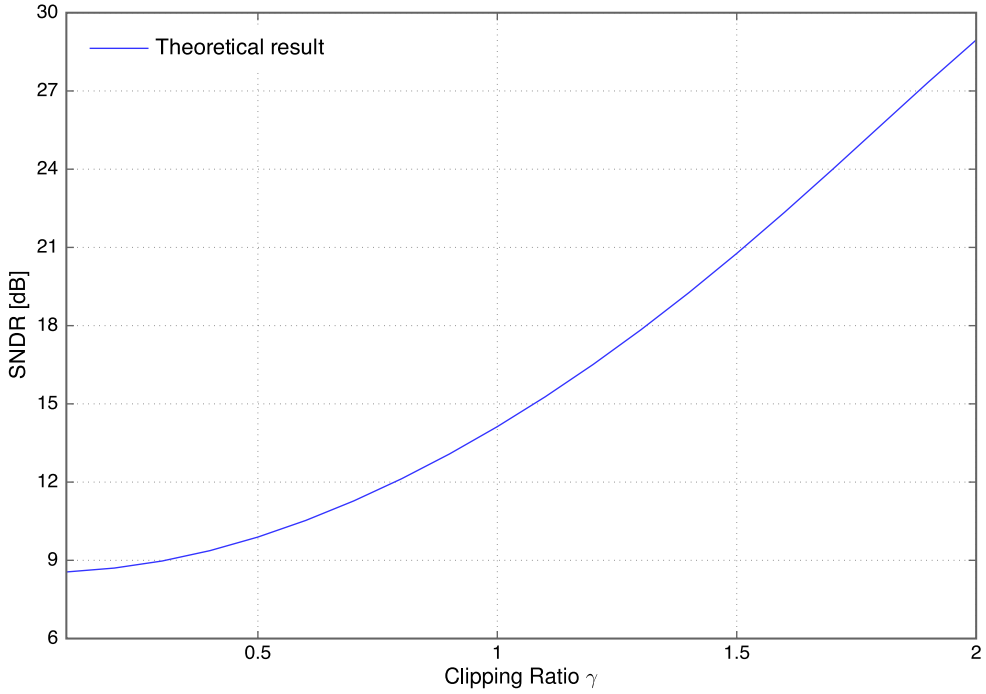

Figure 3.2: Signal-to-noise plus distortion ratio vs. clipping ratio

3.3 Theoretical Analysis

In this section, we approach theoretical analysis of nonlinear distortion caused by the clipping process and analog devices such as PA and DAC. Measurement methods are also described.

3.3.1 Signal-to-Noise plus Distortion Ratio (SNDR)

By Bussgang's theorem and Gaussian approximation, the distorted symbol on the kth subcarrier of OFDM signal can be approximated by (see [OI02] and references therein)

$$\tilde{A}_k = \alpha_c A_k + D_k, \tag{3.8}$$

where D_k is nonlinear component in frequency domain. Since D_k is uncorrelated with A_k, the expected value of $|\tilde{A}_k|^2$ can be expressed as

$$\begin{aligned} E\{|\tilde{A}_k|^2\} &= E\{|\alpha_c A_k + D_k|^2\} \\ &= \alpha_c^2 E\{|A_k|^2] + E[|D_k|^2\}, \end{aligned} \tag{3.9}$$

where $E[\cdot]$ is expected value, α_c is attenuation factor, k is subcarrier index. From (3.9), we can define the signal-to-distortion ratio (SDR) of the kth subcarrier as

$$\text{SDR}_k = \frac{\alpha_c^2 E\{|A_k|^2\}}{E\{|D_k|^2\}}. \tag{3.10}$$

The theoretical value of the SDR for the oversampled and clipped OFDM signal can be derived by using the power spectral density and its autocorrelation given by [OI02; CMP99]

$$\text{SDR}_k = \frac{K_\gamma p_{in,k}/P_{in}}{\frac{1}{\sqrt{JN}}\text{DFT}(JN, \{R_{\tilde{s}}[n]/P_{out}\})_k - K_\gamma p_{in,k}/P_{in}} \tag{3.11}$$

where $p_{in,k}$ is the signal power of $\mathbf{A}$ in kth subcarrier, $R_{\tilde{s}}[n]$ is autocorrelation of the clipped signal $\tilde{s}[n]$ and K_γ is a normalized attenuation factor defined as

$$K_\gamma = \frac{\alpha_c^2 P_{c,in}}{P_{c,out}} = \frac{\alpha_c^2}{1 - e^{-\gamma^2}} \tag{3.12}$$

where the attenuation factor α_c in clipping process is given by

$$\alpha_c = 1 - e^{-\gamma^2} + \frac{\sqrt{\pi}\gamma}{2}\text{erfc}(\gamma) \tag{3.13}$$

However, the transmit signal also suffers from the channel noise and other impairments as an additional noise term. Given this fact, we consider the signal-to-noise plus distortion ratio (SNDR) which is related with given SDR in (3.11), and defined for the kth subcarrier by [OI02]

$$\text{SNDR}_k = \frac{E[|\alpha_c A_k|^2]}{E[|D_k + W_k|^2]} = \frac{1}{\text{SDR}_k + B} \tag{3.14}$$

where

$$B = \text{SNR}^{-1}\left(1 + \frac{1}{N}\sum_{k=0}^{N-1}\text{SDR}_k^{-1}\right) \tag{3.15}$$

3.3.2 Cutoff Rate

The cutoff rate R_0 serves as a measure for achievable information rate of code word error rate assuming a certain class of channel codes. It can be represented for the

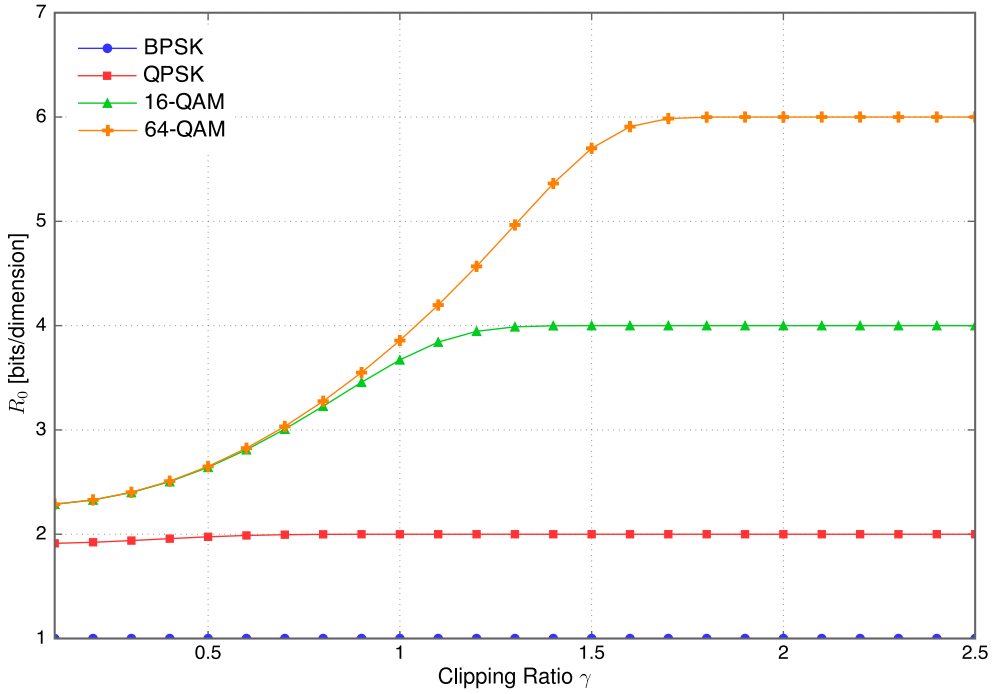

Figure 3.3: Cutoff rate vs. clipping ratio for various modulation type

equally likely symbol given by [Pro01]

$$R_0 = -\log_2\left(\frac{1}{M^2}\sum_{l=1}^{M}\sum_{m=1}^{M} e^{-d_{lm}^2/4N_0}\right) \tag{3.16}$$

where d_{lm} is the Euclidean distance between A_l and A_m and N_0 is the noise power. With this definition, we can derive the upper bound of code word error rate for M-QAM and M-PSK symbol. As an example, the upper bound for QPSK can be derived as

$$R_{0:QPSK} = \log_2 \frac{4}{1 + 2e^{-\epsilon_c/2N_0} + e^{-\epsilon_c/N_0}} \tag{3.17}$$

where the ϵ_c is the average power of signal. Assuming that N_0 denotes the clipping noise D_k and thermal noise in circuit, then ϵ_c/N_0 in (3.17) can be replaced in terms of SDR on the kth subcarrier, and consequently, the cutoff rate R_0 can be rewritten as follow

$$R_{0:QPSK} = \log_2 \frac{4}{1 + 2e^{-\mathrm{SNDR}_k/2} + e^{-\mathrm{SNDR}_k}}. \tag{3.18}$$

Using the relation between (3.14) and (3.16), we can obtain the relationship between the cutoff rate R_0 and clipping ratio γ as shown in Fig. 3.3. In the case of coding rate $R = 1/2$ and $R = 3/4$ for 64-QAM, for instance, the resulting information bits are 3bits and 4.5bits, and thus the minimum acceptable clipping ratio γ is easily derived

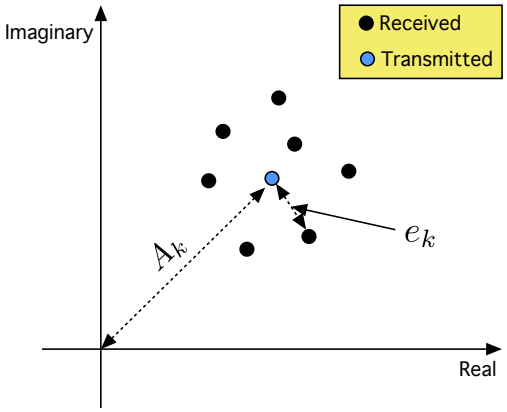

Figure 3.4: General EVM measurement.

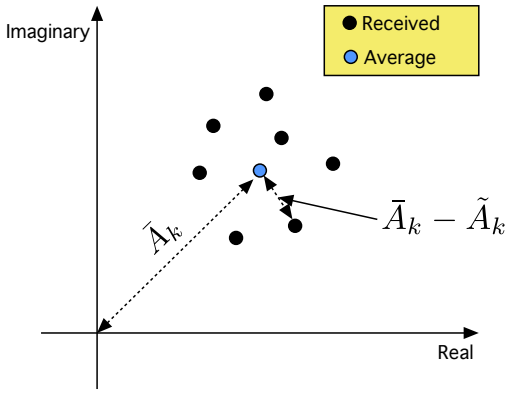

Figure 3.5: Experimental EVM measurement.

as approximately 0.7 and 1.2, respectively. On the other hand, in the case of BPSK and QPSK, the cutoff rate results are almost constant and the same as $\log_2 M$ for the entire clipping ratio range. This means that the bit error rate can be mitigated by moderate channel coding even if the clipping ratio is chosen as zero.

3.3.3 Error Vector Magnitude (EVM)

The EVM is used as a measure for specifying nonlinear distortion and other impairments mostly caused by circuits in many systems. Recent wireless communication standard adopts EVM constraints in order to guarantee the quality of the transmit signal in accordance with each modulation type. Generally, EVM is defined as

$$\text{EVM} = \frac{1}{N}\sum_{k=0}^{N-1}\sqrt{\frac{E[|D_k|^2]}{E[|\alpha A_k|^2]}} \times 100[\%], D_k = A_k - \tilde{A}_k \tag{3.19}$$

where A_k is a reference M-QAM (or M-PSK) symbol on the kth subcarrier, $\tilde{A}_k$ is the received signal with additive white Gaussian noise (AWGN) and nonlinear distortion caused by deliberate clipping as well as nonlinear amplification by PA, and D_k corresponds to an error vector as illustrated in Fig. 3.4. Since the average power of the received OFDM signal is changed by clipping process and power amplification, and thus the reference symbol A_k and the received symbol $\tilde{A}_k$ have mismatch in terms of their average power. Therefore it is reasonable to measure for EVM by modifying the definition (3.19) as

$$\text{EVM} = \frac{1}{N}\sum_{k=0}^{N-1}\sqrt{\frac{E[|\bar{A}_k - \tilde{A}_k|^2]}{E[|\bar{A}_k|^2]}} \times 100[\%] \tag{3.20}$$

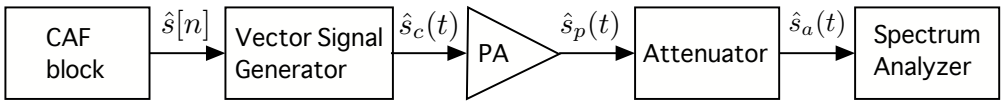

Figure 3.6: Block diagram of experiment configuration

where $\bar{A}_k$ is the mean value of the received signal. This definition is quite appropriate as long as the statistical distribution of $\tilde{A}_k$ (conditioned on the transmitted symbol A_k) is circularly symmetric with respect to its mean $\bar{A}_k$.

As an alternative measure of EVM, SNDR can be adopted. Based on the relationship between (3.14) and (3.20), EVM can be rewritten in terms of SNDR as

$$\text{EVM} = \frac{1}{N}\sum_{k=0}^{N-1}\sqrt{\frac{E[|D_k + W_k|^2]}{E[|\alpha A_k|^2]}} = E\left\{\sqrt{(\text{SNDR}_k)^{-1}}\right\} = \sqrt{(\text{SNDR})^{-1}} \tag{3.21}$$

3.4 Testbed Description

In this section, we describe the testbed used in our experiment for applying CAF to IEEE 802.11g standard in Section 3.5. Measurement in hardware relies on the specification and the characteristic of hardware, and only embedded measurement function can be available. On the other side, data acquisition to be measured is performed in hardware (i.e., real time spectrum analyzer (RSA)), then the data is analyzed in software to be able to manipulate by user. There is little significant difference between hardware measurement and software one [AN10]. In this work, we also use software measurement with down-converted acquisition data from RSA.

Figure 3.1, and 3.6 show the system block diagram of our testbed. First, the clipped and filtered ERP-OFDM baseband signal is generated using computer and then fed to the vector signal generator, where CAF process is applied to the entire frame excluding the short preambles that are designed to have a low PAPR. The detailed testbed description is provided in Appendix B.

The discrete ERP-OFDM data is converted to analog signal by digital-to-analog converter (DAC) with 16-bit precision. Since the SDR_q with regard to quantization noise can be calculated as [Hay01]

$$\text{SDR}_q = \left(\frac{P_{\text{avg}}}{\text{PAPR}_{\max}}\right) \times 2^{2R} \tag{3.22}$$

Table 3.1: Power Amplifier Specification

Gain	30 dB
Frequency Band	2 – 3000 Mhz
Output Power (P1dB)	29 dBm
Noise Figure	8 dB

where P_{avg} is the average power, $\text{PAPR}_{\max}$ is the maximum peak power to be predicted and R is the quantization bits per sample, we have $\text{SDR}_q \approx 89$ dB in our experiment configuration with $\text{PAPR}_{\max} = 12$ dB and $R = 16$. Therefore, this is large enough to confirm that the quantization noise is negligible. The output signal of DAC is up-converted to the 2.4 GHz carrier frequency with 20 MHz bandwidth, which complies with the IEEE 802.11g standard. The RF signal $\hat{s}_c(t)$ from the vector signal generator is amplified by the PA.

The specification of the PA used in this testbed is given in Table 3.1 and Table 3.2 shows the modulation and coding parameters, resulting data rate, and their acceptable EVM limit specified by the IEEE 802.11g standard.

In order to measure the performance achieved by CAF under the constraints such as spectral mask and EVM described in Table 3.2, we adjust the average power of the clipped and filtered signal $\hat{s}_c(t)$ prior to PA (i.e., input back-off) in Fig. 3.1. Finally, the amplified RF signal $\hat{s}_p(t)$ is linearly attenuated (as $\hat{s}_a(t)$) and measured by the spectrum analyzer. The down-converted baseband signal is captured by this spectrum analyzer and the received data is analyzed by computer.

3.4.1 The Power Amplifier Model

In general, nonlinearity caused by PA distorts both amplitude and phase. For example, if we define the power amplifier input signal as

$$s_{pi}(t) = s(t)e^{j\phi(t)} \tag{3.23}$$

then the signal amplified and/or distorted by PA can be represented by

$$s_{po}(t) = \xi(s_{pi}(t))e^{j(\phi(t)+\Phi(t))} \tag{3.24}$$

where $\xi(\cdot)$ is AM/AM conversion and $\Phi(\cdot)$ is AM/PM conversion. Among the several PA model, we use well-known solid state power amplifier model called Cann

Table 3.2: EVM constraints (a) IEEE 802.11g and (b) Cutoff rate in various modulation type

Modulation	Code rate (R)	EVM constraint	
		IEEE 802.11g	Cutoff rate
BPSK	1/2	56.2%	>100%
	3/4	39.8%	77.7%
QPSK	1/2	31.6%	74.9%
	3/4	22.3%	54.9%
16-QAM	1/2	15.8%	43.1%
	3/4	11.2%	27.7%
64-QAM	2/3	7.9%	18.8%
	3/4	5.6%	15.5%

model[Can80], which is also well-known as Rapp model[Rap91]. They can be easily transformed each other with simple algebraic manipulation[TPZ05]. Cann model is expressed as

$$\xi(s_{pi}(t)) = g_0 \frac{A_{sat}}{[1 + (A_{sat}/s_{pi}(t))^{2p}]^{1/2p}}, \ \Phi(t) = 0 \tag{3.25}$$

where g_0 is amplification gain, A_{sat} is saturation level of PA and p is sharpness factor which determines the smoothness of the curve.

3.5 Applying CAF to IEEE 802.11g System

Generally, communication standard has constraints to guarantee the quality of signal such that the resulting error rate is tolerable. In this section, we verify the performance of the CAF by applying to IEEE 802.11g system [Ieea; Vas+05] which has backward compatibility with IEEE 802.11a [Ieeb] and strict constraints on both of EVM and power spectral density. Since the cutoff rate suggests the achievable code rate for channel coding, once the code rate is defined, we can redefine the EVM constraints based on the cutoff rate. After some algebraic manipulation of (3.14) and (3.16), we can obtain the relationship between the cutoff rate and the corresponding maximum acceptable EVM results shown in Fig. 3.7. Also, Table 3.2 shows the EVM constraints defined by (a) IEEE 802.11g standard and (b) cutoff rate. Based on these two constraints, we evaluate the performance of CAF in IEEE 802.11g system using simulation and experiment with real power amplifier.

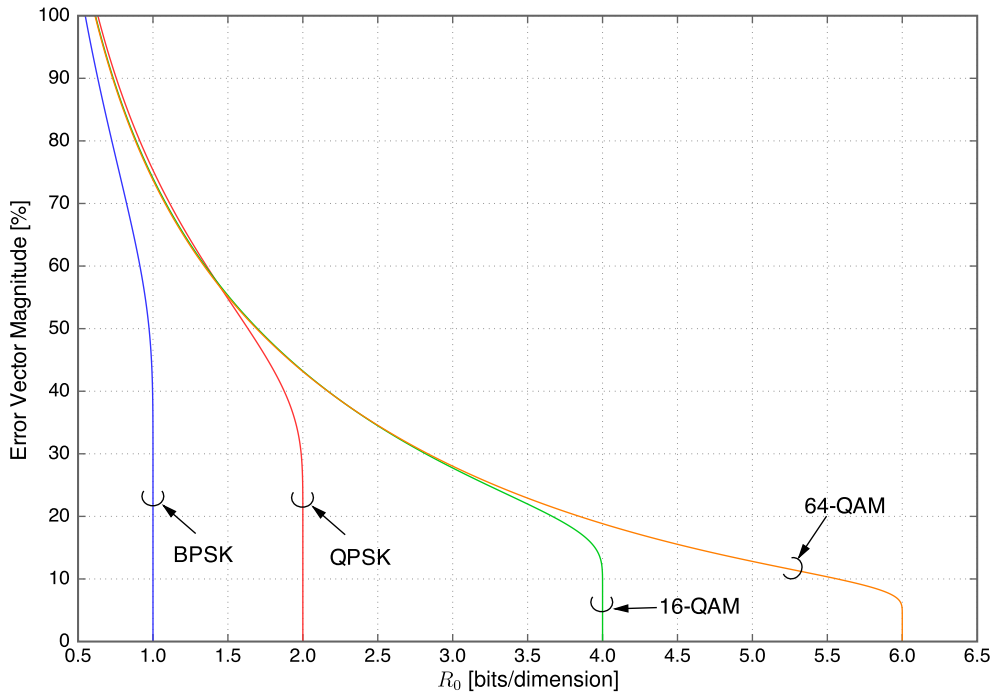

Figure 3.7: The relationship between EVM and cutoff rate with various modulation type

3.5.1 Peak Power Reduction

Figure 3.8 shows the CCDF result of instantaneous power normalized by the saturation power of PA. Since the peak envelope directly affects the nonlinear distortion caused by PA, it is more reasonable to investigate instantaneous power rather than the PAPR. Clearly, as clipping ratio decreases, peak power reduces as well. For example, we can achieve about 5 dB peak power reduction effect at 10^{-5} probability by setting the clipping ratio as 1.0 in comparison with unclipped one. We can readily obtain the probability of the signal to be distorted by PA by applying IBO setting drawn with vertical dashed line. In other words, IBO setting can be treated as saturation point of PA because the instantaneous power is normalized by saturation power of PA, thus right side area of the dashed line is considered as the nonlinear amplification area of PA. Most of peak envelope will be distorted when IBO is set as low value (e.g., IBO = 1 dB in the figure). However, the probability to be distorted becomes significantly lower as clipping ratio decreases. From this result, we can confirm that the clipped and filtered signal rarely causes additional nonlinear distortion while the unclipped signal easily exceeds the saturation point.

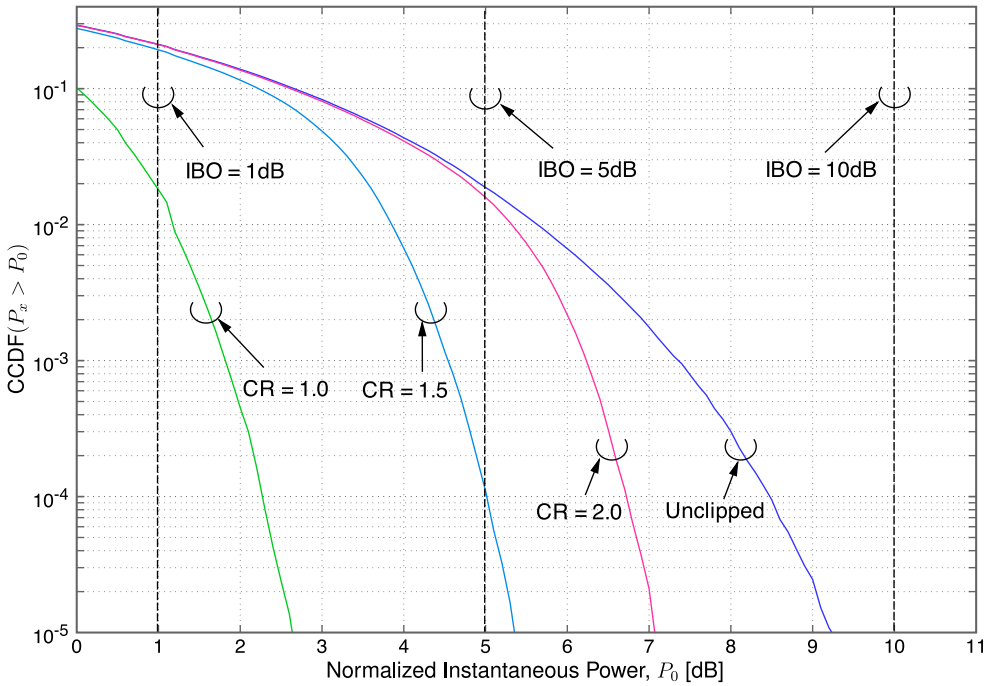

Figure 3.8: Peak power reduction effect of the clipped and filtered OFDM signal. $N = 64, J = 4$

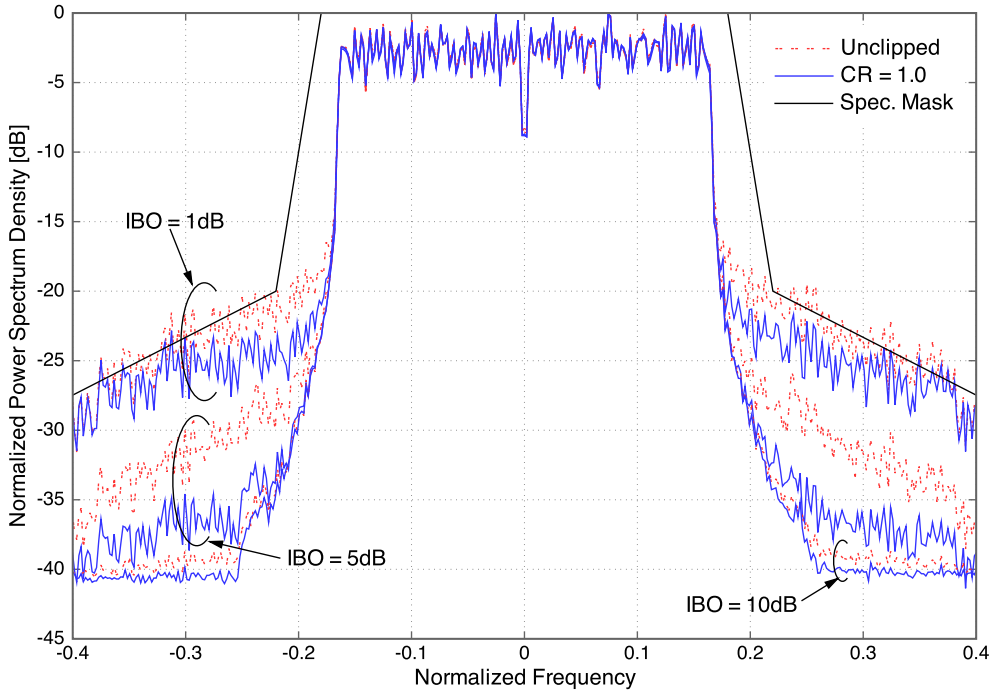

Figure 3.9: Experimental results of power spectral density; (IBO = 1, 5, 10 dB) and (CR = 1.0, unclipped), respectively

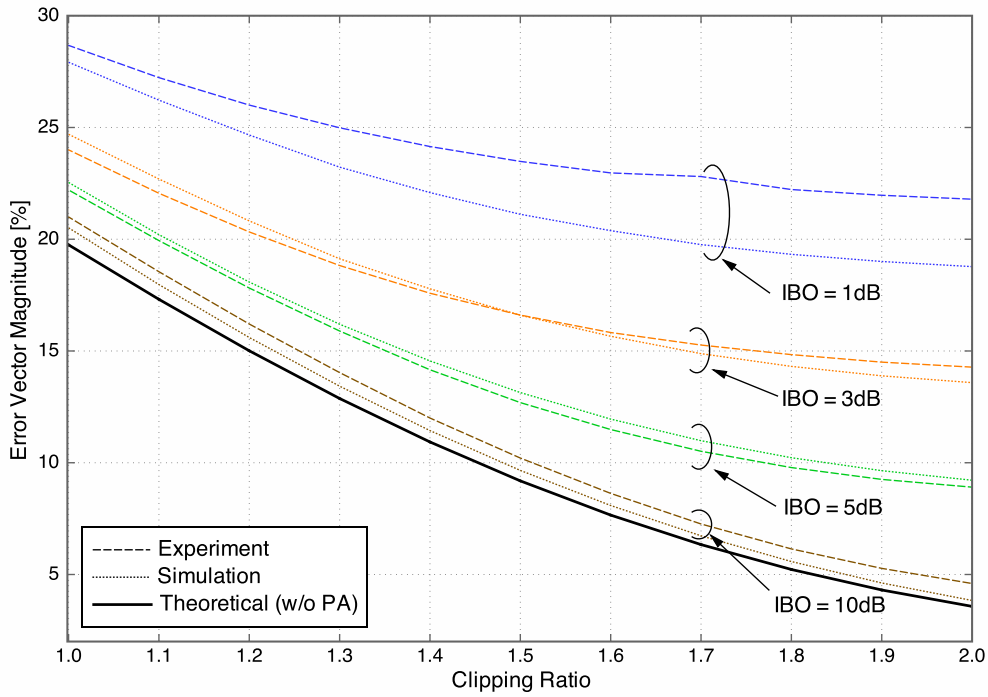

Figure 3.10: Experimental results of EVM against clipping ratio with various IBO through theoretical (SNR = 35 dB), computer simulation and experiment

3.5.2 Adjacent Channel Power Reduction

Figure 3.9 compares the power spectral density results when IBO of PA is chosen as 1 dB, 5 dB, and 10 dB as indicated in Fig. 3.8. Since nonlinear distortion is rarely caused when IBO is as high as 10 dB, the sidelobe power is almost the same level for both clipped ($\gamma = 1.0$) and unclipped signals. On the other hand, the gap becomes significant as IBO is reduced. This is due to the fact that the clipped signal causes less nonlinear distortion in power amplifier than unclipped one When IBO = 5 dB, for example, there is 5 dB gap of sidelobe power between clipped and unclipped signal. In extremely low IBO, however, the nonlinear distortion caused by PA becomes dominant for both clipped and unclipped cases, and thus the gap becomes smaller again.

3.5.3 EVM and IBO for Clipping Ratio

Since bit error is frequently caused by increasing the modulation order, that is, shortening the euclidean distance, IEEE 802.11g standard has defined different EVM constraint as modulation type changes. Figure 3.10. shows the EVM results on various IBO values for each clipping ratio on IEEE 802.11g system through the computer simulation (twin line), experiment using real PA (solid line) and theoretical analysis (dashed

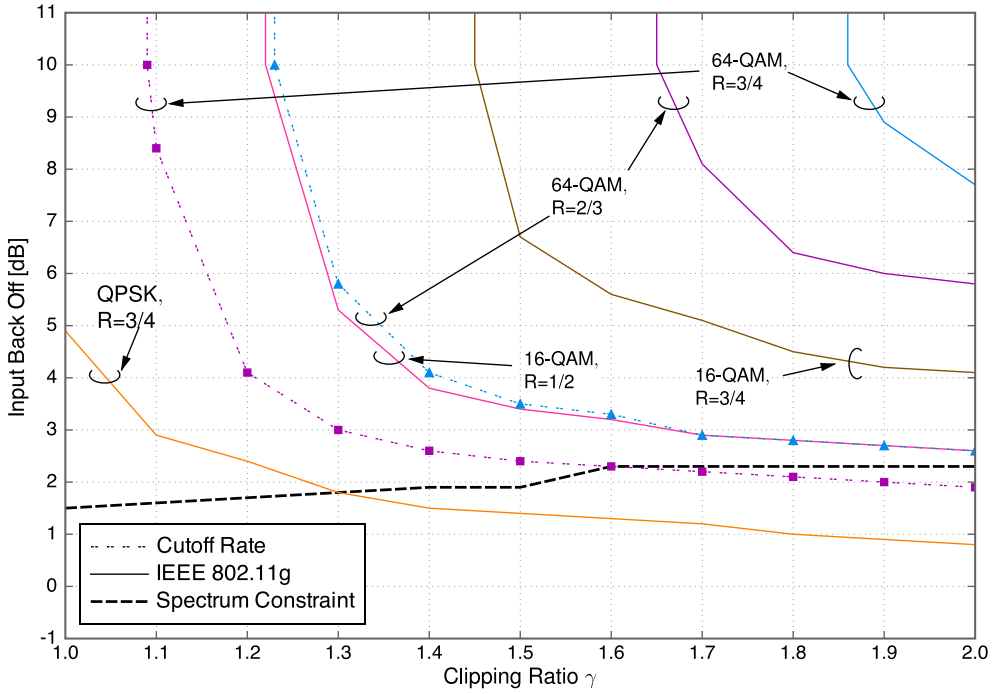

Figure 3.11: Applicable range of clipping ratio and IBO for the various modulation type under the constraints (EVM and spectral mask) of both (a) IEEE 802.11g and (b) cutoff rate

line). Since clipping process is nonlinear type of peak power reduction nonlinear distortion (say clipping noise) is caused by itself. As a result, as clipping ratio is reduced, resultant EVM increases. Theoretical value derived from SNDR (SNR = 35 dB) in (3.14) and (3.21) introduces the boundary which is the minimum CR under the given IBO and EVM constraints of each transmission mode. As expected, the EVM increases as IBO is reduced. This is due to the fact that peak signal envelope frequently exceeds the saturation point of PA when IBO is low, so that the additional nonlinear distortion is caused. The resultant EVM approaches the theoretical value in the case of sufficiently large IBO (e.g., IBO = 10 dB), which is the case where the signal is linearly amplified by PA. From these results, we can obtain the minimum IBO (maximum average power) for each transmission mode from Fig. 3.10 and Table. 3.2. In the case of 64-QAM and code rate $R = 2/3$, for example, since its EVM constraint of IEEE 802.11g standard is 7.9% from Table 3.2 (a), we can achieve the minimum clipping ratio of approximately 1.7 at IBO = 10 dB. On the other hand, if we choose the EVM constraint of cutoff rate as 18.8 % which is less severe than IEEE 802.11g standard, then the minimum clipping ratio is 1.1 at IBO = 10 dB. Also, we can reduce IBO, that is, enabling to amplify the signal more efficiency by PA, if we set larger clipping ratio.

3.5.4 EVM under Spectral Constraints

Applying the spectral constraint to the EVM results in Fig. 3.10, the acceptable pair of CR and IBO becomes different. Figure 3.11 shows the relationship between EVM results under spectral constraint in terms of clipping ratio and input back off. In high transmission mode (16-QAM and 64-QAM), the clipped and filtered signal does not reach to the spectral constraint since the EVM constraints of IEEE 802.11g standard are severe due to the required error rate performance. Consequently, the signal is governed by the EVM constraint rather than the spectral constraint. On the other hand, in low transmission mode (BPSK and QPSK), it is governed by the spectral constraint rather than EVM constraint excluding QPSK with code rate $R = 3/4$. In other words, the minimum IBO for each clipping ratio is the same as the spectral limit line in Fig. 3.11. In the case of QPSK with code rate $R = 3/4$, it is subject to both EVM and spectral constraints. For example, if the clipping ratio is higher than 1.4, the spectral constraint becomes dominant and thus one should increase the iBO of PA, even though its EVM is lower than the maximum acceptable value that is suggested by the error rate.

On the other hand, if we apply the constraint of cutoff rate from Table. 3.2 (b), applicable range of the clipping ratio is enlarged. Therefore the corresponding IBO curve of 64-QAM shown in Fig. 3.11 is expanded with wider clipping ratio. Consequently, under the transmission rate of 16-QAM, only the spectrum constraint affects the signal.

3.5.5 Power Increase Effect by CAF

We can measure the power efficiency by estimating the transmit power increase. Since the CAF shrinks the dynamic range of the transmit signal, the peak envelope which is clipped with lower clipping ratio is amplified less frequently in nonlinear area of PA than higher CR or unclipped one. In addition, once the signal is amplified in nonlinear area, the signal energy is reallocated in out-of-band, and thus the transmit power is significantly reduced. Figure 3.12 shows the inband power increase of transmit signal to unclipped one against clipping ratio under the condition that the EVM result of both the clipped and unclipped signal is satisfied according to Table 3.2. We can confirm from the result that as IBO decreases, the transmit power is increased in lower transmission mode such as BPSK and QPSK.

When we apply the EVM constraints of (b) the cutoff rate, the inband power of 64-QAM is slightly increased as observed from the twin lines in Fig. 3.12. However, the

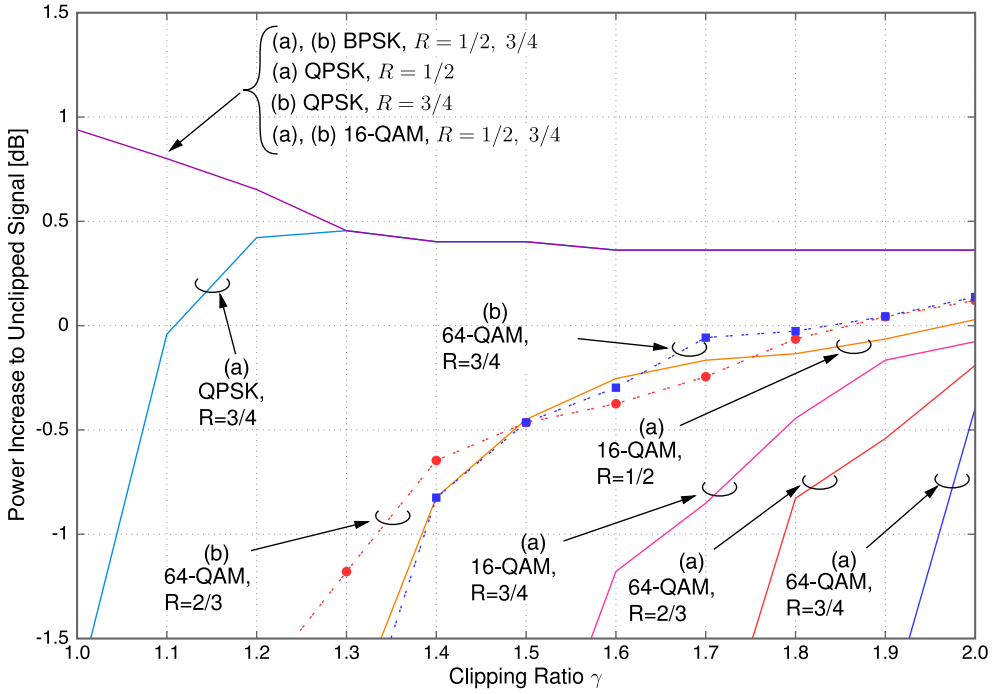

Figure 3.12: Power increase effect to unclipped signal under the inherited condition of Fig. 3.11

rest of the corresponding results is limited by spectral constraint, so that we can achieve 1 dB inband power increase in the same manner as BPSK and QPSK modulation of (a) IEEE 802.11g standard at 1.0 of clipping ratio.

3.6 Conclusion

We have investigated the effectiveness of clipping and filtering and evaluated its performance by applying to IEEE 802.11g WLAN system. The improvement of PA efficiency and received signal power can be achieved through the clipping and filtering in low rate mode transmission. However, when the EVM is strictly limited as in the case of high rate mode transmission, the CAF may not help improving the overall performance. Therefore, in this case, the CAF should be combined with other power efficiency improvement techniques without any increase of EVM such as distortionless peak power reduction schemes.

Chapter 4

Characterization of Power Spectral Density for Nonlinearly Amplified OFDM Signals

4.1 Introduction

As the mobile terminals become smaller while meeting their demand for communication with even higher data rate, the future wireless communication signals should satisfy high bandwidth efficiency without sacrificing power efficiency. Orthogonal frequency-division multiplexing (OFDM) signaling has gained significant attention due to its high bandwidth efficiency and robustness against frequency-selective fading channels. However, its well-known drawback is the high peak-to-average power ratio (PAPR) property of the resulting signals. High PAPR signal is difficult to amplify without sacrificing its power conversion efficiency at the linear power amplifier (PA). In order to maximize PA efficiency, it is essential to adjust the input signal to be amplified mostly around the saturation region. This PA operation introduces severe nonlinear distortion which degrades the signal quality, and in turn increases bit error rate (BER). In addition, it also introduces out-of-band radiation which causes adjacent channel interference (ACI). On the other hand, when we set the operation point of the PA much lower than its saturation point, it suffers from a severe power penalty. This is a well-known trade-off between the PA efficiency and the quality of transmit signals [Lia+99; Och13], a salient issue for the OFDM systems that exhibit highest PAPR among many communication systems.

The PA models are categorized into strictly memoryless, quasi-memoryless, and memory [BG89]. The output signal of strictly memoryless PA models (e.g., Rapp model

[Rap91]) depends only on the amplitude-to-amplitude (AM-AM) characteristic while that of the quasi-memoryless PA models (e.g., Saleh model [Sal81]) depends on both the AM-AM and amplitude-to-phase (AM-PM) characteristics.

Most wireless communication standards such as IEEE 802.11 wireless LAN strictly regulate the permissible spectral sidelobe levels in order to avoid ACI and thus enhance overall spectral efficiency of the multi-user systems. The error vector magnitude (EVM) is another measure that characterizes the performance degradation caused by nonlinearity due to the system impairments and often restricted by the specification. The EVM is an alternative measure for a ratio of the power of the received signal to that of the *in-band* distortion and noise [Och13; YBZ12]. Therefore, from the viewpoint of communication system designers, it may be helpful if performance measures such as power spectral density (PSD) and EVM of the PA output signal are easily predicted or estimated.

The PSD of the signals affected by the nonlinearity of the PA has been extensively studied, mostly in conjunction with the OFDM signals that can be characterized as a band-limited complex Gaussian process. For example, in [GGS99; Erm01], based on the autocorrelation function of memoryless PA output signal, the out-of-band spectrum has been theoretically analyzed and good agreement with the experimental result has been observed. In [ZR04; Zho00], using cumulant expression as a generalization of the autocorrelation function, the closed-form polynomial expression is derived. In [BC00], the spectrum estimation is performed by autocorrelation function with curve fitting by a series of Bessel function. More recently, the nonlinearity analysis has been extended to the MIMO-OFDM signals [KD11; Ahm+13; LST14] as well as the degradation in terms of channel capacity[SST].

One of the major issues associated with the above-mentioned approaches is how to accurately model a given PA. In principle, any well-behaved nonlinear function can be approximated by Taylor series expansion or a series of special functions, but reducing the residual error in the estimated PSD requires an addition of higher order terms. Incorporating higher order terms, in turn, makes the analysis complicated or even mathematically intractable.

In this work, we propose an approach to develop a *simple* model that can accurately characterize the PSD and EVM of the resulting OFDM signals. Our approach is based on the use of the cross-correlation coefficient between the input and output signals from the PA, which can be easily calculated from its AM-AM and AM-PM characteristics and

input back off operation. This cross-correlation coefficient is directly related to the concept of the total signal-to-distortion power ratio (SDR) discussed in [Och13]. Here, we emphasize that unlike conventional curve fitting approaches, our approach does not necessarily require the precise expressions for the AM-AM and AM-PM curves of a given PA in order to characterize the resulting PSD and EVM. The accuracy of the proposed approach is confirmed by simulation as well as an experimental measurement using a real PA.

The major contributions of this work are summarized as follows: 1) We theoretically establish the link among the cross-correlation coefficient, total SDR as well as in-band SDR (or EVM), and the resulting PSD. In particular, the effect of the higher-order distortion terms is theoretically analyzed for two representative and analytically tractable nonlinear models. 2) We propose a simple PSD estimation approach that only makes use of the cross-correlation coefficient and the spectral shape of the third-order distortion. 3) The effectiveness of our approach is verified by both simulation and measurement using real PA with OFDM signal input. As is common in the statistical analysis of OFDM signals [BC00; Erm01; OI01; ZR04; WGK10], the PA input signal is assumed to be a zero-mean circular symmetric stationary complex Gaussian process [Gar] throughout this work.

This chapter is organized as follows. A general mathematical expression of PSD for nonlinearly amplified Gaussian signals in terms of the correlation coefficients of input signals is described in Section 4.2, followed by its examination through two specific nonlinearity examples in Section 4.3. In Section 4.4, the proposed estimation of PSD based on the cross-correlation coefficient of input and output signals is developed and its application to OFDM signaling is discussed. The simulation and experimental results are compared with those based on the proposed theoretical approach in Section 4.5. Finally, the concluding remarks are given in Section 4.6.

4.2 PSD Expression of Nonlinearly Amplified Gaussian Signals

4.2.1 Input Signal Model

Throughout this chapter, we assume that a complex baseband signal $z_i(t)$ input to the PA is characterized as a zero-mean circular symmetric stationary complex Gaussian process, which is considered as an accurate model for OFDM signals with a large number of subcarriers. It then follows that $z_i(t)$ is expressed as

$$z_i(t) = x_i(t) + jy_i(t) = r(t)e^{j\theta(t)}, \tag{4.1}$$

where $r(t) = |z_i(t)|$, $\theta(t) = \arg z_i(t)$, $x_i(t) = \Re\{z_i(t)\}$, and $y_i(t) = \Im\{z_i(t)\}$. By assumption, $x_i(t)$ and $y_i(t)$ can be considered as statistically independent real-valued zero-mean Gaussian processes. The autocorrelation function of a stationary process $z_i(t)$ can be defined as

$$R_{z_i}(\tau) \triangleq E\{z_i(t)z_i^*(t+\tau)\} \tag{4.2}$$

where $E\{\cdot\}$ denotes an expectation operator. The corresponding correlation coefficient can be expressed as

$$\rho_{z_i}(\tau) \triangleq \frac{E\{z_i(t)z_i^*(t+\tau)\}}{\sqrt{E\{|z_i(t)|^2\}E\{|z_i(t+\tau)|^2\}}} = \frac{R_{z_i}(\tau)}{P_{\text{in}}}, \tag{4.3}$$

where

$$P_{\text{in}} = R_{z_i}(0) = E\left\{|z_i(t)|^2\right\} = E\left\{r^2(t)\right\} \tag{4.4}$$

is the average power of $z_i(t)$. It also follows that

$$\rho_{z_i}(\tau) = \rho_{x_i}(\tau) = \frac{E\{x_i(t)x_i(t+\tau)\}}{E\{x_i^2(t)\}} \tag{4.5}$$

where $\rho_{x_i}(\tau)$ is a real-valued correlation coefficient, and thus $\rho_{z_i}(\tau)$ is a real-valued function as well, satisfying $-1 \leq \rho_{z_i}(\tau) \leq 1$.

4.2.2 Correlation Coefficient of Output Signals

In principle, the amplitude and phase distortions associated with a PA depend only on the amplitude of input signal envelope $r(t)$ [ZR04], and the corresponding output baseband signal $z_o(t)$ from the PA can be expressed as

$$z_o(t) = g[r(t)]e^{j\{\phi[r(t)]+\theta(t)\}} = G[r(t)]e^{j\theta(t)}, \tag{4.6}$$

where $g[\cdot]$ and $\phi[\cdot]$ denote the AM-AM and AM-PM conversions, respectively, and the complex gain is defined as

$$G(r) = g(r)e^{j\phi(r)}. \tag{4.7}$$

Following the results by Blachman [Bla79], when the input signal is expressed as a complex stationary Gaussian process, the correlation coefficient of the output signal $z_o(t)$ can be expressed in terms of the correlation coefficient of the input signal $\rho_{z_i}(\tau) = \rho_{x_i}(\tau)$ as

$$\rho_{z_o}(\tau) = \frac{R_{z_o}(t)}{P_{\text{out}}} = \frac{P_{\text{in}}}{P_{\text{out}}}\sum_{n=0}^{\infty} C_n \rho_{x_i}^{2n+1}(\tau) = \sum_{n=0}^{\infty}\frac{C_n}{\xi}\rho_{x_i}^{2n+1}(\tau) \tag{4.8}$$

where

$$R_{z_o}(\tau) = E\{z_o(t)z_o^*(t+\tau)\}, \tag{4.9}$$

$$P_{\text{out}} = R_{z_o}(0) = E\left\{|z_o(t)|^2\right\} = E\left\{g^2(r)\right\}, \tag{4.10}$$

$$\xi \triangleq \frac{P_{\text{out}}}{P_{\text{in}}}. \tag{4.11}$$

The coefficient $C_n \in \mathbb{R}$ associated with the $(2n+1)$th order term is expressed as [Bla79]

$$C_n = \frac{1}{(n+1)P_{\text{in}}}\left|\int_0^{\infty} p(r)G(r)\frac{r}{\sqrt{P_{\text{in}}}}L_n^{(1)}\left(\frac{r^2}{P_{\text{in}}}\right)dr\right|^2, \tag{4.12}$$

where $p(r)$ is the probability density function (PDF) of the input envelope $r(t) = |z_i(t)|$, which follows Rayleigh distribution, and expressed as

$$p(r) = \frac{2r}{P_{\text{in}}}e^{-r^2/P_{\text{in}}}. \tag{4.13}$$

(The above PDF assumption is valid for the OFDM system without PAPR reduction. When the PAPR of input signal is reduced before power amplification, the use of other

distributions, e.g., [YGP11], may result in more accurate result.) The function $L_n^{(m)}(z)$ in (4.12) is the generalized Laguerre polynomial [Olv10], which can be expressed in a polynomial form for a non-negative integer m as

$$L_n^{(m)}(z) = \sum_{k=0}^{n} \binom{n+m}{n-k} \frac{(-z)^k}{k!} \tag{4.14}$$

where

$$\binom{a}{b} = \frac{a!}{b!(a-b)!}. \tag{4.15}$$

Note that in the case of $n = 0$, since $L_0^{(m)}(x) = 1$ for any x, (4.12) reduces to

$$C_0 = \frac{1}{P_{\text{in}}^2} \left| E\left\{ rG(r) \right\} \right|^2 \tag{4.16}$$

and thus

$$\frac{C_0}{\xi} = \frac{\left| E\left\{ rG(r) \right\} \right|^2}{E\left\{ r^2 \right\} E\left\{ g^2(r) \right\}} = |\rho_{z_i,z_o}|^2 \tag{4.17}$$

where $\rho_{z_i,z_o} \in \mathbb{C}$ corresponds to the cross-correlation coefficient of $z_i(t)$ and $z_o(t)$:

$$\rho_{z_i,z_o} = \frac{E\{z_i(t)z_o^*(t)\}}{\sqrt{E\{|z_i(t)|^2\}E\{|z_o(t)|^2\}}} = \frac{E\{z_i(t)z_o^*(t)\}}{\sqrt{P_{\text{in}}P_{\text{out}}}}. \tag{4.18}$$

4.2.3 PSD of Output Signals

As a consequence of Bussgang theorem [Row82], the output autocorrelation function of a nonlinearly transformed Gaussian signal is decomposed as a sum of the scaled version of the autocorrelation function of the input signal and that of the distortion component uncorrelated with the input signal. It thus follows that the term with $n = 0$ in (4.8), or equivalently, (4.17) represents the useful signal component and the remaining terms correspond to distortion. In fact, taking Fourier transform of (4.8) gives the *normalized* PSD, which is expressed as

$$S_{z_o}(f) = \int_{-\infty}^{\infty} \rho_{z_o}(\tau) e^{-j2\pi f\tau} d\tau = \sum_{n=0}^{\infty} \frac{C_n}{\xi} S_{x_i}^{\star(2n+1)}(f), \tag{4.19}$$

where $S_{x_i}(f)$ is the PSD of the input signal directly obtained by Fourier transform of the correlation coefficient of input signal ρ_{x_i} given by

$$S_{x_i}(f) = \int_{-\infty}^{\infty} \rho_{x_i}(\tau) e^{-j2\pi f\tau} d\tau, \tag{4.20}$$

and $S_{x_i}^{\star(m)}$ denotes the self-convolution process with m times, i.e.,

$$S_{x_i}^{\star(m)}(f) \triangleq \underbrace{S_{x_i}(f) \star \cdots \star S_{x_i}(f)}_{m}, \tag{4.21}$$

with $\star$ corresponding to convolution operation. We also note that due to the normalization, we have

$$\int_{-\infty}^{\infty} S_{x_i}^{\star(m)}(f) df = 1 \tag{4.22}$$

for any positive integer m.

In principle, once the input signal PSD $S_{x_i}(f)$ and C_n are known, the output PSD can be determined through the above equations. In the case of OFDM, it is reasonable to assume that the PSD is rectangular, and in this case the closed-form expression can be obtained for their self-convolution terms as will be discussed in Section 4.4.4. On the other hand, the coefficient C_n involves the nonlinear function $G(r)$ and whether it can be given in a tractable form or not depends on the mathematical structure of $G(r)$.

4.3 Examples of Distortion Coefficients for Nonlinearly Amplified Gaussian Signals

In this section, we examine the effect of sharpness and smoothness of the nonlinearity on the resulting PSD by analyzing the coefficients C_n/ξ in (4.19). The two specific example AM-AM models, i.e., soft envelope limiter model and erf model, are considered as our representative examples.

4.3.1 Analysis of Coefficients

By substituting (4.13) into (4.12), we obtain

$$C_n = \frac{1}{(n+1)P_{\text{in}}} \left| \sum_{k=0}^{n} \frac{(-1)^k}{k!} \binom{n+1}{n-k} \int_0^\infty G(r) \frac{2r^{2+2k}}{P_{\text{in}}^{k+\frac{3}{2}}} \exp\left(-\frac{r^2}{P_{\text{in}}}\right) dr \right|^2 . \tag{4.23}$$

In general, except for some special cases of $G(r)$, (4.23) should be numerically calculated. The soft envelope limiter model and erf model turn out to result in analytically tractable expressions, where the former serves as an example of sharpest nonlinearity (but perfectly linear up to the saturation point) and the latter as a smooth nonlinearity (but severer in terms of amount of distortion [RQZ05]). These nonlinearity functions (including those described later in Section 4.5) are compared in Fig. 2.4.

Soft Envelope Limiter Model

The soft envelope limiter model is defined as

$$G(r) = g(r) = \begin{cases} r, & r < A_{\max}, \\ A_{\max}, & r \geq A_{\max}, \end{cases} \tag{4.24}$$

where $A_{\max}$ denotes the maximum envelope level of input signal where it is linearly amplified. Note that without loss of generality, the amplifier gain is normalized to unity and the AM-PM characteristic is absent (i.e., $\phi(r) = 0$) in this model. The clipping process is controlled by the input back off (IBO) (or clipping ratio) $\gamma = A_{\max}/\sqrt{P_{\text{in}}}$. By substituting (4.24) into (4.23) and after some algebra (see Appendix A), we obtain

$$C_n = \frac{1}{(n+1)} \left| \sum_{k=0}^{n} \binom{n+1}{k+1} \frac{(-1)^k}{k!} \left\{ \Gamma(2+k) + \gamma\Gamma\left(\frac{3}{2}+k, \gamma^2\right) - \Gamma(2+k, \gamma^2) \right\} \right|^2 \tag{4.25}$$

where $\Gamma(a, b)$ is the incomplete gamma function given by

$$\Gamma(a, b) = \int_b^\infty x^{a-1} e^{-x} dx, \tag{4.26}$$

and $\Gamma(a) = \Gamma(a, 0)$. Note that in [BC00], a recursive expression of C_n for the soft envelope limiter is derived. On the other hand, from (4.25), one may directly obtain the

following form:

$$C_n = \frac{1}{(n+1)}\left|\sum_{k=0}^{n}(-1)^k\frac{(n+1)!}{(n-k)!}\left\{1-\left(1+\sum_{l=1}^{k+1}\left[\frac{1}{l!}-\frac{F_k}{(\frac{1}{2})_l}\right]\gamma^{2l}\right)e^{-\gamma^2} + F_k\sqrt{\pi}\gamma\text{erfc}(\gamma)\right\}\right|^2 \tag{4.27}$$

where $\text{erfc}(x) = 1 - \text{erf}(x)$ is the complementary error function with the error function $\text{erf}(x)$ defined as

$$\text{erf}(x) = \frac{2}{\sqrt{\pi}}\int_0^x e^{-t^2}dt, \tag{4.28}$$

$(a)_k$ is the Pochhammer symbol [Olv10] given by

$$(a)_k = \frac{\Gamma(a+k)}{\Gamma(a)} = a(a+1)(a+2)\cdots(a+k-1) = \prod_{l=0}^{k-1}(a+l), \tag{4.29}$$

and

$$F_k \triangleq \prod_{m=0}^{k}\frac{2m+1}{2m+2}. \tag{4.30}$$

Equation (4.27) states that C_n can be expressed by the square of linear combinations of terms $\gamma^{2l}e^{-\gamma^2}$ and $\gamma\text{erfc}(\gamma)$ for $l = 0, 1, \ldots$ The first three coefficients are calculated as

$$C_0 = \left|1 - e^{-\gamma^2} + \frac{\sqrt{\pi}}{2}\gamma\text{erfc}(\gamma)\right|^2, \tag{4.31}$$

$$C_1 = \frac{1}{8}\left|\gamma^2 e^{-\gamma^2} + \frac{\sqrt{\pi}}{2}\gamma\text{erfc}(\gamma)\right|^2, \tag{4.32}$$

$$C_2 = \frac{1}{768}\left|6\gamma^2 e^{-\gamma^2} - 4\gamma^4 e^{-\gamma^2} + 3\sqrt{\pi}\gamma\text{erfc}(\gamma)\right|^2. \tag{4.33}$$

The output power can be derived by using (4.10) and the output/input power ratio ξ is given by

$$\xi = \frac{P_{\text{out}}}{P_{\text{in}}} = 1 - e^{-\gamma^2}. \tag{4.34}$$

Erf Model

The erf model is defined as [Och13; Gal59]

$$G(r) = g(r) = A_{\max}\text{erf}\left(\frac{\sqrt{\pi}}{2}\frac{r}{A_{\max}}\right), \tag{4.35}$$

where $A_{\max}$ in this case corresponds to the maximum output envelope level if the power gain is normalized to unity.

By substituting (4.35) into (4.23), C_n can be expressed using $\gamma = A_{\max}/\sqrt{P_{\text{in}}}$ as

$$C_n = \frac{1}{n+1}\left|\sum_{k=0}^{n}\begin{pmatrix} n+1 \\ k+1 \end{pmatrix}(-1)^k(k+1)\,{}_2F_1\left(\frac{1}{2}, k+2; \frac{3}{2}; -\frac{\pi}{4}\frac{1}{\gamma^2}\right)\right|^2 \tag{4.36}$$

where ${}_2F_1(a, b; c; z)$ is the hyper-geometric function [Olv10], and can be expressed as the following infinite series expression:

$$C_n = \frac{1}{n+1}\left|\sum_{k=0}^{n}\binom{n+1}{k+1}(-1)^k\sum_{l=0}^{\infty}\binom{k+l}{l}\frac{k+l+1}{2l+1}(-1)^l\left(\frac{\pi}{4\gamma^2}\right)^l\right|^2. \tag{4.37}$$

The infinite series in the above expression rapidly converges when γ is not too small and thus easy to calculate in the case of a practical operation scenario. Finally, the output/input power ratio ξ can be calculated as [Och13]

$$\xi = \frac{4}{\pi}\frac{\gamma^2}{\sqrt{1+\frac{4}{\pi}\gamma^2}}\arctan\left(\frac{1}{\sqrt{1+\frac{4}{\pi}\gamma^2}}\right). \tag{4.38}$$

4.3.2 Discussion

Figures 4.1 (a) and (b) show the relationship between C_n/ξ and γ_{dB} in the case of soft envelope limiter model and erf model, respectively, where the IBO here is defined as $\gamma_{\text{dB}} \triangleq 20\log_{10}\gamma$. As expected from (4.17) and (4.18), since the correlation between the input and output signals becomes higher as we increase IBO, the effective signal term (C_0) increases, whereas the other terms that represent residual distortions decrease. In the case of the soft envelope limiter, when γ_{dB} is low, the third-order distortion term (C_1) becomes dominant, but as γ_{dB} increases, higher-order terms eventually dominate. This particular behavior is mostly specific to the case of the soft envelope limiter which

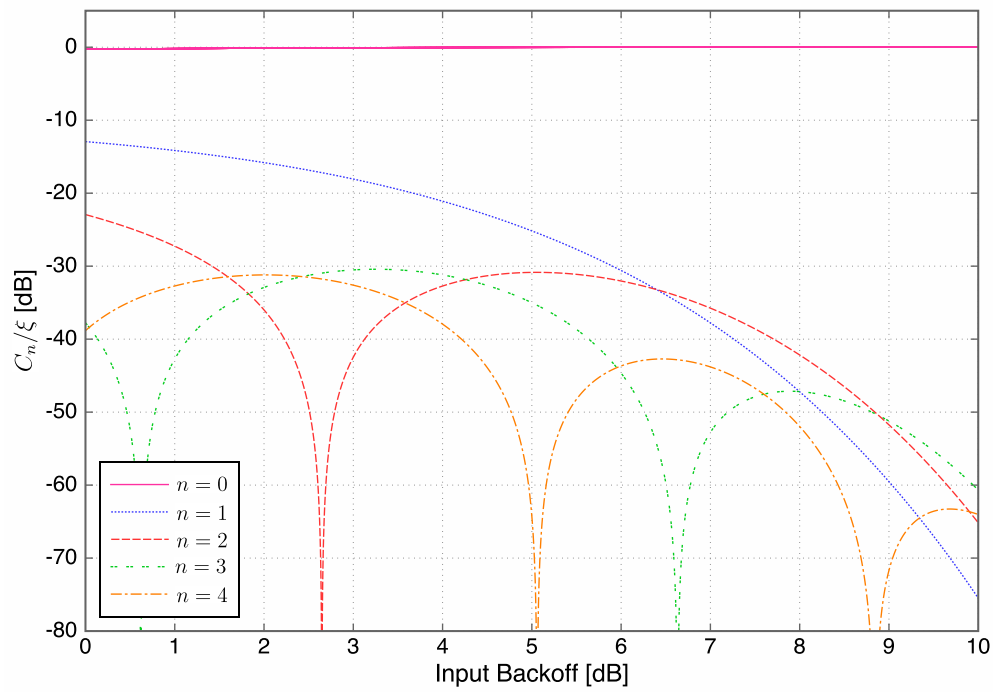

(a)

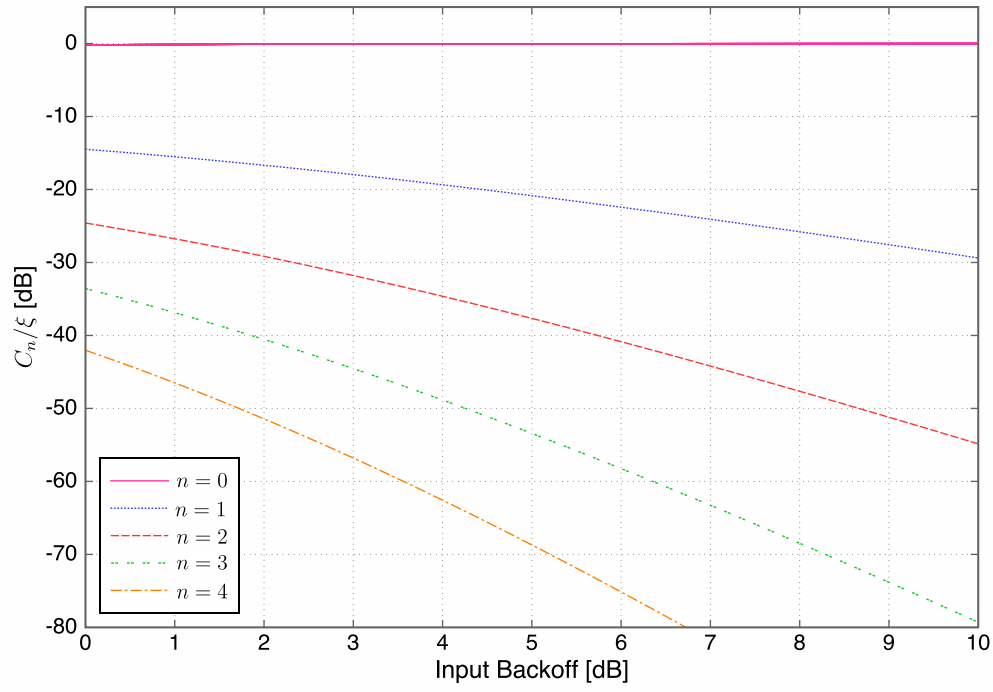

(b)

Figure 4.1: The relationship between higher-order nonlinear distortion components C_n/ξ and input back off for (a) soft envelope limiter model and (b) the erf model.

has a piecewise linear characteristic such that the envelope undergoes severe nonlinearity at the saturation point. On the other hand, in the case of the erf model, the third-order distortion term (C_1) is always dominant and higher-order terms become

less dominant, and this holds almost regardless of the IBO value. Therefore, for many practical amplifiers that have smooth nonlinearity, the third-order term may be considered as the most effective factor in the PSD analysis.

4.4 Simple Expressions for Approximate PSD and EVM Upper Bound

In this section, we first establish the relationship between the nonlinearity behavior and signal-to-distortion power ratio under the assumption of Gaussian input signals. We will then develop a simple approach that does not require any curve fitting but still can estimate the PSD as well as the resulting in-band distortion even if the function $G(r)$ is only partially measured or the signal-to-distortion power ratio is known only at the detector.

4.4.1 Total Signal-to-Distortion Power Ratio

From (4.19) and (4.22), we observe that the total signal power after nonlinear amplification is expressed as

$$\int_{-\infty}^{\infty} S_{z_o}(f)df = \sum_{n=0}^{\infty} \frac{C_n}{\xi} \int_{-\infty}^{\infty} S_{x_i}^{\star(2n+1)}(f)df = \sum_{n=0}^{\infty} \frac{C_n}{\xi} = 1 \tag{4.39}$$

where the first term $n = 0$ corresponds to the useful signal component and the others correspond to distortion. Therefore, the total signal-to-distortion power ratio (SDR) can be defined as

$$\text{SDR}_{\text{total}} \triangleq \frac{C_0/\xi}{\sum_{n=1}^{\infty} C_n/\xi} = \frac{C_0/\xi}{1 - C_0/\xi} = \frac{|\rho_{z_i,z_o}|^2}{1 - |\rho_{z_i,z_o}|^2} \tag{4.40}$$

where ρ_{z_i,z_o} is defined in (4.17). This is referred to as a *design* SDR in [Och13] and can be easily calculated through the measurement of only the cross-correlation coefficient (4.18).

4.4.2 Effective Signal-to-Distortion Power Ratio

As mentioned in [Och13], the total SDR defined above contains both in-band and out-of-band distortion components, whereas the in-band distortion is only a dominant

factor for detection of the data. Thus, the *effective* SDR may be defined based on the in-band distortion component only. To this end, we divide the power spectra corresponding to the order $n \geq 1$ into the in-band and out-of-band components as

$$\int_{-\infty}^{\infty} S_{x_i}^{\star(2n+1)}(f)df = \underbrace{\int_{\mathcal{D}_{\text{in}}} S_{x_i}^{\star(2n+1)}(f)df}_{\beta_{n,\text{in}}} + \underbrace{\int_{\mathcal{D}_{\text{out}}} S_{x_i}^{\star(2n+1)}(f)df}_{\beta_{n,\text{out}}} = 1 \tag{4.41}$$

where $\mathcal{D}_{\text{in}}$ and $\mathcal{D}_{\text{out}}$ represent the frequency regions corresponding to in-band and out-of-band, respectively.

The effective SDR is then defined as

$$\text{SDR}_{\text{eff}} \triangleq \frac{C_0/\xi}{\sum_{n=1}^{\infty} \beta_{n,\text{in}} C_n/\xi}. \tag{4.42}$$

We denote the most dominant in-band spectral component as

$$\beta_{*,\text{in}} = \max_{n \geq 1} \beta_{n,\text{in}}. \tag{4.43}$$

Then we have

$$\text{SDR}_{\text{eff}} \geq \frac{C_0/\xi}{\beta_{*,\text{in}} \sum_{n=1}^{\infty} C_n/\xi} = \frac{1}{\beta_{*,\text{in}}} \text{SDR}_{\text{total}}. \tag{4.44}$$

The EVM can be then upper-bounded by

$$\text{EVM} = \sqrt{\frac{1}{\text{SDR}_{\text{eff}}}} \leq \sqrt{\frac{\beta_{*,\text{in}}}{\text{SDR}_{\text{total}}}}. \tag{4.45}$$

4.4.3 Simple Approximate Expression of Power Spectral Density using Cross-Correlation Coefficient

In Section 4.3.2, we have seen that in both the cases of smooth and sharp (including piecewise linear) nonlinearity, the third-order component (C_1/ξ) is a dominant factor of distortion. Using this fact, we establish the simple approximate PSD expression based only on the input/output cross-correlation coefficient and the PSD of input signals.

First, let us express (4.19) as

$$S_{z_o}(f) = \frac{C_0}{\xi} S_{x_i}(f) + \sum_{n=1}^{\infty} \frac{C_n}{\xi} S_{x_i}^{\star(3)}(f) + \underbrace{\sum_{n=2}^{\infty} \frac{C_n}{\xi} \left\{ S_{x_i}^{\star(2n+1)}(f) - S_{x_i}^{\star(3)}(f) \right\}}_{\delta(f)}. \tag{4.46}$$

Since in general C_n/ξ becomes smaller as n increases, $\delta(f)$ in the above expression may be negligibly small in most scenarios and ignoring this term leads to the following approximate PSD expression:

$$S_{z_o}(f) \approx |\rho_{z_i,z_o}|^2 S_{x_i}(f) + \left(1 - |\rho_{z_i,z_o}|^2\right) S_{x_i}^{\star(3)}(f). \tag{4.47}$$

4.4.4 Power Spectrum Expression for Band-Limited OFDM Signals

The calculation of the exact spectrum (4.19) or its approximate form (4.47) requires the knowledge of the input signal spectrum and its self-convolution. So far, we have not specified the form of the input signal spectrum and we will now focus on the band-limited OFDM signals. Let us define the lth complex baseband OFDM signal centered at the zero frequency that can be expressed as [OI02]

$$z_{i,l}(t) = \frac{1}{\sqrt{N}} \sum_{k=0}^{N-1} X_{l,k}\, e^{j2\pi(k-(N-1)/2)t/T}, \tag{4.48}$$

where N is the number of subcarriers, $X_{l,k}$ denotes a QAM (or PSK) symbol on the kth subcarrier of the lth OFDM symbol, and T is a symbol period.

Note that $z_{i,l}(t)$ defined in (4.48) is periodic with period T, and the resulting input signal formed by the consecutive OFDM symbols may be expressed as

$$z_i(t) = \sum_{l=-\infty}^{\infty} z_{i,l}(t) w(t - lT_s), \tag{4.49}$$

where $w(t)$ is a windowing function of length $T_s > T$ that controls the smoothness of the transition between the consecutive OFDM symbols. Strict characterization of the PSD requires the knowledge of $w(t)$ as it also causes the spectral leakage. In this chapter, however, we focus only on the out-of-band radiation caused by nonlinear distortion through examination of only one OFDM symbol for simplicity and the effect of the spectral leakage caused by this windowing will not be considered.

Provided that $\{X_{l,k}\}$ are independent and identically distributed (i.i.d.), as N increases the distribution of the OFDM signal is known to approach that of a complex Gaussian random process with near rectangular spectral shape. Therefore, in what follows, we assume that $z_i(t)$ is an ideally band-limited Gaussian random process whose PSD is expressed as

$$S_{z_i}(f) = S_{x_i}(f) = \begin{cases} 1, & |f| < \frac{1}{2}, \\ 0, & \text{otherwise.} \end{cases} \tag{4.50}$$

Then, its self-convolution can be expressed by [Dar; Mor87]

$$S_{x_i}^{\star(2n+1)}(f) = (2n+1)\sum_{p=0}^{n-l} \frac{(-1)^p (n+\frac{1}{2}-|f|-p)^{2n}}{p!(2n+1-p)!}, \tag{4.51}$$

for

$$\max\left(0, l-\frac{1}{2}\right) < |f| < l+\frac{1}{2}, \tag{4.52}$$

where $l = 0, 1, \cdots, n$. In particular, when $n = 1$ we obtain

$$S_{x_i}^{\star(3)}(f) = \begin{cases} \frac{3}{4} - |f|^2, & |f| < \frac{1}{2}, \\ \frac{1}{2}\left(\frac{3}{2} - |f|\right)^2, & \frac{1}{2} < |f| < \frac{3}{2}. \end{cases} \tag{4.53}$$

After some algebraic manipulation, we obtain the expression of the power that falls in-band as

$$\begin{aligned} \beta_{n,\text{in}} &= 2\int_0^{\frac{1}{2}} S_{x_i}^{\star(2n+1)}(f) df \\ &= 2\sum_{p=0}^{n} (-1)^p \frac{(n-p+\frac{1}{2})^{2n+1} - (n-p)^{2n+1}}{(2n-p+1)!p!}. \end{aligned} \tag{4.54}$$

It follows that the first four terms ($n = 1, 2, 3, 4$) can be calculated as

$$\{\beta_{1,\text{in}}, \beta_{2,\text{in}}, \beta_{3,\text{in}}, \beta_{4,\text{in}}\} = \left\{\frac{2}{3}, \frac{11}{20}, \frac{151}{315}, \frac{15619}{36288}\right\} = \{0.667, 0.55, 0.479, 0.439\} \tag{4.55}$$

and we observe that it decreases monotonically. Thus, the maximum in-band spectral component is $\beta_{*,\text{in}} = \frac{2}{3}$ in this case. Consequently, the following observation can be

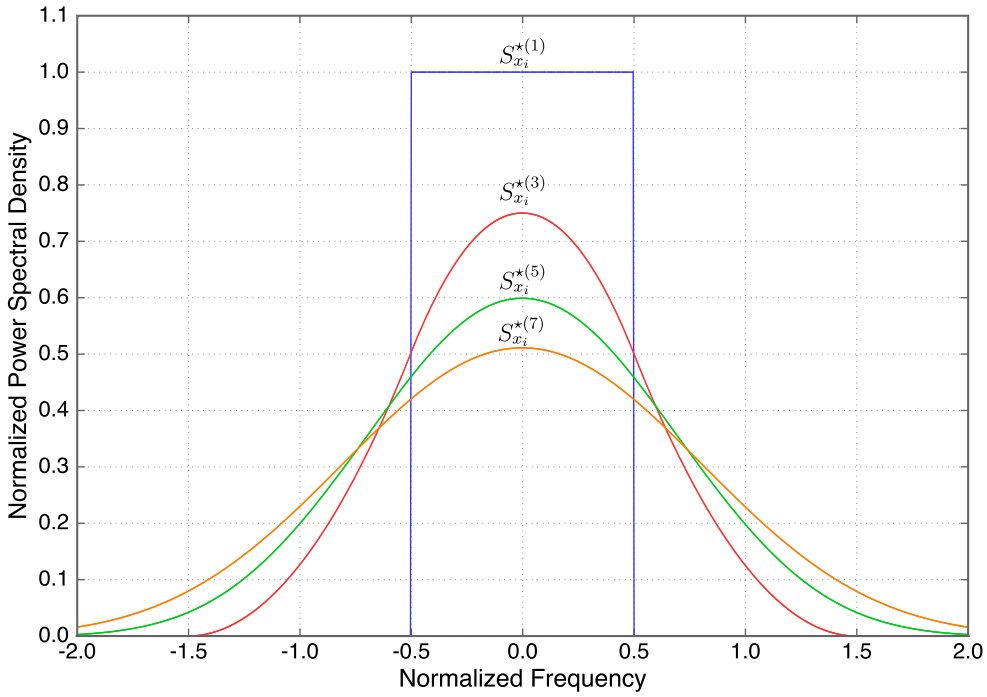

Figure 4.2: The self-convolution of the power spectral density $S_{x_i}^{\star(2n+1)}$ for $n = 0, 1, 2$, and 3.

made: From (4.44), the effective SDR and the total SDR are related by

$$\text{SDR}_{\text{eff}} \geq \frac{3}{2}\text{SDR}_{\text{total}}. \tag{4.56}$$

That is, the effective SDR is at least 1.76 dB higher than the total (or design) SDR in the case of OFDM signals with near rectangular spectrum, which agrees with the observation given in [Och13].

The PSDs of the several beginning orders of $S_{x_i}^{\star(2n+1)}$ in the case of the rectangular input spectrum are plotted in Fig. 4.2. It is observed that with increasing n, the in-band component steadily decreases and thus the sidelobe power increases accordingly.

4.5 Numerical and Experimental Results

In this section, through simulation and actual measurements, we verify the effectiveness of the proposed theoretical PSD expression derived in the previous section. The simulation and experimental procedures are illustrated in Fig. 4.3.

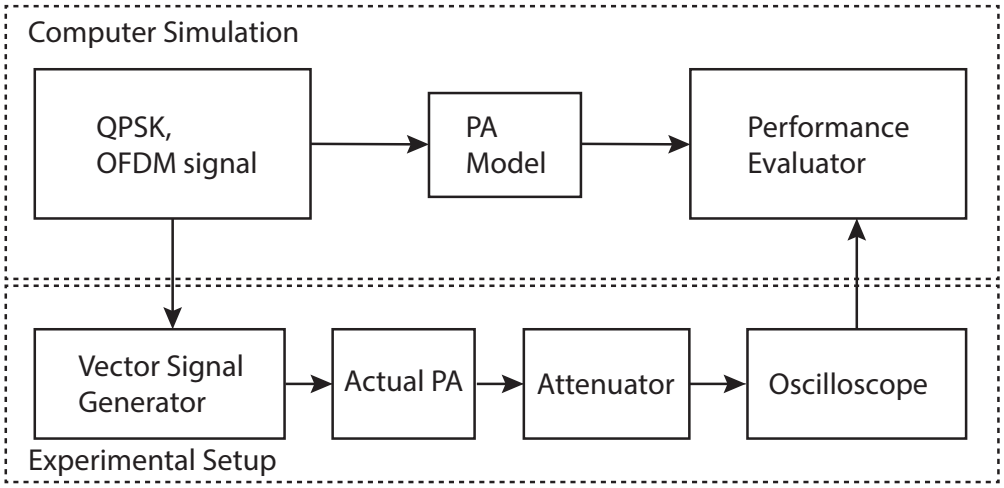

Figure 4.3: Simulation and experimental setup.

4.5.1 Calculation of PSD and EVM for Simulation and Measurement

In this work, we calculate the periodogram by taking an ensemble average of the square of discrete Fourier transform of the generated and power amplified complex baseband OFDM signals. Upon evaluating the periodogram through simulation and measurement, the N-subcarrier OFDM signal is sampled only for one OFDM symbol period with J times oversampling, i.e., with $J\,N$-point FFT. In this manner, the effect of the spectral leakage associated with OFDM symbol transition is eliminated from our PSD calculation and the results become consistent with our theoretical analysis.

For the EVM, we calculate the root mean square error between the detected symbol $\tilde{X}_{l,k}$ and the transmitted symbol $X_{l,k}$ scaled by an optimal attenuation factor, i.e., [Och13]

$$\text{EVM} = \sqrt{\frac{E\left\{\left|\tilde{X}_{l,k} - \alpha X_{l,k}\right|^2\right\}}{E\left\{|\alpha X_{l,k}|^2\right\}}} \times 100 \tag{4.57}$$

where

$$\alpha = \frac{E\left\{X_{l,k}^{*}\tilde{X}_{l,k}\right\}}{E\left\{|X_{l,k}|^2\right\}}. \tag{4.58}$$

This will be compared by the upper bound based on the total SDR, i.e., (4.45) with $\beta_{*,\text{in}} = \frac{2}{3}$.

4.5.2 Calculation of Cross-Correlation Coefficient for Measurement

The calculation of our proposed approximate PSD at least requires the knowledge of the cross-correlation coefficient (4.17). In the case of the measurement where the AM-AM and AM-PM curves of the PA are not known *a priori*, we perform its calculation as follows. Let r_n denote the nth input envelope level at which the corresponding AM-AM and AM-PM of the PA are measured, and let us choose them such that the interval of any closest two samples is equal, i.e., we choose $\{r_n\}$ such that for any n, $r_{n+1} - r_n = \Delta r$ where Δr is constant. Let $g(r_n)$ and $\phi(r_n)$ denote the corresponding measured amplitude and phase responses to r_n. From (4.17), one may express the estimate of the cross-correlation coefficient as

$$|\rho_{z_i,z_o}|^2 \approx \frac{\left\{\sum_n e^{-\frac{r_n^2}{A_0^2}\gamma_0^2} r_n^2 g(r_n)\cos\left[\phi(r_n)\right]\right\}^2 + \left\{\sum_n e^{-\frac{r_n^2}{A_0^2}\gamma_0^2} r_n^2 g(r_n)\sin\left[\phi(r_n)\right]\right\}^2}{\left\{\sum_n e^{-\frac{r_n^2}{A_0^2}\gamma_0^2} r_n^3\right\}\left\{\sum_n e^{-\frac{r_n^2}{A_0^2}\gamma_0^2} r_n g^2(r_n)\right\}} \tag{4.59}$$

where $\gamma_0 \triangleq A_0/\sqrt{P_{\text{in}}}$ corresponds to the IBO with the reference maximum envelope level denoted by A_0.

4.5.3 Simulation Setup

For the Monte-Carlo simulation, we generate 1 024 000 OFDM symbols with the number of subcarriers $N = 256$, where each subcarrier is modulated by QPSK except for the center subcarrier that is set to be null. Since arbitrary PA characteristics can be generated for simulation, in addition to the soft envelope limiter and erf models described in Section 4.3.1, we consider the well-adopted Rapp and Saleh models as our reference of more practical PA models. Their complex gains are plotted in Fig. 2.4. For both the cases, the coefficients C_n of (4.23) may not be expressed in a convenient analytical form, and thus they should be calculated numerically.

We use Rapp and Saleh models as power amplifier simulation which are introduced in Chapter 2. Note that there is no AM-PM effect in the Rapp model, that is, $\phi(r) = 0$. Throughout this work, $p = 3.0$ will be adopted as a relatively good AM-AM example.

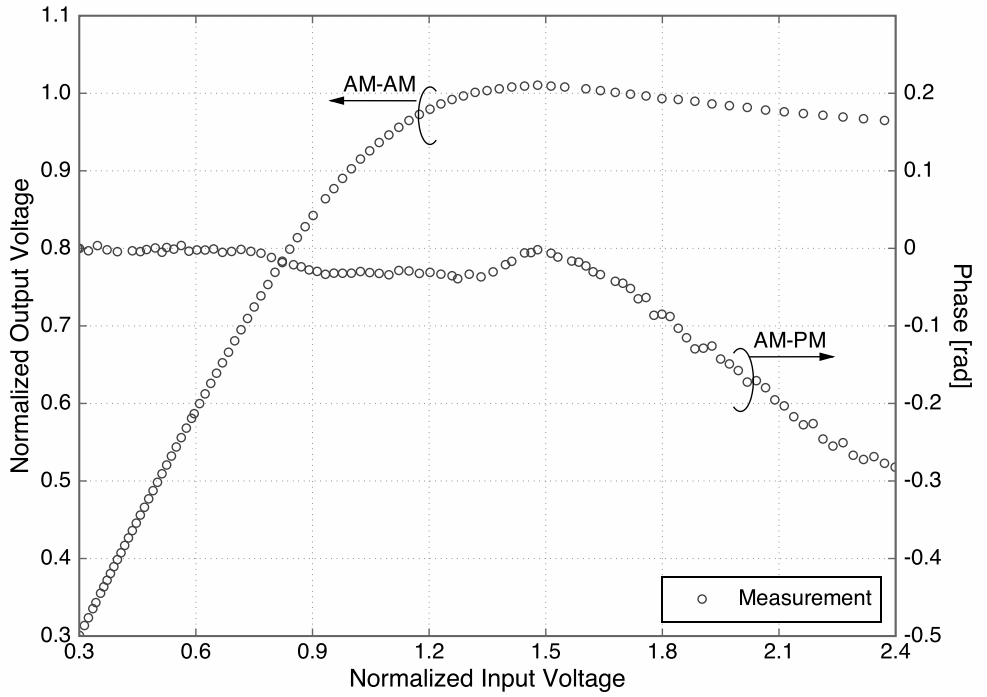

Figure 4.4: AM-AM and AM-PM characteristics of measured PA

4.5.4 Experimental Setup

In the case of the measurement using actual PA where the basic configuration of the experimental setup is illustrated in Fig. 4.3, the data used for generating the input OFDM signals is chosen to be the same as those used in the simulation process. The complex baseband OFDM signal is generated by a computer and then up-converted to the RF signal by the vector signal generator (VSG). The number of the OFDM symbols generated for this measurement is 576 000. The RF modulated signal by VSG is then power amplified by the actual PA, and then is fed, after attenuation of the signal power, to the oscilloscope where the nonlinearly amplified signal is captured and down-converted to the baseband OFDM signal. Finally, the captured data is analyzed by computer in terms of the resulting PSD and EVM.

The PA used in this measurement is the SSPA with gain of 29 dB at 2GHz, and operates with the input signal frequency ranging from 2MHz to 3GHz. Our measurement was performed at 800MHz. The bandwidth of the OFDM signal was set as 12.5MHz. The AM-AM and AM-PM characteristics have been measured by the single frequency input from VSG, and their characteristics are plotted in Fig. 4.4.

4.5.5 Numerical and Experimental Results

For all the theoretical results on PSD, we refer to the results as "exact" when it is calculated using (4.19) with the coefficients C_n given by (4.23), where the summation is taken up to $n = 10$ terms. On the other hand, the proposed simple approximate form (which will be referred to as "approximation" in the results) is based on (4.47) where the cross-correlation coefficient is calculated from (4.17). For the exact case, the required self-convolution of the spectrum is calculated using (4.51) whereas only (4.53) is used for the approximation.

Power Spectral Density

We start with the PSD results for the OFDM signal amplified by the soft envelope limiter shown in Fig. 4.5 (a). In all the cases of IBO examined, it is observed that the exact one and simulation well agree. Furthermore, the proposed simple approximation shows good agreement with the simulation results and this tendency becomes noticeable as the IBO decreases. The reason for this behavior can be verified from Fig. 4.1 (a) where the lower-order nonlinear distortion is dominant in lower IBO whereas higher-order terms eventually prevail as IBO increases. For example, we observe from Fig. 4.1 (a) that the amount of nonlinear distortion of $n = 2$ becomes greater than that of $n = 1$ when the IBO is higher than 6.5 dB.

Next, we examine the erf model and the results are shown in Fig. 4.5(b). In this case, we observe that all the three cases show almost perfect agreement. This is due to the fact that the third-order nonlinear distortion is dominant in all the IBO range of interest as observed from Fig. 4.1(b).

The results for the cases of Rapp (with $p = 3.0$) and Saleh models are shown in Fig. 4.6(a) and (b), respectively, where we observe the tendencies similar to the soft envelope limiter and erf models, respectively. This behavior can be also inferred from the similarity of the AM-AM characteristic curves shown in Fig. 2.4.

In the case of measurement, the approximate PSD is calculated based on the measured cross-correlation coefficient using (4.59). The corresponding theoretical PSD is compared with the measured PSD in Fig. 4.7. We observe that our approximation approach can capture the distortion accurately, especially when IBO is relatively small as expected.

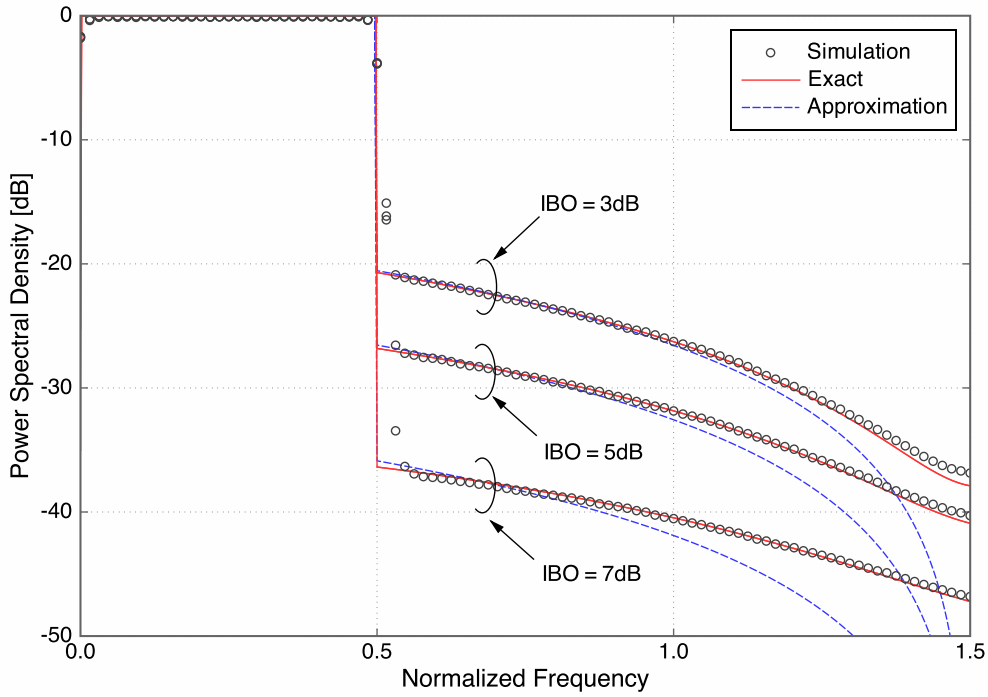

(a)

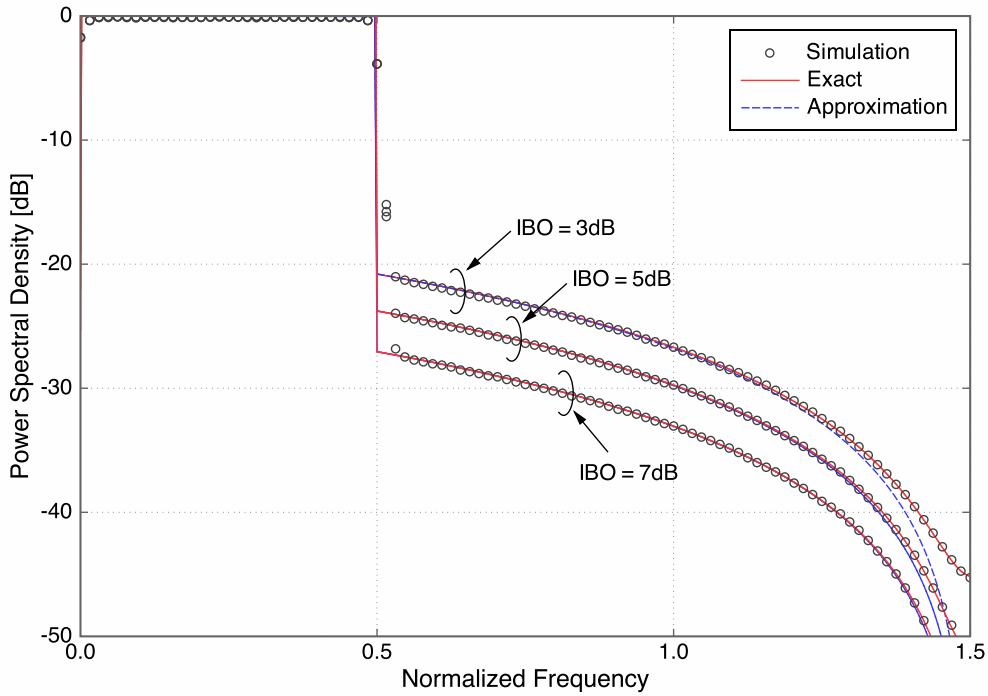

(b)

Figure 4.5: PSD comparison of theoretical and simulation results based on (a) soft envelope limiter model and (b) the erf model.

Error Vector Magnitude

The EVMs in the case of soft envelope limiter and erf models are calculated by the simulation and shown in Fig. 4.8, together with the corresponding theoretical upper

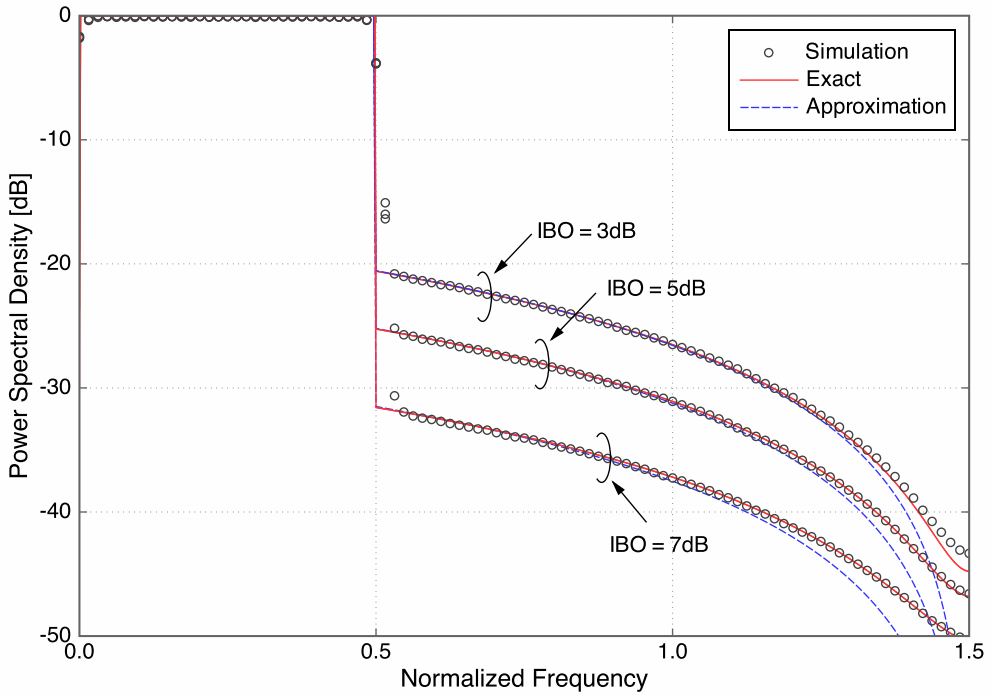

(a)

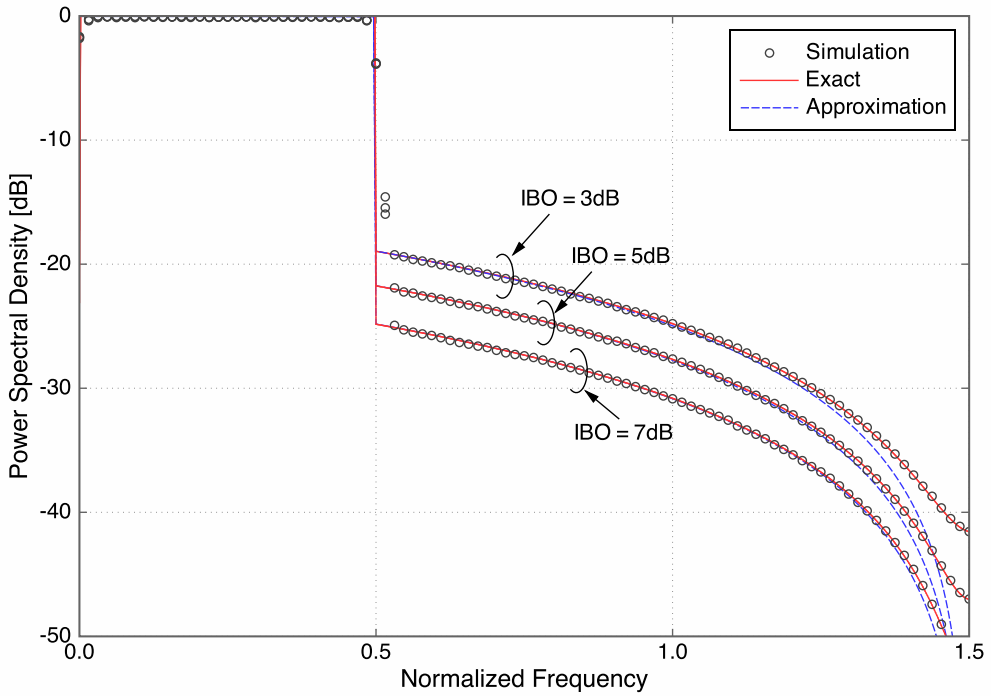

(b)

Figure 4.6: PSD comparison of theoretical and simulation results based on (a) Rapp model with $p = 3.0$ and (b) Saleh model.

bounds. We observe that both the simulation results and upper bounds well agree, which may justify the accuracy of our proposed analytical approach. It is interesting to observe that when the two curves are compared with the same IBO value, soft envelope

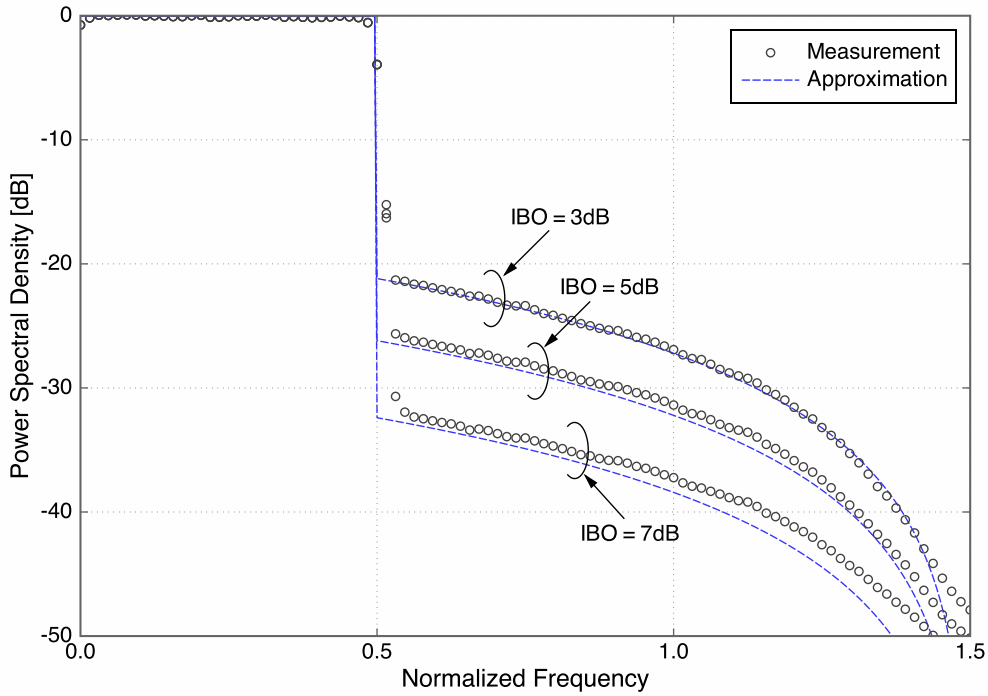

Figure 4.7: PSDs of real PA based on our proposed approximation method.

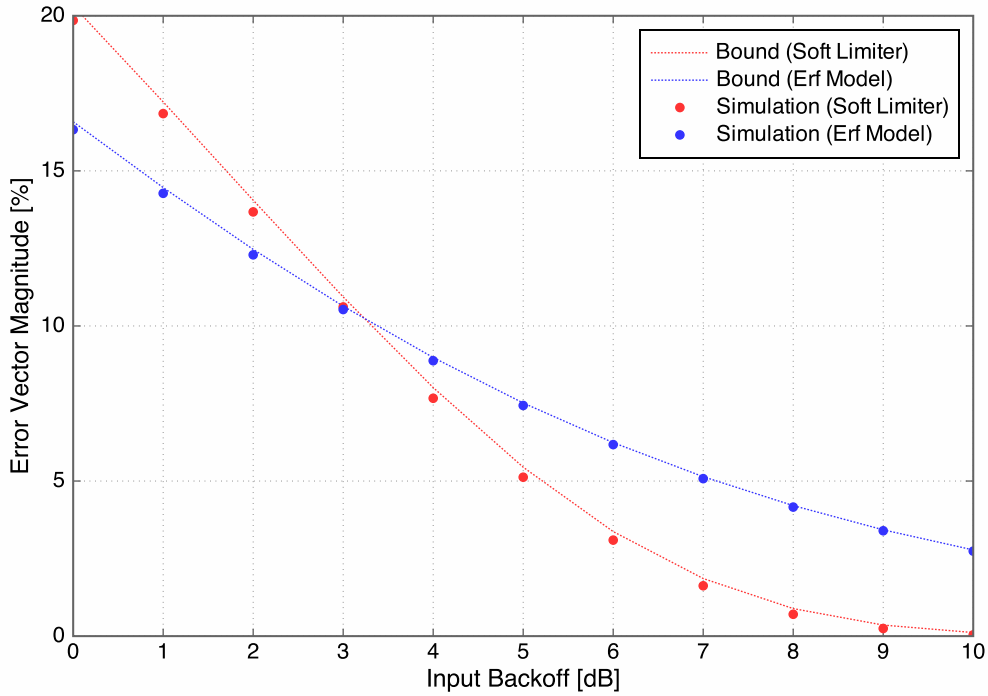

Figure 4.8: EVM results of soft envelope limiter and erf model.

limiter has higher EVM value when IBO is lower than 3 dB, even though it rapidly decreases as IBO increases compared to that of the erf model. We note that similar agreement behavior has been also observed for the Rapp and Saleh models.

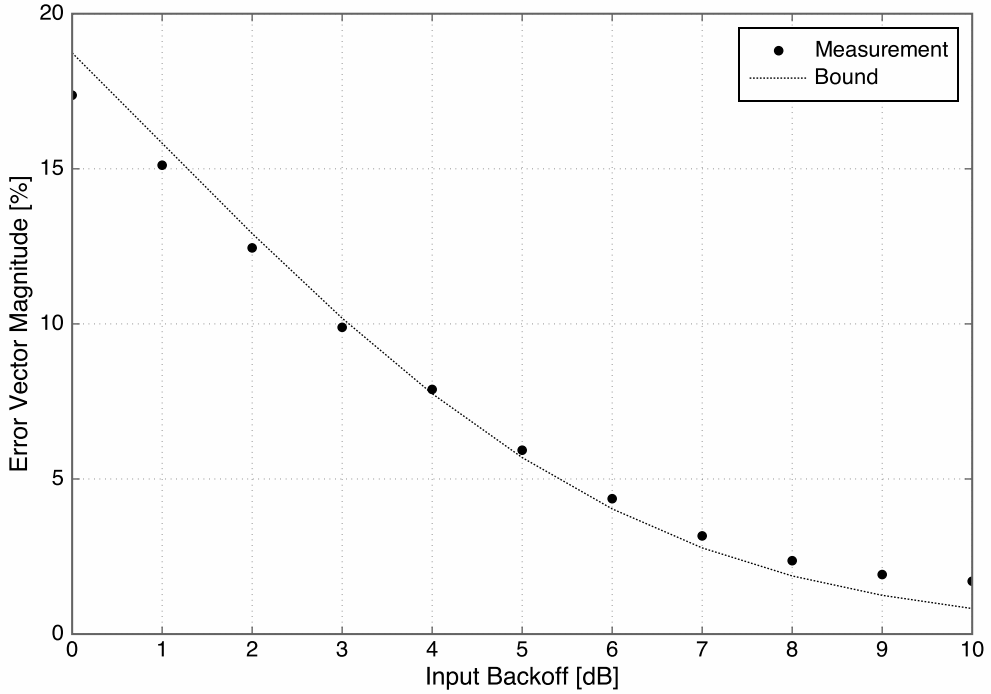

Figure 4.9: EVM results of actual PA.

Finally, in Fig. 4.9, the EVM calculated based on the measurement is compared with the corresponding upper bound based on the theoretical calculation using measured cross-correlation coefficient. For low IBO region, good agreement is observed between the measured results and our upper bound as expected. However, we observe some gap when the IBO is high where high SDR is expected. Several reasons can be considered for this behavior. First, since the number of subcarriers considered in this work is not large ($N = 256$), the assumption of an OFDM signal as a Gaussian process may not be accurate enough. Second, since the OFDM signals with high peak power occur less frequently than those with low peak power [OI01], the event that the OFDM signal is affected by nonlinear distortion becomes rare [Bah+02], especially in the high SDR region where the IBO is set high. Finally, the measured results are affected not only by the nonlinear distortion but also by the additive white Gaussian noise (AWGN) (due to the thermal noise) as well as the quantization noise, where the latter two factors are not taken into consideration in our theoretical calculation.

4.6 Conclusion

In this work, based on the exact mathematical model, we have first established the relationship between the cross-correlation coefficient of the input and output envelope

of the nonlinearly amplified Gaussian signals (or total SDR) and its power spectral density. Based on this result, we have proposed a simple approximate expression for the PSD and EVM of the nonlinearly amplified OFDM signals that can be derived using the cross-correlation coefficient calculated only from the AM-AM and AM-PM characteristics of a PA. Through computer simulation and actual measurement, the effectiveness and accuracy of our approach have been demonstrated. Even though this approach is theoretically valid only for the Gaussian signals with rectangular spectra, which can be approached by the OFDM with a large number of subcarriers, it is expected to offer an approximate solution for other linearly modulated signaling cases. Further investigation may be necessary to investigate the applicability of the proposed approach to other modulation formats.

Chapter 5

A Trellis Shaping Approach for Peak Power Reduction of SC-FDMA Signals

5.1 Introduction

The fourth generation (4G) wireless communication standard known as the Long Term Evolution - Advanced (LTE-A) has successfully improved the achievable transmission rate by incorporating the state-of-the-art techniques. Unlike the third generation (3G) system where the code-division multiple-access (CDMA) plays a primary role, the LTE-A significantly increases the spectral efficiency by adopting frequency-division multiple-access (FDMA)-based approach together with the transmit signals with higher dynamic range. The use of such signals, however, leads to higher energy consumption in power amplifier (PA) at the transmitter [HBB11; GZ14]. Considering the growing concerns toward green communications in the global level, the improvement of energy efficiency without sacrificing the spectral efficiency is an issue of the utmost importance for the next wireless communications standards including 5G [Wan+14; I+14; Boc+14].

In the LTE-A standard, a single-carrier frequency-division multiple-access (SC-FDMA) is adopted as its uplink radio access and orthogonal frequency-division multiple-access (OFDMA) as its downlink. One of the primary reasons that the SC-FDMA has found its practical application is that the resulting signal has lower peak-to-average power ratio (PAPR) than the orthogonal frequency-division multiplexing (OFDM) signal and yet has robustness against frequency selective fading channels similar to the conventional OFDM by the use of cyclic prefix and frequency-domain equalization (FDE) [Fal+02].

The signal bearing high PAPR causes nonlinear distortion unless PA has highly linear characteristics and its input back-off (IBO) is appropriately adjusted. If IBO is set insufficient, the resulting nonlinear distortion not only degrades the quality of transmit signal but also introduces interference to adjacent channels, thus decreasing the spectral efficiency of the overall system. On the other hand, increasing IBO reduces the power conversion efficiency of PA, leading to lower effective average power of transmit (and thus received) signals as well as an increase of heat dissipation. Therefore, the signal quality (i.e., distortion) and its PA efficiency has essentially a trade-off relationship. For the uplink of the cellular networks, the reduction of PAPR signal translates to the improvement of the PA efficiency, thus enhancing its coverage since it increases the transmit signal power for a given energy consumption of battery. Thus, even though the SC-FDMA adopted in the LTE-A standard has higher complexity than that of OFDMA due to the additional process known as a *discrete Fourier transform (DFT) precoding*, it has turned out to be preferable to the latter.

Nevertheless, even with constant amplitude modulation such as phase shift keying (PSK), the dynamic range of the SC-FDMA signal is not constant due to the existence of the pulse shaping filtering. In fact, the use of DFT precoding together with higher-order modulation considerably increases its signal dynamic range [MLG06; Ber+08; HNA07; CSL11; Ben+10; Och12], and thus reduces the PA efficiency. Therefore, reduction of PAPR even for SC-FDMA should lead to further improvement of energy efficiency over OFDMA.

To date, only a few peak power reduction techniques have so far been proposed for SC-FDMA in the literature [CSL11; Fal11]. Since the SC-FDMA system has a transmitter structure similar to conventional single-carrier systems, some peak power reduction techniques developed for the latter may be applicable to SC-FDMA as well, provided that suitable modifications are applied. Several peak power reduction techniques have been proposed for the conventional pulse-shaped single-carrier systems. For example, in [CC05], considering the pulse-shaping process as a memory device (or a convolutional encoder), a peak power reduction technique based on the trellis structure has been proposed. On the other hand, it has been demonstrated in [TO09a] that the trellis shaping (TS) scheme that has been developed for average power reduction of high-order QAM [For92] can generate near constant envelope PSK signals even with a near rectangular pulse-shaping filter. This approach has been later extended to single-carrier high-order QAM systems in [TO09b].

There are two major issues when TS is applied to SC-FDMA systems. First, the impulse response of the pulse shaping filter used for SC-FDMA is essentially a *periodic sinc* function [Och12; Ben+10] whose energy decays very slowly. Therefore, the impulse response is non-negligible over entire SC-FDMA block. Second, due to the periodic nature of this pulse shaping filter, the signal is generated by circular convolution of the filter with input QAM symbols. Therefore, the filtered signal waveform corresponding to the head of each SC-FDMA block is also affected by the QAM symbols located in its tail and *vice versa*.

In this work, we first identify the major challenges associated with PAPR reduction based on TS for SC-FDMA systems. We then propose a novel TS-based approach that enables an efficient PAPR reduction of QAM-modulated SC-FDMA systems.

The rest of this chapter is organized as follows. In Section 5.2, we briefly describe the SC-FDMA system as well as trellis shaping considered throughout this work. The major issues that should be taken into account when TS is applied to SC-FDMA systems are also identified. Our novel approach for TS-based PAPR reduction of SC-FDMA signals is proposed in Section 5.4. Improvement of PA efficiency and the resulting effect of nonlinear distortion are evaluated through the computer simulations in Section 5.6. Finally, conclusions are given in Section 5.7.

5.2 System Description

Figure 5.1 describes a block diagram of the entire system model considered throughout this paper. The information is first encoded by the trellis shaping (TS) encoder that maps a binary sequence to QAM (or PSK) constellation, followed by SC-FDMA signal generator. The resulting signal is then subject to nonlinear amplification of power amplifier. The signal is then transmitted over a frequency selective fading channel with additive white Gaussian noise (AWGN). The received SC-FDMA signal is then detected based on the MMSE criterion. Finally, the information is retrieved through the decoder corresponding to TS encoder.

5.2.1 SC-FDMA

We consider the SC-FDMA system where the maximum of Q users are allocated to a single SC-FDMA block with each user having M-QAM (or PSK) symbols to transmit

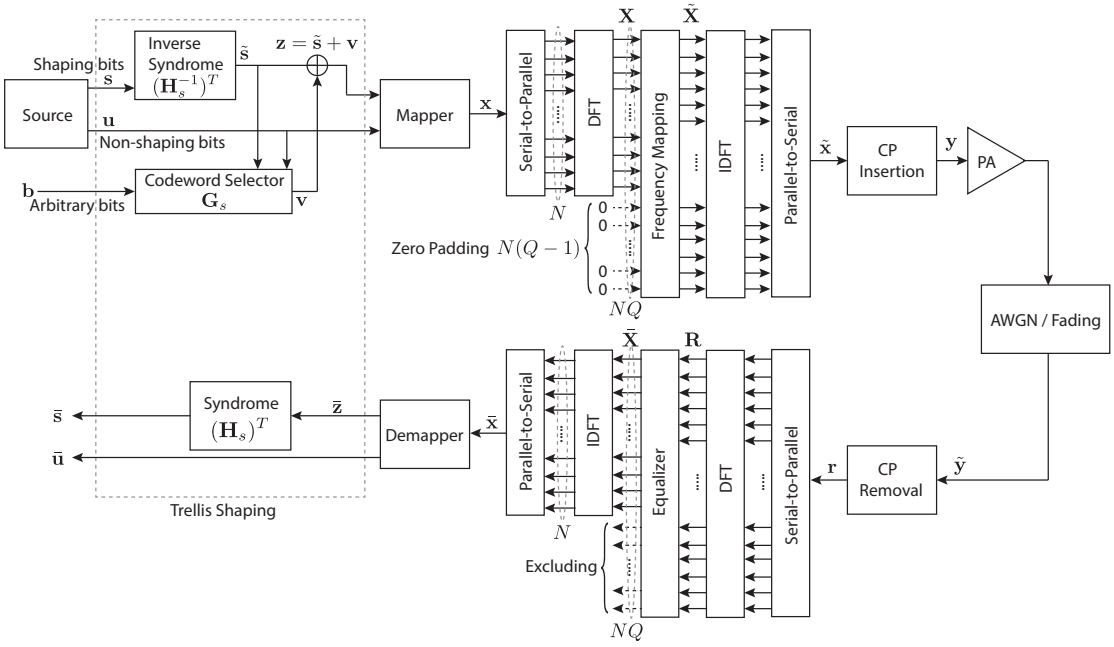

Figure 5.1: A block diagram of the transmitter for the SC-FDMA system with trellis shaping.

within the same block. In general, the SC-FDMA signal is generated by two cascaded discrete Fourier transform (DFT). Let $q \in \{0, 1, \cdots, Q-1\}$ denote the index of the users and $x_n^{(q)} \in \mathcal{X}$ denote the nth symbol of the qth user, where $n \in \{0, 1, \cdots, N-1\}$ and $\mathcal{X}$ is a set of the signal constellations (such as PSK and QAM). The N-point DFT converts a set of the time-domain symbols $\{x_n^{(q)}\}$ to its frequency-domain representation as

$$X_m^{(q)} = \frac{1}{\sqrt{N}} \sum_{n=0}^{N-1} x_n^{(q)} e^{-j2\pi \frac{mn}{N}}, \quad \text{for} \quad m = 0, 1, \cdots, N-1. \tag{5.1}$$

The above N complex-valued samples are then mapped onto the frequency-domain slots of size $Q \times N$. Several FDMAs are proposed depending on how these samples are mapped onto the frequency-domain slots (often called *subcarriers*), and in this work we only focus on the localized FDMA (LFDMA) adopted in LTE-A. Without loss of generality, the frequency-domain mapping of LFDMA for the qth user can be expressed as

$$\tilde{X}_k = \begin{cases} X_m^{(q)}, & \text{if } \; k = qN + m, \; m \in \{0, 1, \cdots, N-1\}, \\ 0, & \text{elsewhere}, \end{cases} \tag{5.2}$$

for $k = 0, 1, \cdots, QN-1$. The subsequent QN-point IDFT converts the frequency-domain components back to the time-domain signal samples as

$$\tilde{x}_l^{(q)} = \frac{1}{\sqrt{N}} \sum_{k=0}^{QN-1} \tilde{X}_k e^{j2\pi \frac{lk}{QN}} = \frac{1}{\sqrt{N}} e^{j2\pi \frac{q}{Q} l} \sum_{m=0}^{N-1} X_m^{(q)} e^{j2\pi \frac{m}{QN} l}, \quad \text{for} \quad l = 0, 1, \cdots, QN-1. \tag{5.3}$$

By substituting (5.1) into (5.3), the discrete samples of the SC-FDMA signal can be expressed for $l \in [0, QN-1]$ as [MLG06; Och12]

$$\tilde{x}_l^{(q)} = \sum_{n=0}^{N-1} x_n \, g_{l-nQ}^{(q)}, \tag{5.4}$$

where $g_m^{(q)}$ is a *periodic sinc function* expressed for any integer $m \in [-Q(N-1), QN-1]$ as

$$g_m^{(q)} = e^{j\pi\left(2q+1-\frac{1}{N}\right)\frac{m}{Q}} \frac{\sin\left(\frac{\pi m}{Q}\right)}{N \sin\left(\frac{\pi m}{NQ}\right)}. \tag{5.5}$$

Therefore, the resulting signal is in fact the oversampled (i.e., interpolated) version of the original sample sequence $\{x_{l,k}\}$ by Q times with filtering based on the periodic sinc function. Setting Q large enough, the discrete samples of (5.4) can be considered as a good approximation of band-limited continuous baseband SC-FDMA signals.

When cyclic prefix (CP) corresponding to P symbols are added, then we may express the output samples as

$$y_l^{(q)} = \begin{cases} \tilde{x}_{QN+l}^{(q)}, & l = -QP, -QP+1, \cdots, -1, \\ \tilde{x}_l^{(q)}, & l = 0, 1, \cdots, QN-1, \end{cases} \tag{5.6}$$

for an integer $l \in [-QP, QN-1]$.

5.2.2 Detection of SC-FDMA Symbols

At the receiver side, the received signal after CP removal can be expressed by

$$r_m^{(q)} = \sum_{l=0}^{QN-1} h_l^{(q)} \tilde{x}_{m-l}^{(q)} + w_m, \tag{5.7}$$

where h_l and w denote channel impulse response and additive white Gaussian noise (AWGN). The received signal is fed to QN-point DFT, and then, its output can be expressed by

$$R_m^{(q)} = \Upsilon_m^{(q)} \tilde{X}_m^{(q)} + W_m. \tag{5.8}$$

By applying MMSE equalizer into (5.8), frequency components are compensated such as

$$\bar{X}_m^{(q)} = T_m^{(q)} \left(\Upsilon_m^{(q)} \tilde{X}_m^{(q)} + \tilde{W}_m \right), \tag{5.9}$$

where

$$T_m^{(q)} = \frac{\left(\Upsilon_m^{(q)}\right)^*}{\left|\Upsilon_m^{(q)}\right|^2 + \text{SNR}}. \tag{5.10}$$

Consequently, the signal constellation from IDFT output can be expressed by substituting (5.1) and (5.3) into (5.9) as [RC09]

$$\begin{aligned} \bar{x}_m^{(q)} &= \frac{\sqrt{N}}{\sqrt{QN}} \sum_{n=0}^{QN-1} T_n^{(q)} \Upsilon_n^{(q)} \left(\tilde{X}_n^{(q)} + \tilde{W}_n \right) e^{-j2\pi \frac{nm}{QN}} \\ &= \frac{1}{\sqrt{QN}} \sum_{n=0}^{QN-1} T_n^{(q)} \Upsilon_n^{(q)} \left(\sum_{l=0}^{QN-1} \left(x_l^{(q)} + \tilde{w}_l \right) e^{j2\pi \frac{lm}{QN}} \right) e^{-j2\pi \frac{nm}{QN}} \\ &= \frac{1}{\sqrt{QN}} \sum_{n=0}^{QN-1} T_n^{(q)} \Upsilon_n^{(q)} \sum_{l=0}^{QN-1} \left(x_l^{(q)} + \tilde{w}_l \right) e^{j2\pi m \frac{(l-n)}{QN}}. \end{aligned} \tag{5.11}$$

We see that each symbol $x_l^{(q)}$ is interfered by another symbols when $l \neq n$. Now, expression (5.11) can be divided into desired signal, interference term and AWGN as

$$\bar{x}_m^{(q)} = \frac{1}{\sqrt{QN}} \sum_{n=0}^{QN-1} T_n^{(q)} \Upsilon_n^{(q)} \left\{ x_n^{(q)} + \sum_{\substack{l=0 \\ l \neq n}}^{QN-1} x_l^{(q)} e^{j2\pi m \frac{(l-n)}{QN}} + \sum_{k=0}^{QN-1} \tilde{w}_k e^{j2\pi m \frac{(k-n)}{QN}} \right\}. \tag{5.12}$$

5.3 Trellis Shaping for SC-FDMA

We consider application of trellis shaping (TS) [For92] to peak power reduction of SC-FDMA signals defined in the previous section. TS has been applied to band-limited

single-carrier PSK and QAM signals in [TO09a] and [TO09b], respectively, and in what follows we briefly summarize the notations introduced in [TO09a] and address the problem associated with direct application of TS to SC-FDMA signals.

5.3.1 Principle of TS

TS first multiplexes a codeword of a given shaping binary convolutional code at the transmitter that results in reduction of peak power in band-limited signals. To this end, the transmitter has to estimate the signal waveform for a given candidate codeword and should select the one that will minimize the peak power (or reduce the signal fluctuation). Specifically, let $\mathbf{G}_s$ denote the generator matrix of the shaping binary convolutional encoder with the number of memory elements ν, and let us assume that the rate of this code is $1/n_s$, i.e., $\mathbf{G}_s$ is given by $1 \times n_s$ matrix. The corresponding parity-check matrix $\mathbf{H}_s^T$ is given by $n_s \times (n_s - 1)$ matrix which satisfies $\mathbf{G}_s\mathbf{H}_s^T = \mathbf{O}$, where $(\cdot)^T$ denotes a transpose of matrix and $\mathbf{O}$ is a zero matrix of the corresponding size. The left inverse matrix of $\mathbf{H}_s^T$, denoted by $(\mathbf{H}_s^{-1})^T$, should satisfy $(\mathbf{H}_s^{-1})^T\mathbf{H}_s^T = \mathbf{I}$, where $\mathbf{I}$ is an identity matrix of the corresponding size, and thus the size of $(\mathbf{H}_s^{-1})^T$ is $(n_s-1)\times n_s$. In other words, $(\mathbf{H}_s^{-1})^T$ itself can be seen as a binary convolutional code of rate $(n_s - 1)/n_s$. Given a set of these matrices, the operation of TS for an N-subcarrier SC-FDMA system is described as follows. The information bit sequence from the source is first divided into the two sequences, each consisting of N symbols. They are defined as $\mathbf{s} = [\mathbf{s}_0, \mathbf{s}_1, \ldots, \mathbf{s}_{N-1}]$ with $\mathbf{s}_n \in \{0,1\}^{n_s-1}$ and $\mathbf{u} = [\mathbf{u}_0, \mathbf{u}_1, \ldots, \mathbf{u}_{N-1}]$ with $\mathbf{u}_n \in \{0,1\}^{n_u}$, where the former sequence is called a shaping sequence and the latter is called a non-shaping sequence in what follows. The integer n_u represents the number of the non-shaping bits carried by each symbol $\mathbf{u}_n$. The shaping sequence $\mathbf{s}$ is input to the rate-$(n_s - 1)/n_s$ convolutional code $(\mathbf{H}_s^{-1})^T$ to generate the sequence $\tilde{\mathbf{s}} = [\tilde{\mathbf{s}}_0, \tilde{\mathbf{s}}_1, \ldots, \tilde{\mathbf{s}}_{N-1}]$ with $\tilde{\mathbf{s}}_n = \mathbf{s}_n(\mathbf{H}_s^{-1})^T \in \{0,1\}^{n_s}$, which thus imposes one-bit redundancy per each symbol. The output sequence $\tilde{\mathbf{s}}$ can be added by an arbitrary valid codeword of the convolutional code $\mathbf{G}_s$ which we denote by $\mathbf{v} = [\mathbf{v}_0, , \mathbf{v}_1, \ldots, \mathbf{v}_{N-1}]$, since at the receiver the sum of the two binary sequences $\mathbf{z}_n = \tilde{\mathbf{s}}_n + \mathbf{v}_n$ should satisfy $\mathbf{z_n}\mathbf{H}_s^T = \mathbf{s}_n$ and thus the ambiguity introduced by $\mathbf{v}_n$ can be completely eliminated provided that $\mathbf{z} = [\mathbf{z}_0, \mathbf{z}_1, \ldots, \mathbf{z}_{N-1}]$ is correctly detected. There are several mapping approaches for the assignment of $\mathbf{z}_n$ and $\mathbf{u}_n$ to x_n (i.e., the nth QAM symbol), and we adopt that similar to the sign-bit shaping [For92], where $\mathbf{z}_n$ and $\mathbf{u}_n$ choose the most significant bits (MSBs) and the least significant bits (LSBs) of an M-ary QAM symbol, respectively. It follows that the size of the constellation should be $M = 2^{n_s+n_u}$.

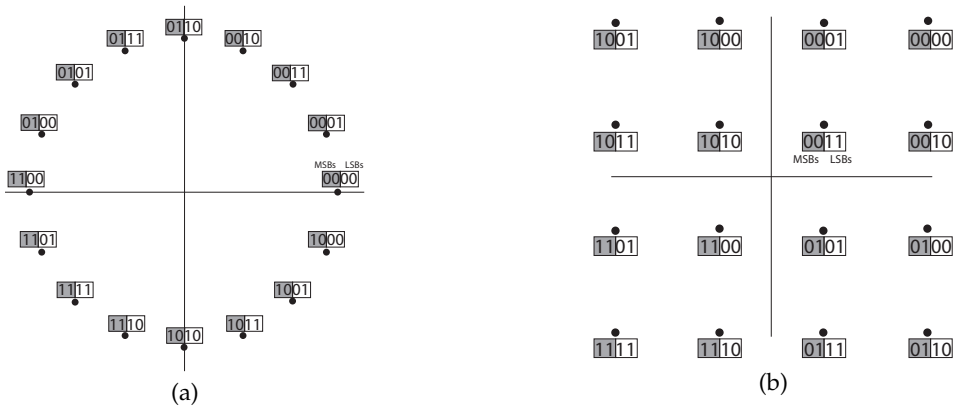

Figure 5.2: Bit labeling for (a) 16-PSK and (b) 16-QAM considered in this work.

In this work, 16-PSK and 16-QAM are considered as two representative cases of PSK and QAM, and their corresponding bit labeling is illustrated in Fig. 5.2. Both of them are arranged such that 1) for given LSBs, each element of each complement MSB pair (i.e., $\{00, 11\}$ and $\{01, 10\}$) is able to select one from the two constellation points with maximum Euclidean distance, and 2) within a set of the four points with the same MSBs, the LSBs follow Gray labeling. The first property guarantees a good peak power control capability by the convolutional codes with maximum free distance, whereas the second property contributes to minimization of the bit error rate. Note that the 16-QAM mapping in Fig. 5.2(b) is called *Type-II mapping* in [Och04] and is able to reduce *both peak and average power* if the associated metric is properly designed.

5.3.2 Metric for Viterbi Decoder

Our task in TS is to find a suitable codeword $\mathbf{v}$ that leads to a transmit signal with smaller peak (or average) power. Since this is equivalent to decoding of binary convolutional code, the Viterbi algorithm (VA) can be employed. A suitable metric that captures signal dynamic range should be developed for Viterbi decoding. In other words, the VA should incorporate a metric that accounts for the instantaneous peak power instead of the Euclidean distance in the conventional channel decoding.

Partial Signal Representation

In the case of SC-FDMA, the signal is generated by the impulse response defined by (5.5) and this spans over the entire SC-FDMA symbol period of $[0, QN)$, or equivalently, $[-\frac{QN}{2}, \frac{QN}{2})$ due to the periodic nature of the impulse response. We now consider the

impulse response in the form of

$$\tilde{g}_m^{(q)} = w_m(K_s)\, g_m^{(q)} \tag{5.13}$$

where $w_m(k)$ is a rectangular window function with a span corresponding to k symbols, defined as

$$w_m(k) = \begin{cases} 1, & -\frac{Qk}{2} \le m \le \frac{Qk}{2}, \\ 0, & \text{otherwise.} \end{cases} \tag{5.14}$$

In other words, we consider the truncated impulse response of the length corresponding to K_s symbols for generation of signal replicas used for metric calculation. The replica corresponding to (5.4) generated by the filter (5.13) for a given candidate transmit symbol sequence $\tilde{\mathbf{x}} = [\tilde{x}_0, \tilde{x}_1, \cdots, \tilde{x}_{N-1}]$, which we refer to as a *partial signal*, can be expressed as

$$\hat{x}_l^{(q)} = \sum_{n=0}^{N-1} \tilde{x}_n\, \tilde{g}_{l-nQ}^{(q)} = \sum_{n=0}^{N-1} \tilde{x}_n\, w_{l-nQ}(K_s)\, g_{l-nQ}^{(q)}. \tag{5.15}$$

Due to the constraint of (5.13), the partial signal for the time interval $kQ \le l < (k+1)Q$ is completely described by a linear combination of $\{\tilde{x}_n\}$ with the indices $n \in \{k - \left(\frac{K_s}{2} - 1\right), k - \left(\frac{K_s}{2} - 2\right), \cdots, k + \frac{K_s}{2}\}$, assuming that K_s is an even integer. Considering the causality of the system and introducing the time shift, the partial signal for $\left(k - \frac{K_s}{2}\right) Q \le l < \left(k - \frac{K_s}{2} + 1\right) Q$ is determined by $\{\tilde{x}_{k-(K_s-1)}, \tilde{x}_{k-(K_s-2)}, \cdots, \tilde{x}_k\}$, leading to the following waveform expression:

$$\hat{x}_l^{(q)} = \sum_{n=0}^{K_s-1} \tilde{x}_{k-n}\, g_{l-(k-n)Q}^{(q)}. \tag{5.16}$$

Defining $l' = l - \left(k - \frac{K_s}{2}\right) Q$, where $0 \le l' < Q$, we may express (5.16) for the time interval $kQ \le l < (k+1)Q$ as

$$\hat{x}_k^{(q)}(l') = \sum_{n=0}^{K_s-1} \tilde{x}_{k+\frac{K_s}{2}-n}\, g_{l'-\left(\frac{K_s}{2}-n\right)Q}^{(q)} \qquad \text{for} \quad k = 0, 1, \cdots, N - \frac{K_s}{2} - 1. \tag{5.17}$$

Note that $\tilde{x}_n$ with the negative indices, i.e., $\left\{\tilde{x}_{-1}, \tilde{x}_{-2}, \cdots, \tilde{x}_{-\left(\frac{K_s}{2}-1\right)}\right\}$, should be appropriately defined in the above expression. Furthermore, the last time-domain samples corresponding to $\left(N - \frac{K_s}{2}\right) Q \le l < NQ$ cannot be controlled by $\tilde{\mathbf{x}}$ of length N in

the above process.

Memory Extension

We incorporate the past $K_s - 1$ candidate symbols into each trellis section defined by the convolutional code. In the framework of TS, this can be achieved by introducing multiple external memories as described in [TO09a]. Specifically, if $\mathbf{v}_k$ is the kth output of the convolutional encoder defined by, e.g., $\mathbf{G}_s = [1+D^3, 1+D^2+D^3]$, the past output $\mathbf{v}_{k-m}$ is generated by $D^m\mathbf{G}_s = [D^m + D^{3+m}, D^m + D^{2+m} + D^{3+m}]$ where $1 \leq m < K_s$. In general, for the convolutional code with the number of memory elements ν, the number of states with extended memories is given by $2^{\nu+m}$. By choosing $m = K_s - 1$, the decoder can take into account the past $K_s - 1$ output symbols upon evaluating the kth output symbol.

Branch Metric Descriptions

For our branch metric calculation, we consider the moment method [TO09a] defined as

$$\mu_k = \sum_{l'=0}^{Q-1} \left| p_k(l') - p_{\text{ref}} \right|^{\beta} \tag{5.18}$$

where $p_k(l') = \left| \hat{x}_k^{(q)}(l') \right|^2$, β is a positive real value, and p_{ref} is a reference threshold power. Alternatively, one may focus only on the middle point of the Nyquist interval and metric increases only if the signal exceeds the threshold, which leads to

$$\mu_k^{+} = \left| p_k\left(\frac{Q}{2}\right) - p_{\text{ref}} \right|^{\beta}. \tag{5.19}$$

In both the above equations, the optimal threshold p_{ref} depends on the parameters such as modulations and target instantaneous power, and should be determined empirically by simulation in practice due to the difficulty of theoretical analysis.

In the case of M-QAM, the following metric is proposed in [TO09b] targeting the reduction of both peak-to-average power ratio and average power:

$$\mu_k^{\times} = \begin{cases} C_{\infty}, & p_k\left(\frac{Q}{2}\right) > p_{\text{peak}}, \\ |p_k\left(\frac{Q}{2}\right) - p_{\text{ref}}|, & \text{otherwise}, \end{cases} \tag{5.20}$$

where C_∞ is a constant set large enough compared to $|p - p_{\text{ref}}|$, and thus p_{peak} is the maximum peak value that the SC-FDMA signal will take.

5.3.3 Conventional TS Algorithm

The conventional TS can be described as follows. Define the trellis diagram according to $\mathbf{G}_s$ and its memory extension such that it has $2^{\nu+K_s-1}$ states. Assume that we have $\mathbf{u} = [\mathbf{u}_0, \mathbf{u}_1, \cdots, \mathbf{u}_{N-1}]$ and $\tilde{\mathbf{s}} = [\tilde{\mathbf{s}}_0, \tilde{\mathbf{s}}_1, \cdots, \tilde{\mathbf{s}}_{N-1}]$ from the source. Each branch of the trellis is thus associated with $\mathbf{z}_n = \tilde{\mathbf{s}}_n + \mathbf{v}_n$ which should be mapped onto the candidate QAM symbol $\tilde{x}_n$.

1. **Initialization:** We set $\tilde{x}_n = 0$, where $-K_s + 1 \leq n \leq -1$, and append it to $\tilde{\mathbf{x}}$ that is to be determined by this algorithm. We also append $K_s - 1$ zeros at the end of the sequence. The resulting sequence is

$$\tilde{\mathbf{x}}' = [\underbrace{0, 0, \cdots, 0}_{K_s-1} \tilde{x}_0, \tilde{x}_1, \cdots, \tilde{x}_{N-1}, \underbrace{0, 0, \cdots, 0}_{\frac{K_s}{2}}]. \tag{5.21}$$

2. Do the following for $k = 0, 1, \cdots, N-1$:

   (a) **Partial signal generation:** For each trellis section with the candidate MSBs specified by $\mathbf{z}_k$, generate $\tilde{x}_k$ and calculate $\hat{x}_k^{(q)}(l')$ according to (5.17).

   (b) **Branch metric calculation:** Calculate the corresponding branch metric μ_k.

   (c) **Viterbi decoding:** Perform the ACS (add-compare-select) operation of the Viterbi Algorithm to determine the survivor branch for each trellis section.

3. **Trace back:** When $k = N - 1$, trace back the path with the minimum metric to determine the sequence $\mathbf{x}$.

5.3.4 Major Issue in Application of TS to SC-FDMA

We demonstrate the major problem of the above approach based on the conventional TS for SC-FDMA by simulation. The parameters used in this simulation are listed in Table 5.1, and the resulting sample signal instantaneous power is plotted in Fig. 5.3. It is observed that high peak power is observed at both the edges of the SC-FDMA block. This stems from the fact that the partial signal in the range of $kQ \leq l < (k+1)Q$ is determined by $x_{k+\frac{K_s}{2}}$ as well as its past $K_s - 1$ symbols, and some of them are

Table 5.1: Simulation Specification

Modulation Type	16-QAM and PSK (Gray mapping)
DFT / IDFT size	N=64, Q=8
Symbol Length	Data (N) = 64, CP = 16
Partial Wave Symbol Length	$K_s = 8$
Metric Calculation Method	(5.19) for PSK with $\beta = 2$, (5.20) for QAM
Generator Polynomial (G_s)	$[1 + D^3\ 1 + D^2 + D^3]$
Syndrome Former (H_s^T)	$[1 + D^2 + D^3\ 1 + D^3]$
Inverse Syndrome Former (H_s^{-1})	$[D\ 1 + D]$

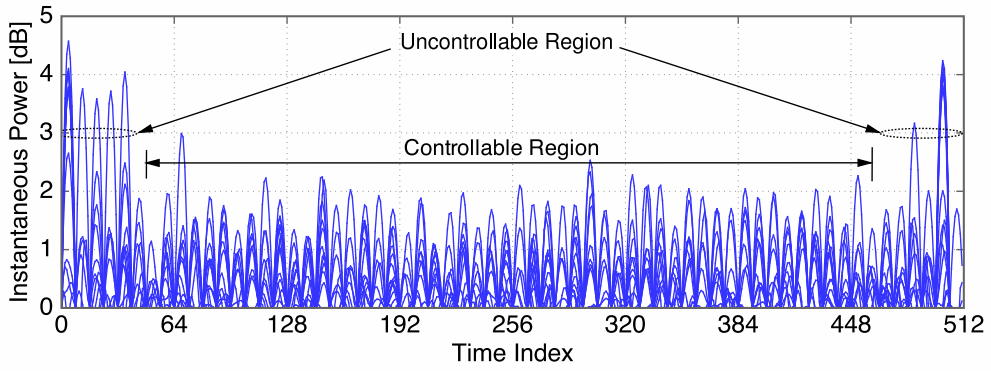

Figure 5.3: Edge peak power over entire 16-PSK SC-FDMA time-domain signal.

not determined *a priori* in these regions of the SC-FDMA signals, due to their periodic nature. Consequently, the region at the head of $\frac{K_s}{2}$ symbols as well the last $\frac{K_s}{2}$ symbols are uncontrollable in our framework as illustrated in Fig. 5.3.

In Fig. 5.4, the CCDF of the instantaneous power for the SC-FDMA signals are compared, where the CCDF of TS is divided into the two parts, *controllable region* and *uncontrollable region* as discussed above, and they are separately evaluated. As a reference, the single-carrier systems pulse shaped by the square-root raised cosine filter with a roll-off factor of $\alpha = 0.0$ (i.e., sinc(t) = $\sin(t)/t$) with the conventional TS are also compared where the symbol is truncated by $w_m(K_s)$ with $K_s = 8$ for partial signal generation of TS and $w_m(K)$ with $K = 8$ for actual signal generation to evaluate CCDF. From this figure, it is apparent that while the CCDF of the controllable region is similar to that of the conventional single carrier systems, that of the uncontrollable region exhibits considerable increase of instantaneous power, thus resulting in the total CCDF that is considerably worse than that of the conventional single-carrier systems. In the next section, we propose a novel approach that significantly improves the CCDF performance of SC-FDMA signals.

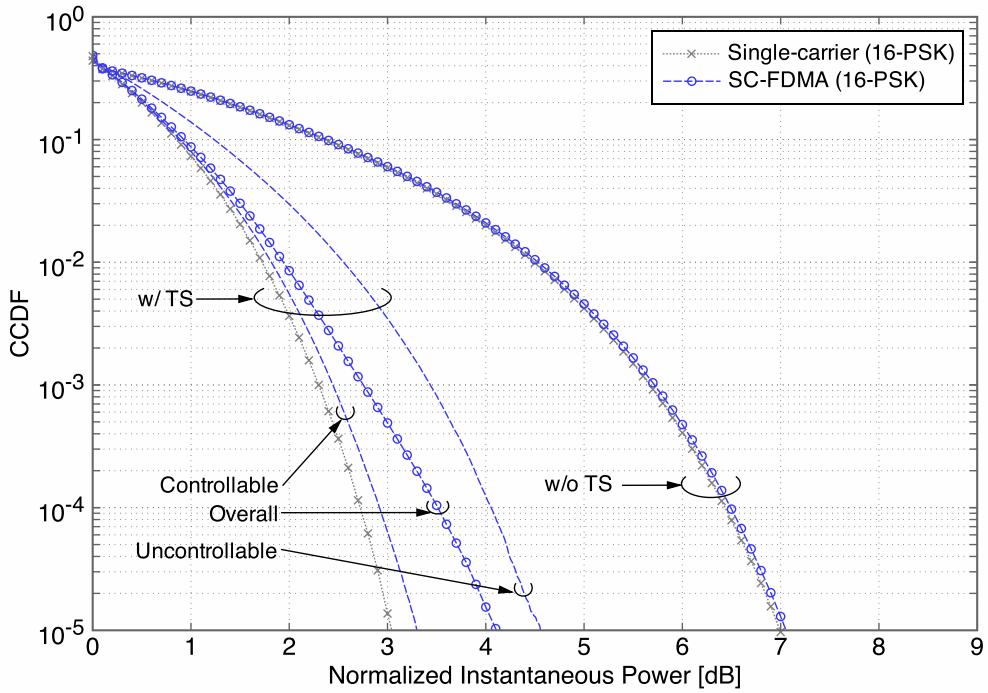

Figure 5.4: CCDF performances of TS applied SC-FDMA signal.

5.4 A New TS Approach for SC-FDMA

In this section, we describe a new TS approach that is adjusted to SC-FDMA signals. The previous section has demonstrated the major problem that one may face upon direct application of the conventional TS to SC-FDMA; it fails to reduce the peak power of the waveform in the edge region. This is due to the fact that TS cannot take into account the continuity of the waveform between the head and tail of the SC-FDMA symbols. In our previous work [LO12], we tackle with this problem based on the repetitive application of TS. Even though good peak power control at the edge can be achieved, the computational complexity turns out to be substantial. This has motivated us to introduce a low complexity TS algorithm that can effectively control the peak power of SC-FDMA signals at these edge regions.

Recall that for the transmit QAM sequence $\mathbf{x}$ to be determined by TS, each QAM symbol x_n is formed by $\mathbf{z}_n$ and $\mathbf{u}_n$, where the former consists of n_s bits and used for shaping (MSBs), and the latter consists of n_u bits as non-shaping (LSBs). Once an information sequence is given from the source, the TS determines $\mathbf{z}$ (or equivalently, $\mathbf{v}$ for given $\mathbf{s}$), whereas $\mathbf{u}$ is determined *a priori*.

1. **Appending prefix:** We first append the prefix symbols of length $K_s - 1$, at the head of the candidate sequence $\tilde{\mathbf{x}}$ similar to (5.21). They are expressed as $\tilde{\mathbf{x}}_h =$

$[\tilde{x}_{h,-K_s+1}, \cdots, \tilde{x}_{h,-2}, \tilde{x}_{h,-1}]$. Let $\mathbf{z}_{h,n}$ and $\mathbf{u}_{h,n}$ denote that MSBs and LSBs of $\tilde{x}_{h,n}$, respectively. The MSBs $\mathbf{z}_{h,n}$ are set as zeros, whereas its LSBs are chosen such that $\mathbf{u}_{h,-n} = \mathbf{u}_{N-n}$ for $n = 1, 2, \cdots, K_s - 1$.

2. Do the following for $k = 0, 1, \cdots, K_{\max} - 1$, where $K_{\max} \geq K_s$:

   (a) **Partial signal generation:** For each trellis section with the candidate MSB given by $\mathbf{z}_k$, generate x_k and calculate $\hat{x}_k^{(q)}(l')$ according to (5.17).

   (b) **Branch metric calculation:** Calculate the corresponding branch metric μ_k.

   (c) **Viterbi decoding:** Perform the ACS operation of the Viterbi Algorithm to determine the survivor branch for each trellis section. This process is necessary only when the number of the trellis states is smaller than $2^{K_{\max}}$.

3. **First trace back:** When $k = K_{\max} - 1$, trace back the path with the minimum metric to determine the first $K_{\max}$ symbols of $\tilde{\mathbf{x}}$.

4. **Appending post-fix:** Append the obtained sequence to the tail of $\mathbf{x}$ as the post-fix such that

$$\tilde{\mathbf{x}}' = [\tilde{x}_0, \tilde{x}_1, \cdots, \tilde{x}_{N-1}, \underbrace{\tilde{x}_{t,0}, \tilde{x}_{t,1}, \cdots, \tilde{x}_{t,K_{\max}-1}}_{K_{\max}}], \tag{5.22}$$

   where $\tilde{x}_{t,n} = \tilde{x}_n$ for $n = 0, 1, \cdots, K_{\max}$.

5. Do the following for $k = K_{\max}, K_{\max} + 1, \cdots, N - 1$:

   (a) **Partial signal generation:** For each trellis section with the candidate MSB given by $\mathbf{z}_k$, generate $\tilde{x}_k$ and calculate $\hat{x}_k^{(q)}(l')$ according to (5.17).

   (b) **Branch metric calculation:** Calculate the corresponding branch metric μ_k.

   (c) **Viterbi decoding:** If necessary, perform the ACS operation to determine the survivor branch for each trellis section.

6. **Branch extension:** Extend the branch of the trellis by $K_{\max}$ symbols according to the appended post-fix. Since the symbols in these branches have been uniquely determined, the ACS operation may not be required. Only the metrics of the corresponding paths should be updated.

7. **Second trace back:** When $k = N - 1 + K_{\max}$, trace back the path corresponding to the trellis of $\tilde{\mathbf{x}}'$ with the minimum metric to determine the entire symbols $\mathbf{x}$ to be transmitted through the SC-FDMA encoder.

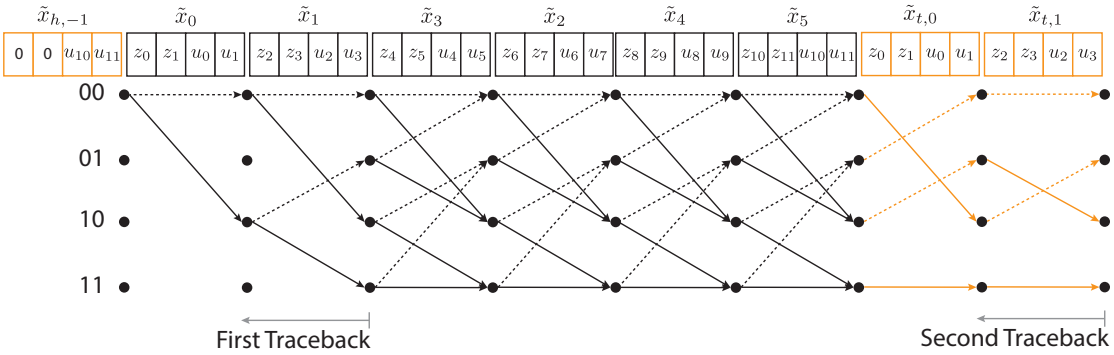

Figure 5.5: An example trellis of the proposed approach for $N = 6$, $K_s = 2$, and $K_{\max} = 2$ with $\nu = 1$ (four-state trellis).

It is not necessarily guaranteed that the tail symbols in the extended region $\tilde{\mathbf{x}}'$ agree with those at the beginning of the selected symbols in $\mathbf{x}$ after the second trace back. We have found that if they match each other, it results in the better peak power reduction performance.

As an example case, TS with $N = 6$, $K_s = 2$, $K_{\max} = 2$, and four-state trellis is illustrated in Fig. 5.5.

5.5 Peak Power Reduction Performance Optimization

In this section, we numerically optimize the peak power reduction performance of the SC-FDMA system with the proposed TS described in the previous section, through the selection of the threshold parameters required for metric calculation.

5.5.1 Reference and Peak Power Levels for TS

In our branch metric calculation of 16-PSK signals, the metrics in (5.18) and (5.19) will be employed, where a proper setting of reference level p_{ref} is critical for effective reduction of peak power. Furthermore, in the case of QAM based on the metric (5.20), both p_{ref} and p_{peak} should be carefully selected for effective reduction of average power as well as peak-to-average power ratio. In what follows, we define the peak-to-average power ratio (PAPR) as the threshold level of the normalized instantaneous power where the CCDF is 10^{-3}. The parameters of TS considered in the rest of this work are summarized in Table 5.1.

Through extensive computer simulations, we evaluate the PAPR as a function of p_{ref} for 16-PSK and the result is shown as the dashed curve in Fig. 5.6. It is observed that

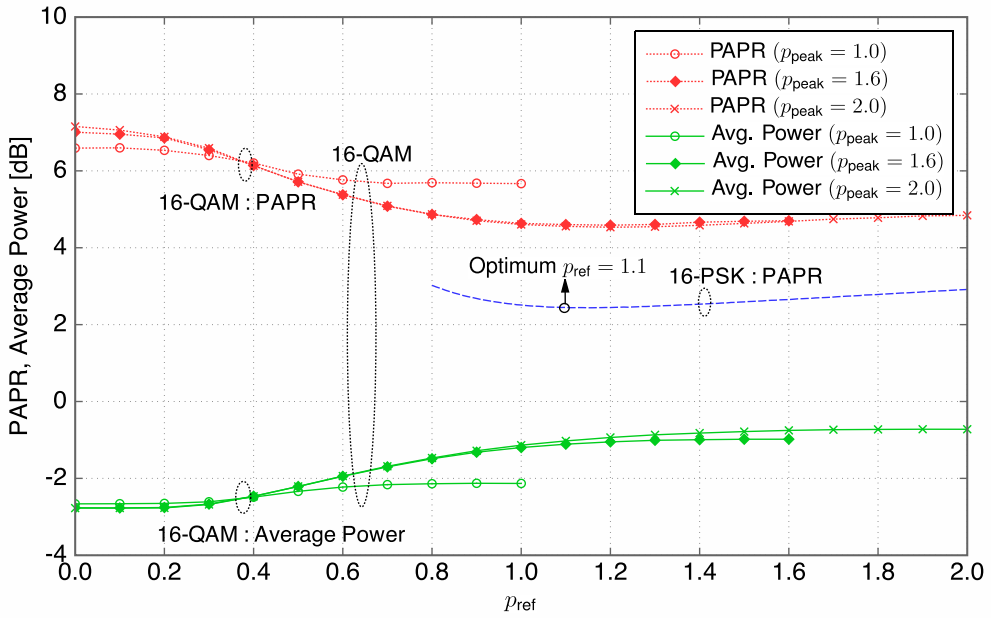

Figure 5.6: Relationship between the peak-to-average power ratio and average power for given parameters p_{ref} and p_{peak}.

there is an optimal value of p_{ref} (which is 1.10 in this case) that minimizes the PAPR in the case of 16-PSK.

In the case of 16-QAM, it is necessary to jointly optimize the parameter pair p_{ref} and p_{peak}. By changing p_{peak} from 1.0 to 2.0, we have evaluated the resulting average power and PAPR as a function of p_{ref} and the results are shown as the corresponding curves in Fig. 5.6. We observe that when p_{peak} is low, peak power can be reduced but the average power is also reduced, thus resulting in relatively high PAPR. On the other hand, as p_{peak} increases, PAPR is reduced but the average power is also increased, thus less shaping gain can be expected from the average power reduction. A reasonable selection of p_{peak} will be around 1.6, while changing p_{ref} offers a trade-off relationship between the PAPR and average power.

5.5.2 Peak Power Reduction Performance

Figure 5.7 shows each CCDF results of conventional and proposed TS methods. All results of TS has the partial wave symbol length of eight. We observe that our proposed method improves peak power reduction performance of 0.5 dB for 16-PSK and 1 dB for 16-QAM compared to conventional TS at the probability of 10^{-5}.

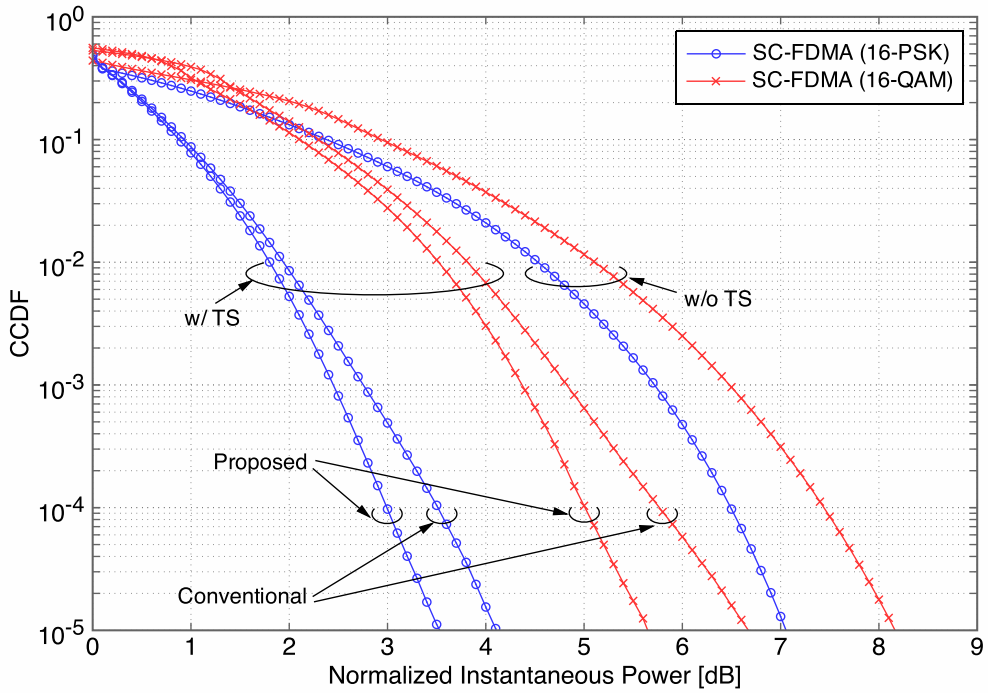

Figure 5.7: CCDF performances of our proposed TS method. It outperforms conventional TS as 0.5 dB and 1.0 dB for 16-PSK and QAM at target CCDF of 10^{-5}, respectively.

5.6 System Level Simulation Results

5.6.1 Effect of PA Nonlinearity

As we investigated in above section, TS is also valid in SC-FDMA signal as well. In this section, we investigate the performance of the proposed TS with the specification shown in Table 5.1.

In order to investigate nonlinear distortion caused by PA, we adopt PA model as solid state power amplifier (SSPA) known as Rapp model [Rap91] given by

$$g_{\mathrm{PA}}(r) = \frac{r}{(1 + (r/A_{\max})^{2p})^{\frac{1}{2p}}}, \tag{5.23}$$

where $A_{\max}$ denotes maximum output envelope level of r and p is smoothness factor from linear to saturation region. Note that p is chosen by the kind of target PA. Generally, $p = 3$ is suitable for high power amplifier (HPA) whereas $p = 2$ corresponds to moderate PA (see [Och13] and references therein). In this work, we adopt $p = 2$ to investigate performances in severe nonlinear distortion with no phase distortion (AM-PM).

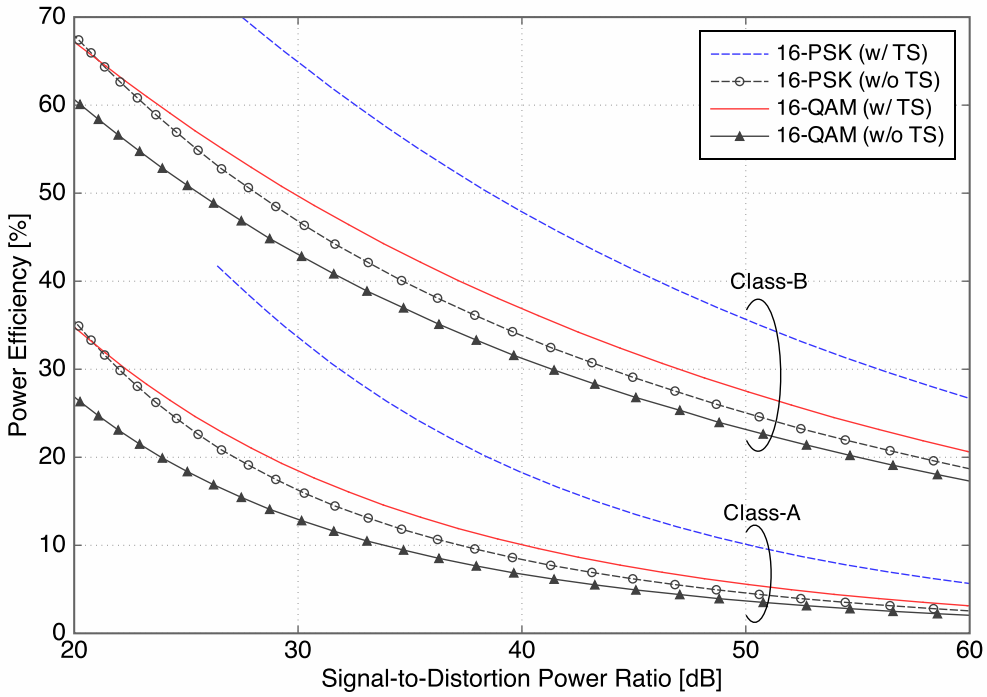

Figure 5.8: Power efficiency of SC-FDMA with and without TS for class-A and B PA.

The input back-off (IBO) of the PA is generally defined as a ratio of saturation power $P_{\text{sat}} = (A_{\max})^2$ to input signal average power P_{avg} as

$$\text{IBO} = \frac{P_{\text{sat}}}{P_{\text{avg}}} = \frac{(A_{\max})^2}{E\left\{\left|\tilde{x}_m^{(q)}\right|^2\right\}}, \tag{5.24}$$

where $E\{\cdot\}$ denotes mean value. The lower IBO has an advantage of higher PA efficiency, but it may cause severe nonlinear distortion unless PAPR is reduced accordingly.

5.6.2 Power Efficiency

The power efficiency is generally defined by direct current (DC) power supplied to PA and the RF signal power converted by the PA as [Och13]

$$\eta = P_{\text{RF}}/P_{\text{DC}}. \tag{5.25}$$

In other words, since P_{DC} is constant, power efficiency totally depends on the amplified output signal power P_{RF}. For example, the signal bearing high PAPR such as OFDM signal should be amplified around the region well below saturation in order to avoid

Table 5.2: Corresponding IBO value for SDR = 30 dB.

16-PSK		16-QAM	
Non-shaped	Trellis-shaped	Non-shaped	Trellis-shaped
4.5 dB	0.5 dB	5.5 dB	3.5 dB

nonlinear amplification by reducing input signal power. Consequently, the achievable PA efficiency is significantly decreased. The power efficiency of class A and B can be derived by (see [Och13] and references therein)

$$\eta_{\text{av,A}} = \frac{1}{2} M_2(r_{\max}) \text{ and } \eta_{\text{av,B}} = \frac{\pi}{4} \frac{M_2(r_{\max})}{M_1(r_{\max})} \tag{5.26}$$

where $M_n(\cdot)$ denotes the normalized nth non-central moment. By using (5.26),together with the CCDF curves obtained in Fig. 5.7, the power amplifier efficiency of both classes can be derived.

The signal-to-distortion power ratio (SDR) is a good measure for distorted signal. In [Och13], SDR can be obtained by PA characteristic and CCDF of PA input signal given by

$$\text{SDR}_{\text{design}} = \frac{|\rho_s|^2}{1 - |\rho_s|^2}, \tag{5.27}$$

where ρ_s denotes cross-correlation coefficient between PA input and output signal.

Figure 5.8 shows power efficiency results against SDR for amplified transmit SC-FDMA signal. As we expected, since trellis-shaped signal takes less nonlinear distortion than that of non-shaped one, the power efficiency is considerably improved. For example, in the case of 16-PSK SC-FDMA signal at 30 dB SDR, TS can improve the power efficiency increase as approximately 18 percent for both class-A and B PA, respectively. On the other hand, in the case of 16-QAM, we obtain the power efficiency increase as about 6 percents for both PAs. This is due to the peak power reduction performance as shown in Fig. 5.4.

For the consideration of trade-off relationship between power efficiency and signal quality, it is essential to investigate performance variation in terms of PSD for out-of-band and SER for inband quality. In following subsections, we further investigate them to verify validation of TS with above example for SDR = 30 dB. It should be noted that even transmit signals have same SDR, its IBOs vary depending on peak-to-average power ratio. In our example case, the corresponding IBOs are summarized in Table 5.2.

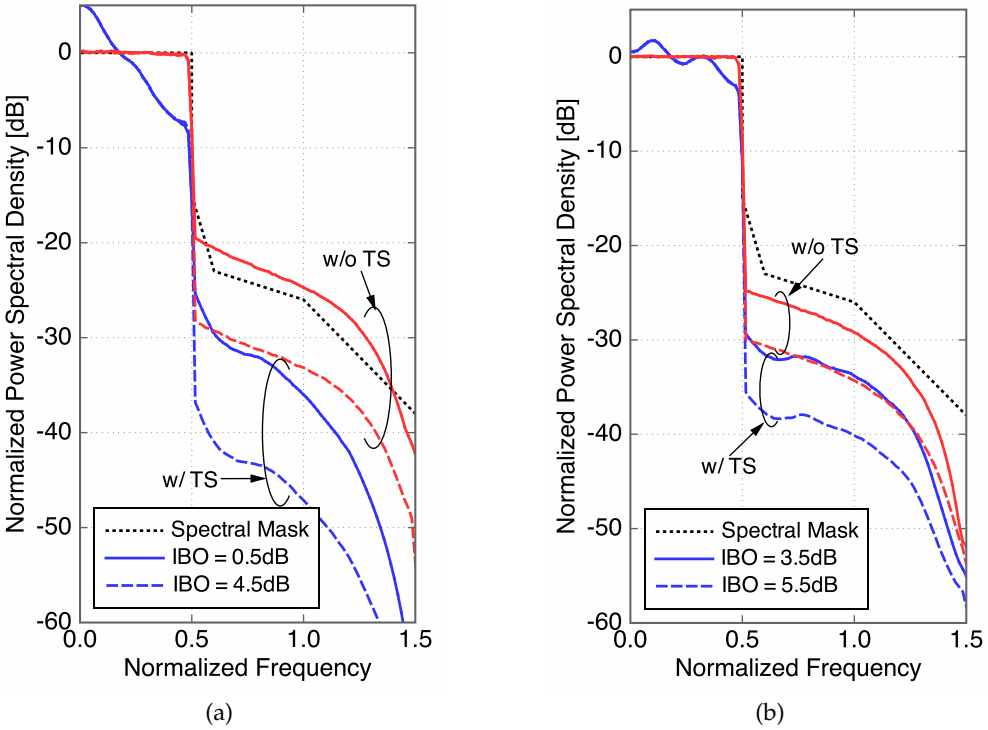

Figure 5.9: Power spectral density for (a) 16-PSK and (b) 16-QAM.

Similar to power efficiency result, we observed that TS can significantly reduce IBO as 4 dB for 16-PSK, and 2 dB for 16-QAM.

5.6.3 Out-of-band Spectral Emission

Figure 5.9 shows the power spectral density results. All results are normalized by in-band average power. It is noted that we adopt LTE spectral emission mask to compare the results. In case of 16-PSK, all the transmit signals with corresponding IBO listed in Table 5.2 are satisfied with spectral emission mask of LTE standard. However, once the IBO of non-shaped signal is set to same value with that of trellis-shaped, it undergoes severe nonlinear distortion so that its PSD exceeds the spectral emission mask. Similarly, TS significantly improves out-of-band spectral emission for 16-QAM signal. In this case, non-shaped signal with IBO = 3.5 dB which is corresponding one for TS nearly approaches spectral emission mask. From these results, we see that TS can significantly improve adjacent channel interference. Note that the PSD shape of in-band for SC-FDMA with TS does not coincide with the conventional SC-FDMA. This is due to the correlation between successive symbols introduced by the TS.Since the TS imposes correlation to the data symbol sequence such that the peak power is reduced, the

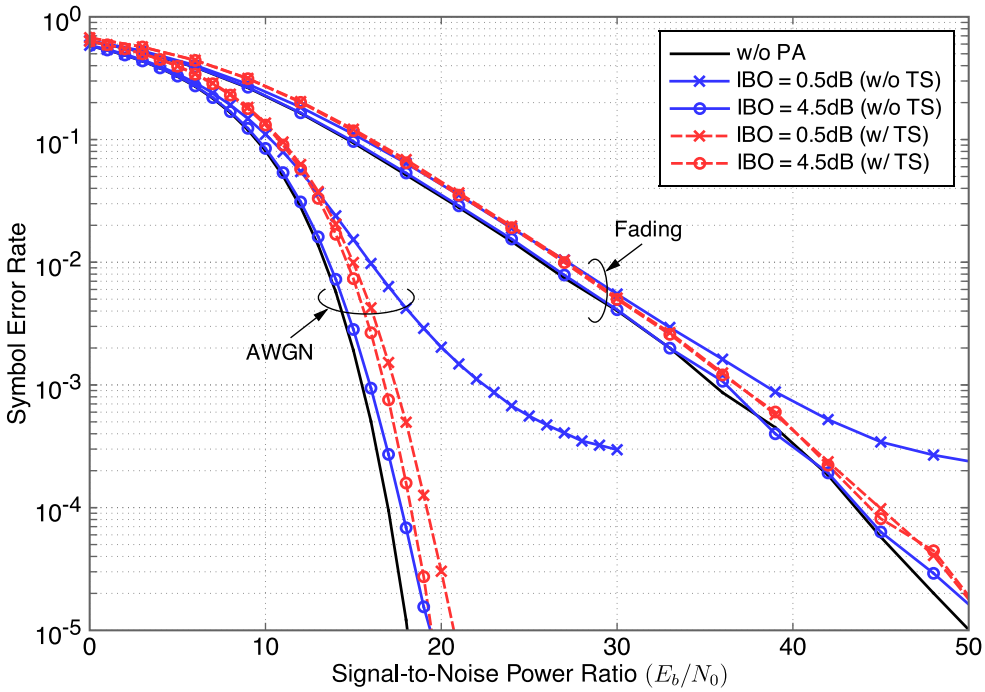

Figure 5.10: Symbol error rate for 16-PSK over AWGN and Rayleigh fading channel

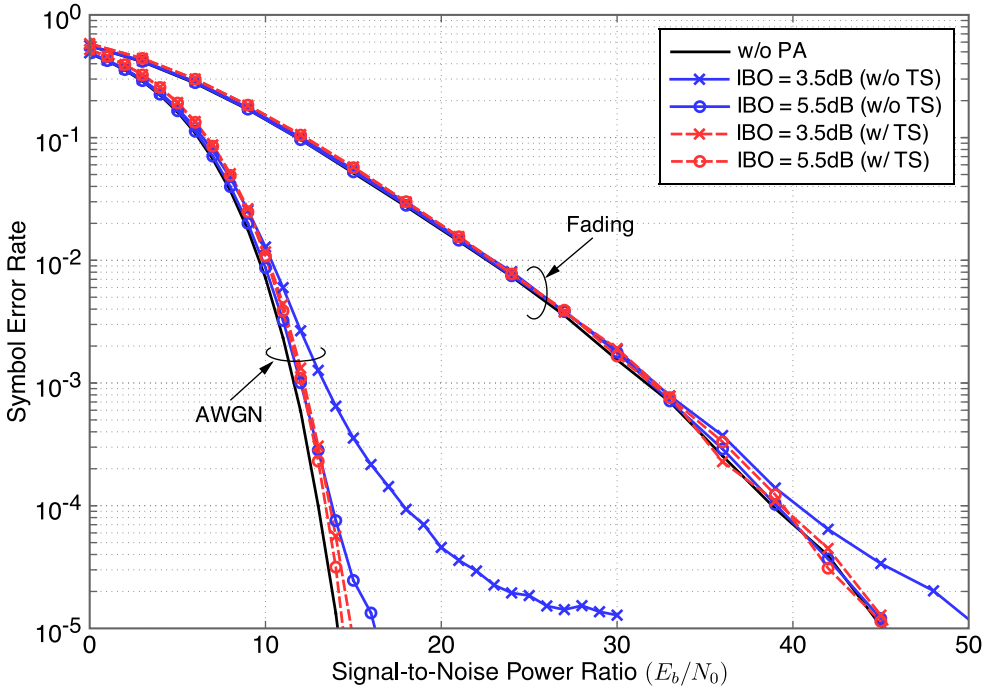

Figure 5.11: Symbol error rate for 16-QAM over AWGN and Rayleigh fading channel

resulting PSD shape will not be flat as observed in the corresponding results in Fig. 5.9 (a) and (b).

5.6.4 Symbol Error Rate

We evaluate the SER performance of the proposed TS over AWGN and a two-path frequency selective Rayleigh fading channels. For the latter channel, we use a MMSE equalizer as described in section 5.2, and perfect channel state information is assumed at the receiver in our work.

Figures 5.10 and 5.11 show the SER results of uncoded 16-PSK and QAM SC-FDMA system over AWGN and frequency selective fading channels, respectively. Since TS imposes the correlation between symbols to reduce peak power as mentioned before, and thus, a single error introduces burst errors. As a result, the SER performances of trellis-shaped PSK signal is slightly worse than those of one without TS in both fading and AWGN channels. On the other hand, such gap can be mitigated in the case of 16-QAM due to average power reduction. In the circumstance of same IBO, the average power of the transmit signal from the output of PA is increased by the factor of α_p so that expression (5.24) can be rewritten by

$$\text{IBO} = \frac{(A_{\max})^2}{E\left\{\alpha_p \left|\tilde{x}_m^{(q)}\right|^2\right\}}. \tag{5.28}$$

Consequently, the transmit signal has higher power against channel noise power by recalling (5.12) as

$$\bar{x}_m^{(q)} = \frac{1}{\sqrt{QN}} \sum_{n=0}^{QN-1} T_n^{(q)} \Upsilon_n^{(q)} \left\{ \sqrt{\alpha_p} x_n^{(q)} + \sum_{\substack{l=0 \\ l \neq n}}^{QN-1} \sqrt{\alpha_p} x_l^{(q)} e^{j2\pi m \frac{(l-n)}{QN}} + \sum_{k=0}^{QN-1} \tilde{w}_k e^{j2\pi m \frac{(k-n)}{QN}} \right\}. \tag{5.29}$$

In our system model, TS uses one bit redundancy so that the bit energy is reduced by the factor of $\frac{3}{4} \approx -1.25$ dB. However, we obtain average power gain of 1 dB, and thus, the gap can be cancelled out.

Also, the proposed TS system outperforms that of without TS as we decrease IBO such that the nonlinear distortion caused by PA dominates. For example, when IBO is set as 0.5 dB for 16-PSK, non-shaped signal severely suffers from nonlinear distortion so that error floor is occurred around 10^{-4} of SER for both AWGN and fading channel. However, trellis-shaped signal can avoid such severe nonlinear distortion although its performance is slightly degraded. This is due to the fact that severe nonlinear distortion

results in non-negligible inband distortion whereas that is not the case for the proposed TS system. In the case of 16-QAM, the SER performance of non-shaped signal with IBO = 3.5 dB also has error floor around 10^{-5} of SER. We can also obtain better performance in Rayleigh fading channel.

5.7 Conclusion

In this chapter, we have proposed a new approach for applying TS to SC-FDMA systems. It has been shown that significant performance improvement in terms of power efficiency can be achieved at the cost of transmitter complexity. With the proposed approach, it is expected that the power consumption of PA in user terminals is mitigated and thus their battery life is prolonged.

Chapter 6

Conclusions

In this dissertation, we have addressed the peak-to-average power ratio problem associated with OFDM and SC-FDMA. The PAPR statistics are studied and the effect of power amplifier nonlinearities as a function of power backoff is evaluated by computer simulation and experiments with real PA. It is shown that the amount of backoff required to reduce spectral growth and associated performance degradation are significant. Large backoff is an undesirable solution for battery-powered systems since PA efficiency is low.

With the clipping and filtering as a simple peak power reduction technique, the spectral regrowth can be suppressed even with insufficient backoff. However, it dramatically degrades the inband signal quality. By applying the CAF to IEEE 802.11g, we verified that the CAF may not necessarily improve the performance under severe nonlinear conditions.

Since there is a critical problem of the lack of frequency resource in recent wireless communication systems, the adjacent channel interference caused by nonlinear distortion in PA should be suppressed. For this reason, the spectral regrowth should be analyzed in the process of system design. In order to obtain exact estimation, the analysis requires accurate curve fitting of PA characteristic, and higher order calculation process in the conventional method. On the other hand, we proposed a new method only with the third-order nonlinear term. In addition, since our proposed method does not require curve fitting, the estimation can be performed by simple calculation without sacrificing the accuracy compared with the conventional approach. The results are verified through both simulation and experiment with real PA.

Even though the peak-to-average power ratio of SC-FDMA signal is much lower than that of OFDM, it is required to achieve even lower peak power due to the fact that

SC-FDMA is adopted in user equipment of LTE-Advanced. The user equipment is operated by battery so that it is essential to reduce peak power in order to improve battery life. Our propose method starts from the fact that SC-FDMA is inherited from single-carrier, and thus, the peak power reduction method for single-carrier may be applied to SC-FDMA. The trellis shaping leads to good performance in single-carrier system, but it requires modification upon its application to SC-FDMA due to the structural problem, namely circular convolution. By judicious arrangement of dummy symbols upon Viterbi algorithm, we have succeeded in effective reduction of the peak power of SC-FDMA signals.

Remaining issues that should be addressed in future include the followings.

- Extension of theoretical analysis of power spectral density to SC-FDMA which does *not* follow Gaussian distribution.
- Investigation of channel coding with trellis shaping.

Appendix A

Derivation of Nonlinear Coefficient C_n for Ideal PA

We define the regularized Gamma function as follow:

$$Q(a,z) \triangleq \frac{\Gamma(a,z)}{\Gamma(a)}. \tag{A.1}$$

Then (4.23) can be rewritten by

$$C_n = \frac{1}{(n+1)} \left| \sum_{k=0}^{n} \binom{n+1}{k+1} \frac{(-1)^k}{k!} \Gamma(k+2) \left\{ 1 - Q(k+2,\gamma^2) + \frac{\gamma\Gamma\left(\frac{3}{2}+k,\gamma^2\right)}{\Gamma(k+2)} \right\} \right|^2. \tag{A.2}$$

Since $\Gamma(a) = (a-1)\Gamma(a-1)$, the last term of (4.23) can be rewritten by

$$\begin{aligned} \frac{\Gamma\left(\frac{3}{2}+k,\gamma^2\right)}{\Gamma(k+2)} &= \frac{\Gamma\left(\frac{3}{2}+k,\gamma^2\right)}{\Gamma\left(\frac{3}{2}+k\right)} \cdot \frac{\Gamma\left(\frac{3}{2}+k\right)}{\Gamma(2+k)} \\ &= Q\left(\frac{3}{2}+k,\gamma^2\right) \frac{(k+\frac{1}{2})\Gamma(k+\frac{1}{2})}{(k+1)!} \\ &= \sqrt{\pi} Q\left(\frac{3}{2}+k,\gamma^2\right) \prod_{l=0}^{k} \frac{2l+1}{2l+2}. \end{aligned} \tag{A.3}$$

By substituting (A.3) into (A.2), then we can rewrite (A.2) as

$$\begin{aligned}
C_n &= \frac{1}{(n+1)}\left|\sum_{k=0}^{n}\binom{n+1}{k+1}(-1)^k(k+1)!\left\{1-Q(k+2,\gamma^2)+\gamma\sqrt{\pi}Q\left(\frac{3}{2}+k,\gamma^2\right)\prod_{l=0}^{k}\frac{2l+1}{2l+2}\right\}\right|^2 \\
&= \frac{1}{(n+1)}\left|\sum_{k=0}^{n}\binom{n+1}{k+1}(-1)^k(k+1)!\right. \\
&\qquad \left.\times\left\{1-e^{-\gamma^2}\left(\sum_{l=0}^{k+1}\frac{\gamma^{2l}}{l!}\right)+\prod_{l=0}^{k}\frac{2l+1}{2l+2}\left[\sqrt{\pi}\gamma\text{erfc}(\gamma)+e^{-\gamma^2}\left\{\sum_{l=1}^{k+1}\frac{\gamma^{2l}}{(\frac{1}{2})_l}\right\}\right]\right\}\right|^2 \\
&= \frac{1}{(n+1)}\left|\sum_{k=0}^{n}\binom{n+1}{k+1}(-1)^k(k+1)!\right. \\
&\qquad \left.\times\left\{1-\left(1+\sum_{l=1}^{k+1}\left[\frac{1}{l!}-\frac{F_k}{(\frac{1}{2})_l}\right]\gamma^{2l}\right)e^{-\gamma^2}+F_k\sqrt{\pi}\gamma\text{erfc}(\gamma)\right\}\right|^2
\end{aligned} \tag{A.4}$$

where $(a)_k$ is Pochhammer symbol given by

$$(a)_k = \frac{\Gamma(a+k)}{\Gamma(a)} = a(a+1)(a+2)\cdots(a+k-1) = \prod_{l=0}^{k-1}(a+l), \tag{A.5}$$

and therefore, we can define F_k as

$$F_k \triangleq \prod_{m=0}^{k}\frac{2m+1}{2m+2}. \tag{A.6}$$

Appendix B

Description of Experimental Process

In this Appendix, we describe the demodulation and estimation methods for experimental analysis of distortion for nonlinearly amplified OFDM in Chapter 3 and Chapter 4.

The data used for generating input OFDM signals is chosen to be exactly the same as those used in the simulation process for the fair comparison. The complex baseband OFDM signal is thus generated by a computer and then up-converted to the RF signal by the vector signal generator (VSG). The number of the OFDM symbols generated for measurement is 576 000. The RF modulated signal by VSG is then power amplified by the actual PA, and then is fed, after attenuation of the signal power, to the oscilloscope where the power amplified signal is captured and down-converted to the baseband OFDM signals. Finally, the captured data is analyzed in computer in terms of the resulting PSD and EVM. Throughout the experiment, we have maintained the temperature on the surface of the PA package such that the electrical memory effect is stable [VR01].

Figure B.1: A frame composition of transmit data

B.0.1 Transmitter Side

In order to detect and analyze signal through practical evaluation, the transmit signal is required to be composed of appropriate format. The entire frame format illustrated in Fig.B.1 is largely categorized into the following three parts: null symbols, training

sequence and data frame. Null symbols play a role to detect the beginning of the frame. The training sequence is used for coarse channel estimation. It is composed by the one similar to IEEE 802.11a standard [Ieeb]. The difference is that we expand the number of subcarriers from $N = 64$ to 256 in this research. It consists of 60 consecutive and 196 null subcarriers. Consecutive subcarriers are modulated by binary phase shift keying (BPSK) given by

$$X_{T_r,k} = \begin{cases} Z_i & : k = 4 * i + 8, \\ 0 & : \text{otherwise} \end{cases} \tag{B.1}$$

where $i = \{0, 1, 2, \cdots, 59\}$ and

$$Z_i = \{1, 1, -1, -1, 1, 1, -1, 1, -1, 1, 1, -1, 1, 1, 1, -1, 1, 1, 1, 1, 1, -1, -1, 1, -1, 1, -1, -1, 1, 1, 1, \\ -1, -1, -1, -1, -1, 1, -1, 1, 1, 1, -1, -1, 1, 1, 1, 1, 1, -1, -1, -1, 1, -1, -1, -1, -1, -1, 1, -1, 1\} \tag{B.2}$$

The training sequence is generated by N-point FFT with $X_{T_r,k}$ given by

$$s(t) = \frac{1}{\sqrt{N}} \sum_{k=0}^{N-1} X_{T_r,k} e^{j2\pi kt/N} \tag{B.3}$$

As a result, the training sequence $s(t)$ has a periodicity of $N/4$, and its peak-to-average power ratio is extremely low (i.e., approximately 1.5 dB). In order to perform more precise estimation, it is required to prolong the training signal. From this fact, we compose the training signal with three copies of $s(t)$, such that it has a periodicity of twelve as shown in Fig. B.1.

Followed by training sequence, the average power adjusted transmit signal data is allocated in order with IBO difference. From this allocation, we can obtain the exact data against even fast time varying channel (wired connection between vector signal generator (VSG) and PA or PA and spectrum analyzer (SPA)). The data frame is composed of a set of five different IBO valued transmit signal, and its length is $5 \times N_F$ where N_F is the number of frame. There are 16 pilots in each OFDM symbol, and DC subcarrier is set as null. Figure B.2 shows the actual transmit signal wave captured in oscilloscope.

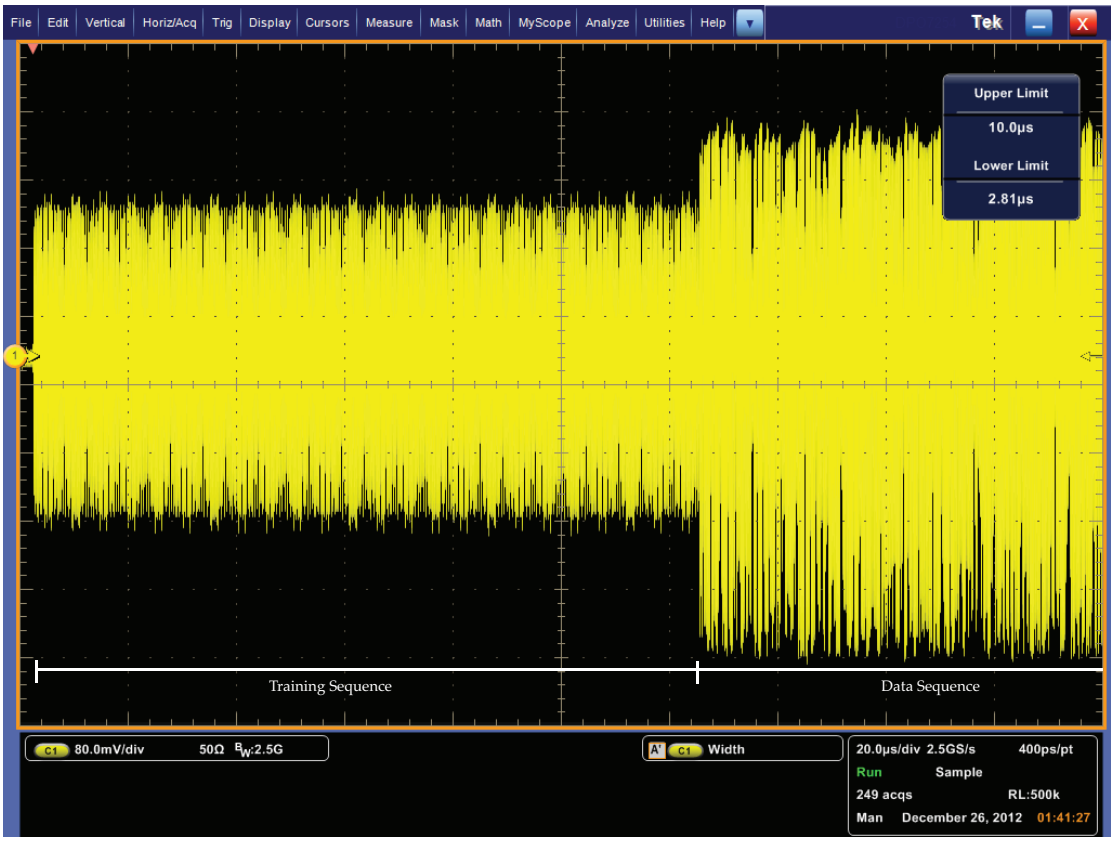

Figure B.2: Actual transmit signal wave captured in oscilloscope.

B.0.2 Receiver Side

Data Acquisition

The amplified signal from PA is acquired by oscilloscope or spectrum analyzer. Since we set the bandwidth of transmit data as 12.5 MHz bandwidth, and the carrier frequency as 800 MHz, sampling frequency of f_s = 2500 MHz is sufficient to capture the RF signals.

Signal Detection

Since we insert null symbols at the head of transmit frame as shown in Fig. B.2, we can detect the transmit signal if we recognize null signal. Since null signal has extremely low power in comparison with transmit signal, and therefore it can be detected by calculating its signal power.

Carrier Suppression

The carrier frequency f_c can be simply removed by using trigonometric identity. We assume that $v[n]$ is complex passband signal given by

$$v[n] = s(nT_s)e^{jw\pi f_c nT_s} = v_{\text{RE}}[n]\cos(2\pi f_c nT_s) + jv_{\text{IM}}[n]\sin(2\pi f_c nT_s) \tag{B.4}$$

where $v_{\text{RE}}[n]$ and $v_{\text{IM}}[n]$ denote real and imaginary components of passband signal $v[n]$. The frequency components f_c are simply suppressed by multiplying exactly the same frequency f_c' to $v[n]$ given by

$$\tilde{v}[n] = v[n]e^{-j2\pi f_c' nT_s} = s(nTs)e^{j2\pi(f_c - f_c' nT_s)}. \tag{B.5}$$

Finally, the lowpass filter ejects the baseband signal as

$$r[n] = \sum_{k=0}^{K-1} h[k]\tilde{v}[n+k], \tag{B.6}$$

where $h[k]$ is filter impulse response of raised cosine given by

$$h[k] = \text{sinc}(\pi k T_s)\frac{\cos(\pi\alpha k T_s)}{1-(2\alpha k T_s)^2}, \tag{B.7}$$

and α is rolloff factor with $\text{sinc}(x) = \frac{\sin(x)}{x}$.

Synchronization

In synchronization process, we use the preamble signal due to the fact that it is known signal at the receiver, and therefore the synchronization can be achieved by investigating cross correlation between transmitted and received signals. The received signal is oversampled by OSC as a factor of $O_v = \frac{JB}{f_s}$. We define the received preamble signal $r_p[n_c] = r[n_c]$, where $n_c = \{0, 1, \cdots, N_c \times O_v - 1\}$, and N_c denotes the number of preamble data. In this work, we use three permutations of one OFDM preamble, thus $N_c = JN \times 3 = 2 \times 256 \times 3 = 1536$. Subsequently, the cross correlation ρ can be calculated by

$$\rho[n_c] = \sum_{n=0}^{JN-1} x_p[n] r_p[O_v \times n + n_c], \tag{B.8}$$

where synchronization point is n_c that has the maximum value of $\rho[n_c]$. In what follows, we reset the data index n_c as zero.

B.0.3 Compensation

The received signal is compensated by initial phase error θ and carrier frequency offet f_{Δ_f} to data signal r_d as follows:

$$\tilde{r}_d[n_d] = r_d[n_d]e^{-j2\pi f_{\Delta_f} * n_d/f_s - \theta} \tag{B.9}$$

Sampling Timing Error

In order to demodulate OFDM symbol successfully, the exact synchronization is required. In particular, the sampling timing error may lead to synchronization error, and thus it has a critical effect on signal quality. In this work, we simply solve the problem to interpolate the received signal by low pass filtering. Since the training signal is known, we can determine the synchronization timing by obtaining the cross-correlation $\rho_{<r,x>}(t)$ between the received and interpolated signal $r(t)$ and the transmit signal $x(t)$ [Cou01; SC97] as

$$\rho_{<r,x>}(t) = \int_{-\infty}^{\infty} r(\tau)x(t-\tau)d\tau. \tag{B.10}$$

We assume the exact sampling timing point when $\rho_{<r,x>}(t)$ has the maximum value.

Initial Phase Error

The received signal which has an initial phase error can be expressed by

$$r[n] = x[n]e^{j\theta}. \tag{B.11}$$

In consideration of the periodicity of preamble signal, initial phase error can be simply compensated by using preamble signal as follows:

$$\theta = \arctan\left\{\frac{r[n]x^*[n]}{|x[n]|^2}\right\}, \tag{B.12}$$

where $r^*[\cdot]$ denotes the complex conjugate of $r[\cdot]$.

Frequency Offset

In order to investigate the frequency offset, we use preamble signal and its periodicity. As mentioned earlier, since the preamble signal has three permutations of one OFDM frame, we can estimate the frequency offset by comparing the signal of permutations. Assuming that f_{TX} and f_{RX} are carrier frequency of VSG and local oscillator frequency of OSC, respectively, then the baseband signal can be expressed by

$$r[n_f] = x_p[n_f]e^{j2\pi(f_{\text{TX}}-f_{\text{RX}})n_f T_s} \tag{B.13}$$

where $n_f = \{\text{integer} : 0, 1, \cdots, N_c \times O_v - 1\}$. We can obtain the frequency $f_{\Delta_f} = f_{\text{TX}-f_{\text{RX}}}$ by multiplying $r^*[n_f + N_c \times O_v - 1]$ to (B.13) given by

$$r[n_f]r^*[n_f + N_c \times O_v] = x_p[n_f]e^{j2\pi f_{\Delta_f} n_f T_s} x_p[n_f + N_c \times O_v]e^{-j2\pi f_{\Delta_f}(n_f+N_c\times O_v)T_s} \tag{B.14}$$

$$= |x_p[n_f]|^2 e^{-j2\pi f_{\Delta_f} N_c \times O_v T_s} \tag{B.15}$$

and thus, its phase is

$$\arg\{r[n_f]r^*[n_f + N_c \times O_v]\} = -2\pi f_{\Delta_f} N_c \times O_v T_s \tag{B.16}$$

Consequently, we can obtain the frequency offset given by

$$f_{\Delta_f} = \frac{\arg\{r[n_f]r^*[n_f + N_c \times O_v]\}}{-2\pi N_c \times O_v T_s} \tag{B.17}$$

Pilot Compensation in Data Frame

The frequency components $\tilde{X}_k$ include pilot subcarrier $\tilde{X}_l^p$. We use pilot symbols to estimate signal attenuation and phase distortion. The estimation is performed by averaging all pilot symbols given by signal attenuation:

$$\alpha = \sqrt{E\{|\tilde{X}_l^p|^2\}}, \tag{B.18}$$

phase distortion:

$$\theta_p = \arg\{E\{\sqrt{|\tilde{X}_l^p|^2}\}\}, \tag{B.19}$$

where $l = \{8, 24, 40, 56, 72, 88, 104, 120, 136, 152, 168, 184, 200, 216, 232, 248\}$. Subsequently, the frequency components are compensated and normalized by α and θ_p as

$$\hat{X}_k = \frac{1}{\alpha}\tilde{X}_k e^{j\theta_p}. \tag{B.20}$$

Bibliography

[Ahm+13] I Ahmad et al. "Spectral broadening effects of high-power amplifiers in MIMO-OFDM relaying channels". In: *EURASIP J. Wireless Commun. Netw* 2013.1 (2013), p. 32.

[AN10] Leopoldo Angrisani and Aniello Napolitano. "Modulation quality measurement in WiMAX systems through a fully digital signal processing approach". In: *IEEE Trans. Instrum. Meas.* 59.9 (2010), pp. 2286–2302.

[Bah+02] ARS Bahai et al. "A new approach for evaluating clipping distortion in multicarrier systems". In: *IEEE J. Select. Areas Commun* 20.5 (2002), pp. 1037–1046.

[BB06] Sergio Benedetto and Ezio Biglieri. *Principles of Digital Transmission*. With Wireless Applications. Springer Science & Business Media, Apr. 2006.

[BC00] P Banelli and S Cacopardi. "Theoretical analysis and performance of OFDM signals in nonlinear AWGN channels". In: *IEEE Trans. Commun.* 48.3 (2000), pp. 430–441.

[Ben+10] N Benvenuto et al. "Single carrier modulation with nonlinear frequency domain equalization: an idea whose time has come—again". In: *Proc. IEEE* 98.1 (2010), pp. 69–96.

[Ber+08] G Berardinelli et al. "OFDMA vs. SC-FDMA: performance comparison in local area IMT-A scenarios". In: *IEEE Wireless Commun.* 15.5 (Oct. 2008), pp. 64–72.

[BG89] W Bosch and G Gatti. "Measurement and simulation of memory effects in predistortion linearizers". In: 37.12 (1989), pp. 1885–1890.

[Bla79] N M Blachman. "The output signals and noise from a nonlinearity with amplitude-dependent phase shift". In: *IEEE Trans. Inform. Theory* 25.1 (1979), pp. 77–79.

[Boc+14] F Boccardi et al. "Five disruptive technology directions for 5G". In: *IEEE Commun. Mag.* 52.2 (2014), pp. 74–80.

[Can12] A J Cann. “Improved nonlinearity model with variable knee sharpness”. In: *IEEE Trans. Aerosp. Electron. Syst* 48.4 (2012), pp. 3637–3646.

[Can80] A J Cann. “Nonlinearity model with variable knee sharpness”. In: *IEEE Trans. Aerosp. Electron. Syst* AES-16.6 (1980), pp. 874–877.

[car+10] P Garcia-Du x0301 car et al. “Design and experimental evaluation of a LINC transmitter for OFDM systems”. In: *IEEE Trans. Wireless Commun.* 9.10 (2010), pp. 2983–2987.

[CC05] Mei Chen and O M Collins. “Trellis pruning for peak-to-average power ratio reduction”. In: *Proc. Int. Symp. on Inform. Theory, 2005. ISIT 2005*. IEEE, 2005, pp. 1261–1265.

[CCRTMA07] C Crespo-Cadenas, J Reina-Tosina, and M J Madero-Ayora. “Volterra behavioral model for wideband RF amplifiers”. In: *IEEE Trans. Microwave Theory Techn.* 55.3 (2007), pp. 449–457.

[CMP99] E Costa, M Midrio, and S Pupolin. “Impact of amplifier nonlinearities on OFDM transmission system performance”. In: *IEEE Commun. Lett.* 3.2 (1999), pp. 37–39.

[Cou01] A J Coulson. “Maximum likelihood synchronization for OFDM using a pilot symbol: algorithms”. In: *IEEE J. Sel. Areas Commun.* 19.12 (2001), pp. 2486–2494.

[CSL11] Guoliang Chen, S H Song, and K B Letaief. “A low-complexity precoding scheme for PAPR reduction in SC-FDMA systems”. In: *Proc. IEEE Wireless Commun. and Networking Conference 2011. WCNC 2011*. IEEE, 2011, pp. 1358–1362.

[CZ14] Shanzhi Chen and Jian Zhao. “The requirements, challenges, and technologies for 5G of terrestrial mobile telecommunication”. In: *IEEE Commun. Mag.* 52.5 (May 2014), pp. 36–43.

[Dar] D Dardari. “Joint clip and quantization effects characterization in OFDM receivers”. In: *IEEE Trans. Circuits Syst. I, Reg. Papers* 53.8 (), pp. 1741–1748.

[Erm01] N Y Ermolova. “Spectral analysis of nonlinear amplifier based on the complex gain Taylor series expansion”. In: *IEEE Commun. Lett.* 5.12 (2001), pp. 465–467.

[Fal+02] D Falconer et al. “Frequency domain equalization for single-carrier broadband wireless systems”. In: *IEEE Commun. Mag.* 40.4 (2002), pp. 58–66.

[Fal11] D D Falconer. "Linear precoding of OFDMA signals to minimize their instantaneous power variance". In: *IEEE Trans. Commun.* 59.4 (Apr. 2011), pp. 1154–1162.

[For92] G D Jr Forney. "Trellis shaping". In: *IEEE Trans. Inf. Theory* 38.2 (1992), pp. 281–300.

[Gal59] J Galejs. "Signal-to-noise ratios in smooth limiters". In: *IRE Trans. Inform. Theory* 5.2 (1959), pp. 79–85.

[Gar] W A Gardner. *Introduction to Random Processes with Applications to Signals and Systems. 1985*. McMillan.

[GGS99] K G Gard, H M Gutierrez, and M B Steer. "Characterization of spectral regrowth in microwave amplifiers based on the nonlinear transformation of a complex Gaussian process". In: *IEEE Trans. Microwave Theory Techn.* 47.7 (1999), pp. 1059–1069.

[GYL11] Raghu K Ganti, Fan Ye, and Hui Lei. "Mobile crowdsensing: current state and future challenges". In: *IEEE Commun. Mag.* 49.11 (Nov. 2011), pp. 32–39.

[GZ14] Lei Guan and Anding Zhu. "Green communications: digital predistortion for wideband RF power amplifiers". In: *IEEE Microw. Mag.* 15.7 (Nov. 2014), pp. 84–99.

[Hay01] Simon S Haykin. *Communication systems*. John Wiley & Sons Inc, 2001.

[HBB11] Z Hasan, H Boostanimehr, and V K Bhargava. "Green cellular networks: a survey, some research issues and challenges". In: *IEEE Commun. Surveys Tuts.* 13.4 (2011), pp. 524–540.

[HL05] Seung Hee Han and Jae Hong Lee. "An overview of peak-to-average power ratio reduction techniques for multicarrier transmission". In: *IEEE Wireless Commun.* 12.2 (Apr. 2005), pp. 56–65.

[HNA07] G Huang, A Nix, and S Armour. "Impact of radio resource allocation and pulse shaping on PAPR of SC-FDMA signals". In: *Proc. IEEE 18th Int. Symp. on Personal, Indoor and Mobile Radio Commun., 2007. PIMRC 2007*. IEEE, 2007, pp. 1–5.

[I+14] Chih-Lin I et al. "Toward green and soft: a 5G perspective". In: *IEEE Commun. Mag.* 52.2 (2014), pp. 66–73.

[Ieea] *IEEE Standard for Information Technology- Telecommunications and Information Exchange Between Systems- Local and Metropolitan Area Networks-Specific Requirements Part Ii: Wireless LAN Medium Access Control (MAC) and Physical Layer (PHY) Specifications*. IEEE. 2003.

[Ieeb] *IEEE standard for telecommunications and information exchange between systems - LAN/MAN specific requirements - Part 11: wireless medium access control (MAC) and physical layer (PHY) specifications: high speed physical layer in the 5 GHz band*. IEEE. 1999.

[JT02] ADS Jayalath and C Tellambura. "Peak-to-average power ratio of IEEE 802.11 a PHY layer signals". In: *Advanced Signal Processing for ...* (2002).

[JW08] Tao Jiang and Yiyan Wu. "An overview: peak-to-average power ratio reduction techniques for OFDM signals". In: *IEEE Trans. Broadcast.* 54.2 (2008), pp. 257–268.

[KD11] H S Kim and B Daneshrad. "Power optimized PA clipping for MIMO-OFDM systems". In: *IEEE Trans. Wireless Commun.* 10.9 (2011), pp. 2823–2828.

[LC98] Xiaodong Li and Leonard J Jr Cimini. "Effects of clipping and filtering on the performance of OFDM". In: *IEEE Commun. Lett.* 2.5 (May 1998), pp. 131–133.

[Li+09] Hao Li et al. "A fast digital predistortion algorithm for radio-frequency power amplifier linearization with loop delay compensation". In: *IEEE J. Sel. Topics Signal Process.* 3.3 (2009), pp. 374–383.

[Lia+99] Cheng-Po Liang et al. "Nonlinear amplifier effects in communications systems". In: *IEEE Trans. Microwave Theory Techn.* 47.8 (Aug. 1999), pp. 1461–1466.

[Liu+15] Yi Liu et al. "Integrated energy and spectrum harvesting for 5G wireless communications". In: *IEEE Netw.* 29.3 (2015), pp. 75–81.

[LO12] Taewoo Lee and H Ochiai. "Peak power reduction of SC-FDMA signals based on trellis shaping". In: *Proc. IEEE Global Commun. Conference, 2012. GLOBECOM 2012*. IEEE, 2012, pp. 3268–3273.

[LST14] N P Le, F Safaei, and L C Tran. "Transmit antenna subset selection for high-rate MIMO-OFDM systems in the presence of nonlinear power amplifiers". In: *EURASIP J. Wireless Commun. Netw* 2014.1 (2014), p. 27.

[MLG06] H G Myung, Junsung Lim, and D Goodman. "Single carrier FDMA for uplink wireless transmission". In: *IEEE Veh. Technol. Mag.* 1.3 (2006), pp. 30–38.

[Mor87] D R Morgan. "Finite limiting effects for a band-limited Gaussian random process with applications to A/D conversion". In: *Acoustics, Speech, and Signal Processing, IEEE International Conference on ICASSP '87*. Institute of Electrical and Electronics Engineers, 1987, pp. 924–927.

[Och04] H Ochiai. "A novel trellis-shaping design with both peak and average power reduction for OFDM systems". In: *IEEE Trans. Commun.* 52.11 (2004), pp. 1916–1926.

[Och12] H Ochiai. "On instantaneous power distributions of single-carrier FDMA signals". In: *IEEE Wireless Commun. Lett.* 1.2 (Apr. 2012), pp. 73–76.

[Och13] H Ochiai. "An analysis of band-limited communication systems from amplifier efficiency and distortion perspective". In: *IEEE Trans. Commun.* 61.4 (2013), pp. 1460–1472.

[OI01] H Ochiai and H Imai. "On the distribution of the peak-to-average power ratio in OFDM signals". In: *IEEE Trans. Commun.* 49.2 (2001), pp. 282–289.

[OI02] H Ochiai and H Imai. "Performance analysis of deliberately clipped OFDM signals". In: *IEEE Trans. Commun.* 50.1 (2002), pp. 89–101.

[Olv10] Frank W J Olver. *NIST Handbook of Mathematical Functions*. Cambridge University Press, May 2010.

[Pro01] John G Proakis. *Digital Communications*. McGraw-Hill Science, Engineering & Mathematics, 2001.

[Rap91] C Rapp. "Effects of HPA-nonlinearity on a 4-DPSK/OFDM-signal for a digital sound broadcasting system". In: *Proc. of the Second European Conference on Satellite Commun., 1991. ECSC 1991*. Liege, Belgium, Oct. 1991, pp. 179–184.

[RC09] K Raghunath and A Chockalingam. "SC-FDMA versus OFDMA: sensitivity to large carrier frequency and timing offsets on the uplink". In: *GLOBECOM'09: Proceedings of the 28th IEEE conference on Global telecommunications*. IEEE Press, Nov. 2009, pp. 1–6.

[Ree62] I Reed. "On a moment theorem for complex Gaussian processes". In: *Information Theory, IRE Transactions on* 8.3 (1962), pp. 194–195.

[Row82] H E Rowe. "Memoryless nonlinearities with Gaussian inputs: Elementary results". In: *Bell System Technical Journal, The* 61.7 (1982), pp. 1519–1525.

[RQZ05] R Raich, H Qian, and G T Zhou. "Optimization of SNDR for amplitude-limited nonlinearities". In: *IEEE Trans. Commun.* 53.11 (2005), pp. 1964–1972.

[Sal81] AAM Saleh. "Frequency-independent and frequency-dependent nonlinear models of TWT amplifiers". In: *IEEE Trans. Commun.* 29.11 (1981), pp. 1715–1720.

[SC97] T M Schmidl and D C Cox. "Robust frequency and timing synchronization for OFDM". In: *IEEE Trans. Commun.* 45.12 (Dec. 1997), pp. 1613–1621.

[SSC11] Shreyas Sen, Rajarajan Senguttuvan, and Abhijit Chatterjee. "Environment-adaptive concurrent companding and bias control for efficient power-amplifier operation". In: *IEEE Trans. Circuits Syst. I, Reg. Papers* 58.3 (Mar. 2011), pp. 607–618.

[SST] M Sabbaghian, A Sulyman, and V Tarokh. "Capacity analysis for Gaussian channels with memoryless nonlinear hardware". In: *IEEE International Conference on Communications (ICC)* (), pp. 3403–3407.

[TO09a] M Tanahashi and H Ochiai. "Near constant envelope trellis shaping for PSK signaling". In: *IEEE Trans. Commun.* 57.2 (2009), pp. 450–458.

[TO09b] M Tanahashi and H Ochiai. "Trellis shaping for controlling envelope of single-carrier high-order QAM signals". In: *IEEE J. Sel. Topics Signal Process.* 3.3 (2009), pp. 430–437.

[TPZ05] S C Thompson, J G Proakis, and J R Zeidler. "The effectiveness of signal clipping for PAPR and total degradation reduction in OFDM systems". In: *Global Telecommunications Conference, 2005. GLOBECOM '05. IEEE*. IEEE, 2005, pp. 5–2811.

[Vas+05] Dimitris Vassis et al. "The IEEE 802.11g standard for high data rate WLANs". In: *IEEE Netw.* 19.3 (2005), pp. 21–26.

[VR01] JHK Vuolevi and T Rahkonen. "Measurement technique for characterizing memory effects in RF power amplifiers". In: *IEEE Trans. Microwave Theory Techn.* 49.8 (2001), pp. 1383–1389.

[Wan+14] Cheng-Xiang Wang et al. "Cellular architecture and key technologies for 5G wireless communication networks". In: *IEEE Commun. Mag.* 52.2 (2014), pp. 122–130.

[WG05] D Wulich and L Goldfeld. "Bound of the distribution of instantaneous power in single carrier modulation". In: *IEEE Trans. Wireless Commun.* 4.4 (2005), pp. 1773–1778.

[WGK10] S Wei, D Goeckel, and P A Kelly. "Convergence of the complex envelope of bandlimited OFDM signals". In: *IEEE Trans. Inform. Theory* 56.10 (2010), pp. 4893–4904.

[WN15] Rodney Waterhouse and Dalma Novack. "Realizing 5G: microwave photonics for 5G mobile wireless systems". In: *IEEE Microw. Mag.* 16.8 (2015), pp. 84–92.

[YBZ12] Z Yu, R J Baxley, and G T Zhou. "EVM and achievable data rate analysis of clipped OFDM signals in visible light communication". In: *EURASIP J. Wireless Commun. Netw.* (2012).

[YGP11] H Yoo, F Guilloud, and R Pyndiah. "Amplitude PDF analysis of OFDM signal using probabilistic PAPR reduction method". In: *EURASIP J. Wireless Commun. Netw.* 2011.1 (2011), p. 983915.

[Zho00] G T Zhou. "Analysis of spectral regrowth of weakly nonlinear power amplifiers". In: *IEEE Commun. Lett.* 4.11 (2000), pp. 357–359.

[Zor+10] Michele Zorzi et al. "From today's INTRAnet of things to a future INTERnet of things: a wireless- and mobility-related view". In: *IEEE Wireless Commun.* 17.6 (Dec. 2010), pp. 44–51.

[ZR04] G T Zhou and R Raich. "Spectral analysis of polynomial nonlinearity with applications to RF power amplifiers". In: *EURASIP J. Appl. Signal Process* 2004 (2004), pp. 1831–1840.

Publications

Journals

- Taewoo Lee and Hideki Ochiai, "A New Trellis Shaping Design for Peak Power Reduction of SC-FDMA Signals with High-Order QAM," (under review in IEEE Transactions on Vehicular Technology)
- Taewoo Lee and Hideki Ochiai, "Characterization of power spectral density for nonlinearly amplified OFDM signals based on cross-correlation coefficient" *EURASIP Journal on Wireless Communications and Networking* ,no. 1, pp. 199-213, August 2014.

International Conference Papers

- Taewoo Lee and Hideki Ochiai, "Experimental Analysis of Clipping and Filtering Effects on OFDM Systems," *IEEE International Conference on Communications 2010 (ICC 2010)*, vol., no., pp.1-5, Cape Town, South Africa, May 2010.
- Taewoo Lee and Hideki Ochiai, "On limitation of clipping and filtering in IEEE 802.11g based wireless LAN system," *IEEE 12th Annual Wireless and Microwave Technology Conference 2011 (WAMICON 2011)*, vol., no., pp.1-5, Clearwater Beach, FL, April 2011
- Taewoo Lee and Hideki Ochiai, "Peak power reduction of SC-FDMA signals based on trellis shaping," *IEEE Global Communications Conference 2012 (GLOBECOM 2012)*, vol., no., pp.3268-3273, Anaheim, CA, Dec. 2012
- Taewoo Lee and Hideki Ochiai, "A simple characterization of power spectral density for nonlinearly amplified OFDM signals," IEEE Topical Conference on Power Amplifiers for Wireless and Radio Applications 2014 (PAWR 2014), vol., no., pp.88-90, Newport Beach, CA, Jan. 2014

Domestic Conference Papers

- 李 泰雨、落合秀樹、“ 2.4Ghz 無線変調方式におけるパワーアンプの非線形歪みに関する一検討 ”、無線通信システム研究会 (RCS)、RCS2009-30、pp.17-20、名古屋大学、2009 年 6 月
- 李 泰雨, 落合秀樹,“ Clipping and Filtering を用いた OFDM システムにおけるパワーアンプの非 線形歪みの特性評価 ”, 無線通信システム研究会,RCS2009-207,pp.1-5, 九州大学, 2010 年 1 月
- 李 泰雨、落合秀樹、“ Clipping and Filtering が OFDM システムに与える影響に関する検証 ”, 電子情報通信学会 (総合大会)、東北大学、2010 年 3 月
- 李泰雨, 落合秀樹, “ IEEE 802.11g における Clipping and Filtering の適用効果に関する一検討, ”ワイドバンドシステム研究会 (WBS), WBS2010-31, pp.59-63, 2010 年 10 月
- 李泰雨, 落合秀樹, “ Cyclic Prefix を用いた SC-FDE 信号の Trellis Shaping によるピーク電力低威の一手法, ”電子情報通信学会 (総合大会)、北海道大学、2011 年 8 月
- 李泰雨, 落合秀樹, “ トレリスシェイピングを用いた SC-FDMA 信号の ピーク電力低減に関する検討, ”電子情報通信学会, vol. 112, no. 50, WBS2012-6, pp. 29-34, 2012 年 5 月
- 李泰雨, 落合秀樹, “ 非線形増幅された OFDM 信号の 電力スペクトル密度推定に関する一検討, ”電子情報通信学会 (総合大会)、新潟大学、2014 年 3 月